

NEW OBSERVATIONAL AND THEORETICAL INSIGHTS ON CASSIOPEIA A

by

Kristoffer Albert Eriksen

---

A Dissertation Submitted to the Faculty of the  
DEPARTMENT OF ASTRONOMY  
In Partial Fulfillment of the Requirements  
For the Degree of  
DOCTOR OF PHILOSOPHY  
In the Graduate College  
THE UNIVERSITY OF ARIZONA

2009

THE UNIVERSITY OF ARIZONA  
GRADUATE COLLEGE

As members of the Dissertation Committee, we certify that we have read the dissertation prepared by Kristoffer Albert Eriksen entitled *New Observational and Theoretical Insights on Cassiopeia A* and recommend that it be accepted as fulfilling the dissertation requirement for the Degree of Doctor of Philosophy.

\_\_\_\_\_ Date: 12 June 2009  
David Arnett

\_\_\_\_\_ Date: 12 June 2009  
John Biegging

\_\_\_\_\_ Date: 12 June 2009  
Philip Pinto

\_\_\_\_\_ Date: 12 June 2009  
John Raymond

\_\_\_\_\_ Date: 12 June 2009

Final approval and acceptance of this dissertation is contingent upon the candidate's submission of the final copies of the dissertation to the Graduate College.

I hereby certify that I have read this dissertation prepared under my direction and recommend that it be accepted as fulfilling the dissertation requirement.

\_\_\_\_\_ Date: 12 June 2009  
Dissertation Director: David Arnett

## STATEMENT BY AUTHOR

This dissertation has been submitted in partial fulfillment of requirements for an advanced degree at The University of Arizona and is deposited in the University Library to be made available to borrowers under rules of the Library.

Brief quotations from this dissertation are allowable without special permission, provided that accurate acknowledgment of source is made. Requests for permission for extended quotation from or reproduction of this manuscript in whole or in part may be granted by the head of the major department or the Dean of the Graduate College when in his or her judgment the proposed use of the material is in the interests of scholarship. In all other instances, however, permission must be obtained from the author.

SIGNED: Kristoffer Albert Eriksen

## ACKNOWLEDGMENTS

I must first thank my parents, for whom their childrens' educations have always been a priority. Without their sacrifices and encouragement I would not be where I am.

None of the work in this dissertation would have been possible without the tutelage, support, and inspiration of John Raymond. I also thank him for quite possibly being the only person in the world to read both my undergraduate thesis and Ph.D. dissertation.

I learned the hydrodynamics techniques used in this dissertation over parts of two summers spent at Los Alamos National Laboratory. I thank Patrick Young, Chris Fryer, Aimee Hungerford, and Frank Timmes for their hospitality and support.

Thank you to my adviser, David Arnett, for allowing me to take the highly circuitous route I took on this thesis, and for encouragement along the way.

Much credit goes to Phil Pinto and Marc Metchnik, whose advice on algorithms and techniques has been invaluable, and without whom I would not have even attempted much of what is in this document.

I thank Don McCarthy and Craig Kulesa for supporting numerous PISCES runs on the 90" and MMT, and I apologize that my weather karma was in effect for most of those nights.

Carmen Henley, Michelle Cournoyer, Catalina Diaz-Silva, and Erin Carlson have put out more administrative fires of my starting than I care to admit, and I am forever in debt to them.

Thank you to the Kickrunners.com 30s, my "imaginary" running friends, who were with me every step of my running journey the last 3 years, without which I would not have made it to the end of this dissertation.

The only person who can truly understand the plight of a graduate student is another graduate student, and I am indebted to many, many of the Steward and LPL grads past and present, with whom I have commiserated over problem sets, beers, at post-race breakfasts, and under skies both cloudy (too often) and clear (occasionally). Wilson Liu, Andy Marble, Jeremy Bailin, Jane Rigby, Andrea Leistra, Mandy Proctor, Richard Cool, Amy Stutz, Eric Nielsen, Karen Knierman, Kristian Finlator, Moire Prescott, Iva Momcheva, Casey Meakin, Patrick Young, Eric Mamajek, Kevin Flaherty, Lei Bai, Melanie Freed, Chris Groppi, Jackie Monkiewicz, Krystal Tyler, Kate Brutlag, Brandon Swift, Lei Xu, Wayne Schlingman, Wiphu Rujopakarn, and more I am sure I am have left out (I'm sorry!), thank you sincerely.

Most of all, I thank Jennifer Donley, who I think has worried more about this thesis than even I have, though she tried not to show it. You are the best, truly.

...oh, and I thank our cat Starbuck for being fuzzy, purry, and crazy.

## DEDICATION

To Jenn, love of my life, and companion for this very long journey.

And, to Susan Brennan, Iris Brough, John Fernandez, Jane Chaplin, and all the other teachers and professors who inspired me.

## TABLE OF CONTENTS

LIST OF FIGURES . . . . .	8
LIST OF TABLES . . . . .	9
ABSTRACT . . . . .	10
CHAPTER 1 INTRODUCTION . . . . .	12
1.1 An Overview of Nucleosynthesis . . . . .	13
1.2 Supernovae and Supernova Remnants . . . . .	17
1.3 Cassiopeia A . . . . .	19
1.4 This Volume . . . . .	21
CHAPTER 2 THE REDDENING TOWARD CASSIOPEIA A'S SUPERNOVA: CON- STRAINING THE $^{56}\text{Ni}$ YIELD . . . . .	24
2.1 Introduction . . . . .	24
2.2 Observations . . . . .	27
2.2.1 Near-Infrared Imaging . . . . .	27
2.2.2 Near-Infrared Spectroscopy . . . . .	30
2.2.3 <i>Spitzer</i> Mid-Infrared Imaging . . . . .	31
2.3 The Extinction Toward Cas A . . . . .	31
2.3.1 Reddening Measurements from Emission Lines . . . . .	31
2.3.2 [Fe II] Reddening Measurements . . . . .	34
2.3.3 Reddening Measurement from Infrared Synchrotron Emis- sion . . . . .	38
2.4 Discussion . . . . .	44
2.4.1 Cas A's Supernova at Maximum Light . . . . .	44
2.4.2 $^{56}\text{Ni}$ and $^{44}\text{Ti}$ . . . . .	46
2.5 Conclusion . . . . .	49
CHAPTER 3 ILLUMINATING THE COLD EJECTA IN CAS A . . . . .	51
3.1 Introduction . . . . .	51
3.2 Basic Conditions . . . . .	53
3.2.1 Spectroscopy by Eye . . . . .	53
3.2.2 Photoionization Equilibrium . . . . .	56
3.3 The Mean Density Ejecta . . . . .	59
3.3.1 One-dimensional Hydrodynamics, Radiative Transfer, and Non-equilibrium Ionization . . . . .	59
3.3.2 Fluid Evolution . . . . .	61
3.3.3 The Interior Pressure . . . . .	64
3.4 One Zone Models of the Dense Ejecta . . . . .	70
3.4.1 Model Calculations . . . . .	70

TABLE OF CONTENTS — *Continued*

3.4.2	Fluid Behavior . . . . .	73
3.5	Discussion . . . . .	74
3.5.1	The [S III] lines . . . . .	74
3.5.2	Where is the Iron? . . . . .	79
3.6	Summary . . . . .	81
CHAPTER 4	MULTI-DIMENSIONAL HYDRODYNAMICS AND NON-EQUILIBRIUM IONIZATION IN METAL-RICH PLASMA . . . . .	83
4.1	The Physics of Supernova Remnant Shocks . . . . .	83
4.1.1	Hydrodynamics . . . . .	85
4.1.2	Non-equilibrium Ionization . . . . .	87
4.1.3	Cooling and Heating . . . . .	91
4.1.4	Photoionization and Radiative Transfer . . . . .	91
4.2	Algorithms . . . . .	92
4.2.1	Hydrodynamics . . . . .	92
4.2.2	Time-Dependent Ionization and Cooling . . . . .	100
4.2.3	Timestep Control . . . . .	101
4.2.4	OpenMP Parallelization . . . . .	102
4.3	Test Problems . . . . .	108
4.3.1	Collisional Ionization Equilibrium . . . . .	109
4.3.2	One Dimensional Shocks . . . . .	109
4.4	Two Dimensional Simulation of a Shock-Cloud Interaction . . . . .	120
4.4.1	Justification for Two Dimensions . . . . .	120
4.4.2	Cloud-shock Simulation . . . . .	125
4.4.3	The Effects of Resolution . . . . .	126
4.5	Where to Go . . . . .	129
CHAPTER 5	CONCLUSION . . . . .	134
5.1	Results . . . . .	134
5.2	Future Work . . . . .	136
Appendix A	A One Dimensional Hydrodynamics, Radiative Transfer, and Non-equilibrium Ionization Code . . . . .	139
A.1	Hydrodynamics . . . . .	139
A.2	Time-Dependent Ionization . . . . .	139
A.3	Radiative Transfer . . . . .	141
A.4	Line Cooling, PI Heating, and Coulomb Equilibrium . . . . .	145
A.5	Initial Conditions . . . . .	148
A.6	Subsequent Execution . . . . .	150
REFERENCES	. . . . .	152

## LIST OF FIGURES

2.1	PISCES $JHK_s$ Color Image of Cas A . . . . .	29
2.2	The locations of knots with measured [Fe II] ratios . . . . .	35
2.3	Measured [Fe II] ratios . . . . .	36
2.4	Measured infrared flux densities for synchrotron knot N . . . . .	39
2.5	Likelihood contours for knot N fit parameters . . . . .	43
2.6	$^{56}\text{Ni}$ mass . . . . .	47
3.1	Heating and line cooling rates for the 1D simulation . . . . .	60
3.2	Ejecta pressure and temperature evolution for the 1D simulation . . . . .	62
3.3	Sample one zone spectra . . . . .	66
3.4	S50 cooling function . . . . .	67
3.5	$F(18\mu\text{m})/F(33\mu\text{m})$ sensitivity to $T_e$ and $n_e$ . . . . .	75
3.6	Calculated Fe line emissivities for the solar abundance gas. . . . .	79
4.1	Collisional ionization equilibrium for oxygen . . . . .	110
4.2	Collisional ionization equilibrium for iron . . . . .	111
4.3	Ion fraction vs. ionization age ( $n_e t$ ) for oxygen . . . . .	112
4.4	Ion fraction vs. ionization age ( $n_e t$ ) for iron . . . . .	113
4.5	2500 km/s oxygen shock, no cooling . . . . .	116
4.6	2500 km/s oxygen shock, He-like preionization . . . . .	117
4.7	2500 km/s oxygen shock, C-like preionization . . . . .	118
4.8	Pressure and velocity for a radiative shock . . . . .	121
4.9	Temperature and density for a radiative shock . . . . .	122
4.10	Pressure, velocity, and ionization state for a radiative shock . . . . .	123
4.11	Two-dimensional cloud shock, electron density and temperature . . . . .	127
4.12	Two-dimensional cloud shock, electron density and temperature, cont'd . . . . .	128
4.13	Resolving the leeward radiative shock . . . . .	130
A.1	Radiative transfer geometry . . . . .	143

## LIST OF TABLES

3.1	Model Abundances . . . . .	55
3.2	One Zone Model Line Fluxes, Depleted Solar Abundances <sup>a</sup> . . . . .	65
3.2	One Zone Model Line Fluxes, Depleted Solar Abundances <sup>a</sup> . . . . .	68
3.3	One Zone Model Line Fluxes, Incomplete Oxygen Burning <sup>a</sup> . . . . .	69
3.3	One Zone Model Line Fluxes, Incomplete Oxygen Burning <sup>a</sup> . . . . .	70
4.1	Dielectronic Recombination Coefficient References . . . . .	90

## ABSTRACT

Using two techniques not previously applied to Cassiopeia A (Cas A), we measure the reddening toward its expansion center. An estimate of  $A_V$  from the near-IR [Fe II] lines is hampered by uncertain atomic data, though the spatial variation in their flux ratio allows relative measurement of the extinction in regions without previous optical estimates. We use a second technique based on the broad-band IR shape of the synchrotron emission, and find  $A_V = 6.2 \pm 0.6$  for a knot  $13''$  from the expansion center. Assuming a plausible lower limit on the apparent magnitude of the SN in outburst, the  $^{56}\text{Ni}$  yield was  $0.058 < M_{\text{Ni}} < 0.16 M_{\odot}$ . With the  $^{44}\text{Ti}$  mass from published gamma-ray observations, this implies a  $^{44}\text{Ca}/^{56}\text{Fe}$  ratio consistent with the solar abundance.

Recently published *Spitzer Space Telescope* IRS observations detect dust and line emission from cold gas interior to Cas A's reverse shock. Using simple physical arguments and new hydrodynamic, non-equilibrium photoionization calculations, we infer the physical conditions in this material. We find that the mid-IR bright clumps are photoionized by the SNR shocks, over-dense relative to the expected average in the interior of the remnant, and have abundances consistent with incomplete oxygen burning. The lack of detectable iron lines indicates that any Si-burning material still interior to the reverse shock must be far more tenuous than the clumps of O-burning ashes.

Finally, we present calculations from a new multi-dimensional hydrodynamics and non-equilibrium ionization and cooling code designed to model the emission from SNR shocks. Two-dimensional simulations of a shock-cloud interaction in a pure-oxygen plasma, with flow parameters relevant to Cas A, show a wider range of temperatures and ionization states than is typical in single-zone or 1D

calculations, indicating that fluid and cooling instabilities play a role in producing the observed spectra of radiative shocks in metal-rich gas.

## CHAPTER 1

## INTRODUCTION

The theory of nucleosynthesis is a fundamental pillar upon which the rest of astrophysics is built. Much of our understanding of the Universe flows from the basic premise that the primordial hadronic gas consisted nearly entirely of hydrogen and helium, and has been slowly polluted with the nuclear burning products of successive generations of stars. This central tenet is implicit in such diverse fields of astronomy as galaxy structure and evolution, star and planet formation, and the physics of the interstellar and intergalactic media, where the estimates of the metallicity are often proxies for age, mixing, star formation history, and a host of other astrophysically interesting but difficult to measure properties.

The basic nuclear, stellar, and cosmological physics that comprise the theory of nucleosynthesis are well established. Hydrogen, deuterium, and helium were created in the first minutes after the Big Bang, while the vast majority of heavier elements were cooked in stellar interiors and returned to interstellar space in supernovae (SNe) for incorporation into new stars. However, there is still much we do not know about the details of this process. By mass, most nuclear burning in the present-day Universe occurs in the cores of low-mass stars, whose ashes will forever be locked in passively cooling white dwarfs — an evolutionary dead end. Instead, it is the small minority of stars that die as supernovae that chemically enrich their environs, and it is therefore these stars and their supernovae we must understand. Unfortunately, the cores of massive stars (particularly during the advanced burning stages) are vigorously convective — a process that manifestly couples 3D hydrodynamics and nuclear reactions — and their envelopes are dramatically modified by stellar winds or binary interactions, drastically com-

plicating the modeling of stellar structure and evolution. Supernovae themselves feature much of the complex physics of massive stars, plus neutrino transport and a nuclear density equation of state. While progress toward understanding SNe is constantly being made with newer and better numerical simulations, the general problem of supernova explosions is far from solved. Observationally, the situation is similarly difficult. Supernovae occur at a rate of approximately 1 per century in star-forming  $L^*$  galaxies, and the bulk of the important physics in these rare events is hidden from view. Fortunately, the enormous kinetic energy released in a SN leaves an imprint on the surrounding medium that may be detectable for tens of millennia: a supernova remnant (SNR). During the first thousand years or so, when an SNR is “young,” the nucleosynthetic signature of its nascent SN and progenitor star is still visible. Only a handful of such young remnants are known; this dissertation focuses on one, Cassiopeia A.

## 1.1 An Overview of Nucleosynthesis

The application to astrophysics in the 1920s of the new quantum theory inspired great advances in our understanding of the physical processes active in stars. A number of works, most famously Cecilia Payne-Gaposchkin’s pioneering Ph.D. dissertation (Payne 1925) in which she applied Saha’s theory of thermal ionization to stellar atmospheres, established that hydrogen and helium are the dominant constituents of the Sun. Given this composition and the calculated conditions in the solar core, it was logical to conclude that the fusion of hydrogen must be the primary source of energy in normal stars. Early hypotheses focused on electromagnetic interactions with other light nuclei (e.g.  $p + {}^6\text{Li} \rightarrow {}^7\text{Be}$ ), though the low abundance of trace light nuclei such as  ${}^6\text{Li}$  and the rapid rate of these reactions exhaust the fuel on timescales much shorter than the main a stellar life-

time. Hans Bethe (1939) was the first to realize the role of the weak interaction, which enables transmutation a proton into a neutron (e.g.  $p+p \rightarrow D+\beta^++\nu_e$ ), and correctly identify the PP chain and CNO cycle as the sources of energy in main sequence stars. He also recognized that the lack of stable isotopes with atomic mass 5 or 8 prevented the creation of nuclei heavier than helium with simple hydrogen burning.

That the two next most cosmically abundant nuclei after  $^1\text{H}$  and  $^4\text{He}$  ( $^{12}\text{C}$  and  $^{16}\text{O}$ ) consist of three and four  $\alpha$ -particles was a strong indication that many-body reactions involving  $^4\text{He}$  were necessary to hurdle the  $A = 5, 8$  gap. Through theoretical and laboratory work of Salpeter, Hoyle, Cook, and others (see Clayton 1983 for a full discussion), it became clear that the dominant He-burning mechanism was a two-step process. Despite its extremely short lifetime ( $\sim 10^{-16}$  s), a small equilibrium abundance of  $^8\text{Be}$  forms at high enough temperature and density ( $Y(^8\text{Be})/Y(^4\text{He}) \sim 10^{-9}$  in a helium gas with  $T = 1 \times 10^8$  K and  $\rho = 10^5 \text{ g cm}^{-3}$ ), which can resonantly capture a third  $^4\text{He}$  nucleus, completing the triple- $\alpha$  process:  $3 ^4\text{He} \rightarrow ^{12}\text{C}$ . Captures of additional  $\alpha$ 's form  $^{16}\text{O}$  and  $^{20}\text{Ne}$ .

Hoyle (1946), building on previous work by Chandrasekhar, noted that the observed abundances of nuclei from  $^{12}\text{C}$  through the iron-peak are consistent with the nuclear statistical equilibrium populations for  $T \sim 10^9$  K in electron-degenerate gas. We now know this idea to be essentially correct – stars beyond an initial main sequence mass of about  $8M_\odot$  are, following He-depletion, able to ignite their carbon, and undergo successive stages of C, Ne, O, and Si-burning, eventually producing an  $^{56}\text{Fe}$  core. Since fusion beyond  $Z = 26$  is endothermic, the star no longer has an energy source, initiating the complex physical processes that leads to a core-collapse supernova.

This of course leaves nuclei heavier than iron, which are not produced by

the processes described above. One important clue as to the physics at work is the presence of technetium, which has no stable isotopes, in the spectra of the chemically anomalous S-type giants (Merrill 1952), indicating nuclear processing on a timescale of order  $\sim 10^5$  yr (the lifetime of Tc's most stable nucleus). Cameron (1955) showed that the  $^{13}\text{C}(\alpha,n)^{16}\text{O}$  reaction, active as a minor branch during CNO cycling, produces significant free neutrons, which are captured onto successively heavier nuclei, creating elements up through lead. These products, including a detectable fraction of  $^{99}\text{Tc}$ , are brought up to the stellar photosphere through convection. This slow neutron capture (the s-process) proceeds up the valley of  $\beta$ -stability, and produces sharp abundance peaks at the neutron magic numbers (where the absorption cross section is small). The s-process matches some, but not all of the observed abundance pattern beyond Zn, indicating the existence of another mechanism: rapid neutron capture. The r-process is active for extremely high neutron flux, when the capture timescale is much less than the  $\beta$ -decay time, so the produced isotopes can be far from  $\beta$ -stable. These conditions are generally thought to exist during core-collapse, and perhaps nowhere else in the Universe.

It bears mention that before stellar- and supernova-based nucleosynthesis became widely accepted, a competing theory was proposed. Hubble's discovery of cosmological expansion led to the obvious hypothesis that the Universe was once very small, hot, and dense. (Fred Hoyle, a proponent of the competing and incorrect Steady State cosmology called this the Big Bang scenario, a name which has obviously stuck.) Alpher, Bethe & Gamow (1948, the so-called  $\alpha\beta\gamma$  paper) proposed that the cosmic abundance was established by neutron-capture processes during a phase of the early Universe when protons and neutrons were in approximate thermal equilibrium. While the discovery of the Cosmic Microwave

Background confirmed the Big Bang, it also definitively showed that while cosmological nucleosynthesis did occur in the first 15 minutes, the Universe was far too tenuous for the  $3\alpha$  reaction to bridge the  $A = 5, 8$  gap, and the free thermal neutrons were either incorporated into light nuclei (primarily  ${}^4\text{He}$ ), or decayed.

While the improvement of computing power and nuclear reaction rates and the refinement of theory have shaped our understanding of the nucleosynthetic processes outlined above, the basic picture remains the same. In the first minutes after the Big Bang, thermal protons and neutrons constituted the sum of hadronic matter in the Universe. As the cosmos cooled, fusion reactions consumed approximately 25% of the protons (i.e.  ${}^1\text{H}$ ) and created D,  ${}^3\text{He}$ ,  ${}^4\text{He}$ ,  ${}^7\text{Li}$ , and little else. Starting some hundreds of millions years later, and continuing for the next 13 billion years to the present day, successive generations of stars have processed a fraction of these light elements to heavier nuclei. The problem is solved.

Well, no. In reality, while all stars burn hydrogen on the main sequence, and most will burn helium on the horizontal branch or the red clump, the vast majority of stars lack the mass to ignite carbon burning and eventually produce a supernova. After they exhaust their available fuel, their carbon and oxygen-rich cores are forever locked in passively cooling white dwarfs. While the envelopes of the low-mass stars are ejected in planetary nebula which may be enriched in elements such as nitrogen and the s-process nuclei, most nucleosynthesis is both hidden from our view and its products unavailable to be incorporated into future generations of stars, planets, and astronomers. Instead, the vast majority of the chemically enriched material in the Universe was returned to the interstellar medium in supernova explosions. Thus, to truly understand nucleosynthesis, we must truly understand supernovae.

## 1.2 Supernovae and Supernova Remnants

The historical record of “guest stars” extend backs for nearly 2000 years, though the application of the telescope to astronomy greatly extended the grasp of astronomers, and led to the discovery of many transiently bright objects. Of particular note was the discovery in 1885 of a “new star” (S Andromeda, which eventually peaked near 6 mag) in M31 that was visible in the telescopes of the day for nearly 5 months. This object re-ignited the debate about the nature of the “spiral nebulae,” and, ironically, was apparently used to bolster the argument against the “island universe” hypothesis, due to the excessively large luminosity for S And that would imply (de Vaucouleurs & Corwin 1985). However, Hubble’s definitive measurement of the distance to M31 firmly established the existence of a separate class of object far more luminous than the common nova.

Walter Baade and Fritz Zwicky were likely the first to coin the term supernova (Osterbrock 2001) and speculate that the enormous SN luminosity derived from the gravitational collapse of a massive star to a neutron star (Baade & Zwicky 1934). We now know this physical scenario to be essentially correct for core-collapse supernovae, which account for approximately half those observed. (SN type Ia’s, constituting the other half, arise from the deflagration-detonation of an accreting white dwarf.) Beyond this basic premise, stellar structure calculations show that by the time massive stars develop an iron core, their structure consists of successive shells of nuclear ashes, from Si-burning products near the core, to an outer envelope which may be heavily modified by a stellar wind or binary interaction. Once pressure support is lost, the core contracts on approximately a free-fall timescale, until electron captures in the densest material at the center produce a proto-neutron star. At this point, neutron degeneracy pressure abruptly halts further core contraction, and still in-falling material “bounces,” and sends a

strong shock outward through the star. The details of this explosion mechanism are still not understood, and since it occurs deep in the star, direct observation may only be made with neutrinos, which require a sensitive neutrino telescope and a very nearby supernova. (Indeed, neutrinos have been detected from exactly one event, SN 1987A; Hirata et al. 1987; Bionta et al. 1987) Alternatively, the abundance yield of a particular supernova, though less direct, provides a more accessible diagnostic of the details of the explosion, and the composition and structure of the progenitor star. In particular, the presence or absence of the more advanced burning products help constrain how much mass was incorporated into the compact remnant (either a neutron star or a black hole), while the ratio of C-burning to He-burning or CNO ashes may provide information on the mass and evolutionary history of the progenitor.

Once the shock breaks out of the stellar envelope, the supernova's luminosity, which may out-shine its host galaxy for weeks, is powered primarily by the radioactive decay of  $^{56}\text{Ni}$  produced in the explosion, and later by  $^{56}\text{Co}$ , its daughter product. While bright and easy to observe, the supernova is optically thick for months, so only the photosphere is visible, and the extreme flow velocities (perhaps greater than 10,000 km/s) broaden its spectral features dramatically, limiting detailed abundance analysis. However, given the exceedingly large kinetic energy released in the explosion (of order  $10^{51}$  ergs), the effect of the supernova on its surrounding medium is visible for millennia. This nebular ghost is called a supernova remnant (SNR).

Canonical SNR evolution consists of three stages: free-expansion (when the supernova ejecta are essentially undecelerated), the Sedov phase (starting when the mass of entrained interstellar material is approximately equal to the ejecta mass and the expansion is well-described by the Sedov-Taylor similarity solu-

tion), and the snow plow phase (when a dense shell forms behind the radiative blast wave, and the remnant expands due to its momentum). (Given Cas A's relative youth, this dissertation is mostly concerned with the last free-expansion and early-ST stages.) In the first phase of evolution, the outward-traveling blast wave begins to decelerate as it sweeps up circumstellar gas, and freely-expanding SN material piles up behind the blast, driving a reverse shock into the ejecta. The emission from these two shocks give young SNRs their characteristic double-ringed morphology in X-rays. In addition, if the ejecta is clumped, the reverse shock drives slower secondary shocks into the denser clouds, which are often slow enough to produce optical emission in their cooling regions. It is the combination of these X-ray and optically emitting structures in the reverse-shocked material that provide our best look at the supernova's nucleosynthetic ashes.

### 1.3 Cassiopeia A

Cassiopeia A (Cas A, so-named because it was originally discovered as the brightest radio source in the constellation Cassiopeia, it is also known as G111.7-2.1, its Galactic coordinates) is the remnant of one of the most recent known supernova in the Galaxy. The first photographic images and spectra of the nebulosity associated with the radio source (Baade & Minkowski 1954) showed high-velocity emission lines of oxygen, while subsequent observations (van den Bergh 1971) established the existence of two types of optical knots in Cas A: the "fast-moving knots" (FMKs) characterized by a pure line spectrum of metals devoid of hydrogen and helium with Doppler shifts of up to at least 6000 km/s, and the "quasi-stationary flocculi" (QSFs) of slower-moving material with hydrogen and helium, possibly enhanced in nitrogen. Arnett (1975) established that the likely abundances of the FMKs are consistent with the advanced burning products of

a massive star. Kirshner & Chevalier (1977) showed that oxygen was by far the most abundant element in the FMK's and that the QSFs consist of envelope material, presumably lost in a pre-supernova wind. Cas A thus became the prototype of the "oxygen-rich" class of SNRs, young remnants of core-collapse supernovae that still exhibit the abundance pattern of their progenitor star and SN, before the ashes are mixed into the interstellar medium. There are only six other such SNRs known — two in the Galaxy (Puppis A & G292.0+1.8), two others in the LMC (N132D & 0540-69.3), one in the SMC (E0102), and an unresolved object in the more distant dwarf irregular galaxy NGC 4449.

Cas A lies nearly in the galactic plane at a distance of  $3.4_{-0.1}^{+0.3}$  kpc (Reed et al. 1995). Surprisingly, unlike the historical supernovae in 1006, 1054, 1572, and 1604 with known remnants, there were no confirmed sightings of Cas A's SN. There is some debate that Flamsteed may have seen the supernova in decline in 1680, a date nearly consistent with age estimates from the proper motion of the FMKs (Thorstensen et al. 2001). The lack of contemporary reports suggest either a subluminal SN or that the extinction to the explosion is higher than the most quoted values ( $A_V \sim 5$ , Hurford & Fesen 1996). Recent detection of a light echo from the supernova (Krause et al. 2008) definitively determined it to be have been a rare type IIb analogous to SN 1993J, which lends some credence to the subluminal argument, though the  $A_V$  across the remnant is known to be spatially variable (e.g. Troland et al. 1985).

The official "first light" observations from the *Chandra X-ray Observatory* (Tananbaum et al. 1999) revealed for the first time an X-ray point source within  $5''$  of the expansion center, presumed to be the neutron star compact remnant of Cas A's supernova. A separate analysis of the extended SNR emission from the same observation (Hughes et al. 2000) showed a wide diversity in the X-ray

spectra across the remnant, including the surprising discovery that the Fe-rich X-ray emitting ejecta lie outside the lighter ashes. Numerous *HST* campaigns (e.g. Morse et al. 2004; Hammell & Fesen 2008) and mid-IR spectral mapping observations with *Spitzer* (Smith et al. 2009) have expanded tremendously the library of exquisite observations now available for Cas A. It is time to utilize fully these data to gain a greater understanding of the processes at work in its supernova and progenitor.

That so much time on astronomy's flagship telescopes has been devoted to Cas A speaks to the enormous promise this object has in furthering our knowledge into the workings of massive stars and their nucleosynthetic yields. Yet, this potential is still largely unfulfilled, in part because the theoretical tools with which we interpret observations and gain insight to the physics at work have lagged behind the data. This situation is changing. A large collaboration, led by Chris Fryer at LANL, is attempting to model self-consistently, with the best available stellar evolution and supernova numerical tools, a massive star from the pre-main sequence through core-collapse and the supernova remnant phase. In order to inform their simulations, it is time to constrain better the observational properties of Cas A's supernova, and update the tools with which we model its various types of emission. The work in this dissertation is a start on this process.

#### 1.4 This Volume

The focus of Chapter 2 in this dissertation is new near-infrared imaging and spectroscopy of Cas A which provide the best estimates to date of the reddening toward its nascent supernova. This has implications for the observability of the putative SN 1680, and the total ejected mass of  $^{56}\text{Ni}$ , which, when taken in consideration with the  $^{44}\text{Ti}$  yield measured from gamma-ray observations, has con-

sequences for physical models of mixing and nucleosynthesis in the explosion.

In Chapter 3, we present a theoretical framework with which to interpret the recent detection with the *Spitzer Space Telescope* of ejecta interior to the reverse shock in Cas A (Smith et al. 2009). Through simple physical arguments we show the mid-IR-bright material to be cold, over-dense material. More detailed hydrodynamic, non-equilibrium photoionization simulations illuminate the physical conditions in the SNR interior. (The details of this new code are discussed at length in the Appendix.) Finally, we present model mid-IR spectra for two sets of abundances, which will provide a starting-point for modeling this previously unseen phase of supernova ejecta, once details of the observations are published. Chapter 3 as included here is a manuscript ready for submission to ApJ.

The final science chapter (Chapter 4) details the progress made toward the development of a multidimensional hydrodynamics and NEI tool to simulate supernova remnant shocks and their accompanying emission. The eventual goal is to harness the computational power of modern multi-core workstations and provide a shared-memory parallel, desktop tool analogous to the single zone codes (e.g. Itoh 1981; Cox & Raymond 1985) currently used to model the spectra of radiative shock waves, free of many of the simplifying spatial assumptions inherent in a single zone or one-dimensional approach. The current code includes a multi-dimensional, multi-species hydrodynamics package based heavily on the ZEUS-2D code (Stone & Norman 1992), coupled with a non-equilibrium ionization and cooling module, and the atomic physics database necessary for these calculations. The code is parallelized with OpenMP directives. Two dimensional simulations run routinely and efficiently on typical Macintosh or Linux machines. A radiative transfer module is still required to model properly the photoionization-recombination region downstream in radiative shock waves. We

conclude the Chapter with a discussion of the prospects for including this necessary piece of physics into future versions of the code, as well as the limitations inherent in a 2D treatment of the hydro, and the possibility of extending to three dimensions.

Chapter 5 is a short summary, and includes musings on potential future work.

## CHAPTER 2

THE REDDENING TOWARD CASSIOPEIA A'S SUPERNOVA: CONSTRAINING THE  
 $^{56}\text{Ni}$  YIELD

We present new reddening measurements toward Cassiopeia A, using two techniques not previously applied to this object. Our observations of the near-infrared [Fe II]  $1.257\mu\text{m}$  and  $1.644\mu\text{m}$  lines show the extinction to be highly variable across the remnant, increasing toward the west and the south, consistent with previous radio and X-ray observations. While the absolute value of  $A_V$  as determined by the [Fe II] lines is uncertain due to conflicting calculations and observations of their intrinsic flux ratio, parts of the remnant without previous optical measurements show comparatively higher reddening. We find  $A_V = 6.2 \pm 0.6$  from the broadband shape of the infrared synchrotron emission of a knot within  $13''$  of the expansion center. Given this reddening, the apparent faintness of the nascent supernova, and iron mass constraints from X-ray observations, we estimate an ejected mass of  $^{56}\text{Ni}$  of  $0.058 - 0.16M_{\odot}$ . Taken with  $\gamma$ -ray observations of the  $^{44}\text{Ti}$  decay chain, this nickel mass is broadly consistent with the solar  $^{44}\text{Ca}/^{56}\text{Fe}$  ratio.

## 2.1 Introduction

Given its distance ( $3.4_{-0.1}^{+0.3}$  kpc; Reed et al. 1995), circumpolar location in the northern sky, and the most quoted reddening toward Cassiopeia A ( $A_V \sim 5$ , Hurford & Fesen 1996, hereafter HF96), it is surprising that its nascent supernova was largely unreported. SN1604 (Kepler's SN), SN1572 (Tycho's SN), SN1054 (the Crab Nebula) and SN1006 were all widely observed and recorded by contemporary astronomers in Europe, the Far East, or both. Cas A was not. While Flamsteed may have seen the event as a sixth magnitude optical transient in 1680

(Ashworth 1980, though Kamper 1980 provides a dissenting opinion), it was certainly less remarkable than other historical Galactic supernovae. Why? Was the Cas A supernova an unusual, underluminous event? Were contemporary observers unlucky, and the supernova at peak brightness was highest in the northern sky during daylight? Is the extinction toward Cas A greater than previously assumed?

Aside from this historical oddity, the apparent faintness of Cas A's outburst presents an astrophysical conundrum. The peak luminosity and characteristic light curve of supernovae are driven by energy injected into the expanding stellar debris by the radioactive decay of  $^{56}\text{Ni}$  and its daughter nucleus  $^{56}\text{Co}$ . Thus, the peak brightness is proportional to the ejected mass of  $^{56}\text{Ni}$ . Since the complete explosive silicon burning that produces radioactive nickel takes place in the deepest layers of the supernova, the nickel yield is intimately linked with the explosion mechanism, energy, mass cut, and fall-back fraction. Its diagnostic power is further enhanced when compared to a supernova's  $^{44}\text{Ti}$  yield. This trace isotope is produced by " $\alpha$ -rich freeze-out," a process of incomplete silicon burning that dominates in regions of higher entropy (i.e. lower density). The high  $^{44}\text{Ti}$  abundance, as determined by  $\gamma$ -radiation observations of its decay chain (Iyudin et al. 1994, Vink et al. 2001) relative to the implied  $^{56}\text{Ni}$  mass inferred from Cas A's apparently faint outburst, are inconsistent with yields expected from symmetric explosion calculations (Timmes et al. 1996). This is generally assumed to be evidence for asymmetry in the supernova (e.g., Nagataki et al. 1998). Therefore, tighter measurements of  $^{44}\text{Ti}/^{56}\text{Ni}$  should provide helpful constraints on advanced supernova explosion calculations. Furthermore,  $^{44}\text{Ti}$  appears to be produced exclusively in core collapse and sub-Chandrasekhar mass SN Ia (Timmes et al. 1996). A measurement of radioactive titanium and nickel in Cas A may

inform Galactic chemical evolution and stellar population synthesis models in determining the relative importance of these two types of supernovae in producing the observed solar abundance ratio of  $^{44}\text{Ca}/^{56}\text{Fe}$ , the two stable daughter products of these nuclei.

Thus a proper inventory of  $^{56}\text{Ni}$  or, equivalently,  $^{56}\text{Fe}$ , in Cas A is desirable. Willingale et al. (2003), using *XMM-Newton* X-ray observations, find an X-ray emitting iron mass (presumably dominated by  $^{56}\text{Fe}$ ) of  $0.058M_{\odot}$ . Because the cooling time of the X-ray emitting plasma is generally longer than the age of the supernova remnant, this is, to a good approximation, the sum total of iron that has been heated to X-ray emitting temperatures upon passage through the reverse shock. However, it does not include denser material that retained enough electrons to cool efficiently through EUV, optical, and infrared emission. The cooling times for these plasmas can be weeks or months, making a full inventory of gas of these densities at reverse shock passage difficult. Similarly, material that has not yet encountered the reverse shock is nearly invisible.

Here we take a different approach and attempt to bound the allowed total mass of ejected  $^{56}\text{Ni}$ . Given that Cas A's SN was apparently unremarkable at Earth, knowledge of the extinction toward the supernova, a distance measurement, and a limit on the apparent magnitude place constraints on the intrinsic peak luminosity of the event. Previous optical measurements of the reddening suffer from a selection effect, in that the most common method for estimating  $A_V$  is infeasible in regions of higher extinction. Existing CO (Troland et al. 1985) and X-ray (e.g., Keohane et al. 1996) observations show the absorption to Cas A to be spatially variable, with a general trend of increasing extinction from east to west, though poor spatial resolution washes out structure on scales smaller than the beam and will underestimate  $A_V$  if the absorbers are clumped. Indeed, VLA

observations of H<sub>2</sub>CO absorption toward Cas A (Reynoso & Goss 2002) show considerable spatial structure. Moreover, radio and X-ray measurements of the absorbing column require an assumed gas-to-dust ratio to convert to optical extinction. As such, existing estimates of the reddening span several magnitudes, most commonly  $A_V \sim 4 - 8$  (Fesen et al. 2006 assume  $A_V = 6 - 8$  toward the compact remnant). These uncertainties have limited the accuracy of previous attempts (e.g., Troland et al. 1985) to use the peak brightness to constrain the properties of the supernova. Here we present significantly improved measurements of  $A_V$  using [Fe II] infrared emission lines and a new technique based on measurement of the infrared spectral index of the synchrotron emission of Cas A.

The remainder of the chapter is organized as follows. In Section 2.2 we detail the new near-infrared images and spectroscopy and the archival mid-infrared imaging we use for our measurements. In Section 2.3 we address the challenges of measuring the extinction toward Cas A with emission lines, estimate  $A_V$  from our [Fe II] observations, and describe and present results from our measurement of the infrared synchrotron emission. In Section 2.4, we bound the ejected nickel mass and discuss its implications. Section 2.5 is a summary of our results.

## 2.2 Observations

### 2.2.1 Near-Infrared Imaging

We imaged Cas A with the PISCES (McCarthy et al. 2001) near-infrared camera attached to the Steward Observatory 2.3 m Bok telescope, over two different runs in summer 2002 and 2003. The 8'.5 circular field of view and 0".5 pixels at the Bok  $f/9$  focus allowed us to image the entire remnant in a single pointing while adequately sampling typical Kitt Peak seeing, which ranged from 0".8 – 1".5. All observations were made with broadband filters from the 2MASS system.

In July 2002, we used a  $3 \times 3$  dither pattern, with 60 s individual exposures in  $J$ , and 30 s exposures in  $H$ . The total exposure times were 54 minutes in  $J$  and 40 minutes in  $H$ . In July 2003, we used a similar strategy, observing Cas A in  $J$  (45 s individual, 45 minute total exposure),  $H$  (12 s individual, 35 minutes total exposure) and  $K_s$  (10s individual, 56 minutes total exposure).

Standard image processing, including dark subtraction, flat-fielding, distortion correction, and image stacking, was accomplished with the IRAF<sup>1</sup> package. For the 2002 run, flat-field frames were constructed from median-filtered off-source dithers interspersed with on-source pointings. In 2003, no off-source pointings were taken, and flats were made from source frames. This resulted in a poor quality flat-field, and an underestimation of the flux in low-surface brightness, high-coverage features like the diffuse synchrotron emission observed in all bands. As such, the 2003  $J$  and  $H$  images were not used for flux measurements, though they were used to estimate a correction factor for the 2003  $K_s$  data. Magnitude calibration was achieved by comparison with 2MASS (Skrutskie et al. 2006) stars in the observed field.

We present in Figure 2.1 a color  $JHK_s$  image of Cas A from our PISCES data. The clumpy shocked material has strong lines in the  $J$  and  $H$  bands and appears blue-green, while the  $K_s$  image is dominated by smoother synchrotron continuum. While this nonthermal emission is detected in all bands, it is strongest at longer wavelengths, and displays red.

---

<sup>1</sup>IRAF is distributed by the National Optical Astronomy Observatory, which is operated by the Association of Universities for Research in Astronomy (AURA) under cooperative agreement with the National Science Foundation.

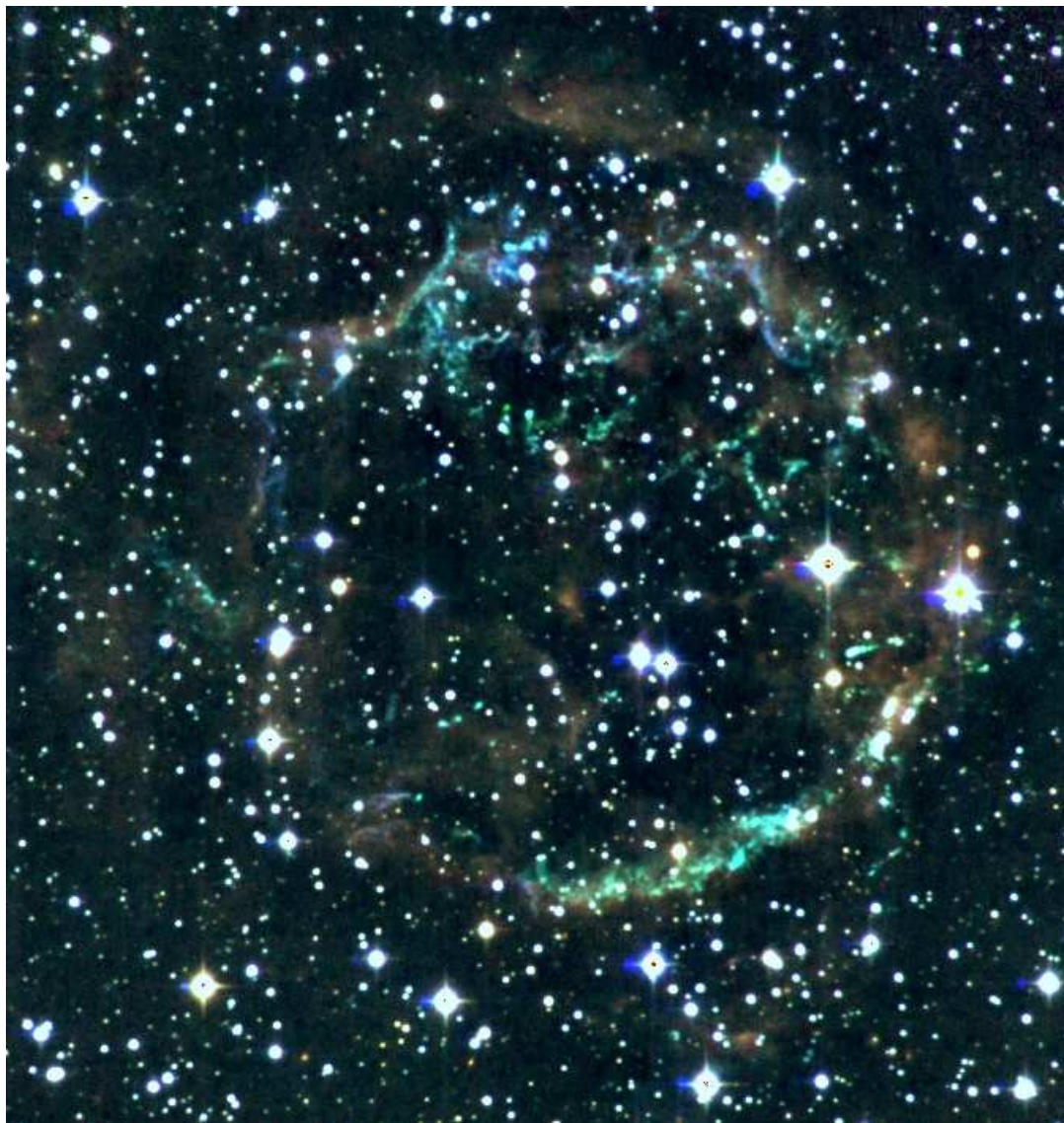


Figure 2.1 Our color  $JHK_s$  (red, green, blue) PISCES image of Cassiopeia A. The clumpy blue/green features are line emission from shock heated ejecta and circumstellar material, while the smoother red features are synchrotron emission. Synchrotron “Knot N” from Wright et al. (1999) is clearly visible as a diffuse red feature near the center of the remnant.

### 2.2.2 Near-Infrared Spectroscopy

Using our *J*-band image to target knots of interest, we observed four slit positions on 2004 September 26-27 with the FLAMINGOS<sup>2</sup> multiobject spectrograph on the KPNO 4 m telescope. The JH grism and 6 pixel wide long-slit provided simultaneous wavelength coverage from approximately 0.95-1.8 $\mu$ m across a 10'  $\times$  1.9" slit on the sky, and delivered approximately 25Å resolution across the J and H bands. The emission knots in Cas A are densely packed on the sky, so it was impossible to use the standard 10" nod along the slit for sky subtraction. Since the FLAMINGOS slit is approximately twice as long as the diameter of Cas A's bright ring, we placed all the supernova remnant line emission at one end of the slit, and used a 5' nod. While this large throw cost extra overhead (including reacquisition of a guide star at each nod), it ensured knots of interest would not overlap between nods. Utilizing an "AABB" pattern, each individual exposure was 300 s, for a total A+B on-source exposure time of 4800-6600 s.

Standard near-infrared spectroscopic reductions (dark subtraction, flat-fielding, sky subtraction, distortion correction) were accomplished with a combination of IRAF and custom Perl Data Language<sup>3</sup> (Glazebrook & Economou 1997) scripts. For the J band, we set the wavelength calibration with HeNeAr lamps. H band wavelength calibration was made against the night sky lines, using VLT/NIRMOS OH line list and sky spectrum convolved to our resolution (Rousselot et al. 2000). The instrumental throughput and telluric transmission was measured with observations of the nearby G2V star HD212809, divided by the synthetic solar spectrum included with the spectral synthesis code SPEC-

---

<sup>2</sup>FLAMINGOS was designed and constructed by the IR instrumentation group (PI: R. Elston) at the University of Florida, Department of Astronomy, with support from NSF grant AST97-31180 and Kitt Peak National Observatory

<sup>3</sup>The Perl Data Language (PDL) has been developed by K. Glazebrook, J. Brinchmann, J. Cerney, C. DeForest, D. Hunt, T. Jenness, T. Luka, R. Schwebel, and C. Soeller and can be obtained from <http://pdl.perl.org>

TRUM v2.73 (Gray & Corbally 1994). Small corrections to the shape of the instrumental response were corrected with observations of the A0V star HD240290, relative to a synthetic Vega spectrum calculated with the same code. Finally, the absolute flux scale was set with an observation of G191B2B, utilizing the STIS/NICMOS fluxes (Bohlin 2007).

### 2.2.3 *Spitzer* Mid-Infrared Imaging

We used archival *Spitzer*/IRAC images of Cas A originally presented by Ennis et al. (2006). While data exist for all four IRAC bands, the broader point spread function for the longer wavelengths degrades our ability to disentangle the synchrotron emission peaks from both the emission-line emitting regions and the smooth continuum background, so we limit our analysis to channels 1 and 2 ( $3.6\mu\text{m}$  and  $4.5\mu\text{m}$ , respectively). Data products were downloaded from the archive, processed and mosaicked using standard IRAC processing.

## 2.3 The Extinction Toward Cas A

### 2.3.1 Reddening Measurements from Emission Lines

Reddening measurements of emission-line nebula require observations of at least two lines of known intrinsic ratio and significantly different energies. With the adoption of a reddening curve (e.g., Cardelli et al. 1989, which we use here) and an assumption about general-to-selective extinction ( $R_V = A_V/E(B - V) = 3.1$  is the standard value for the diffuse ISM), the observed flux ratio of the selected lines gives the extinction.  $H\alpha$  and  $H\beta$  (and higher order lines of the Balmer series) are most often used since they are generally among the brightest lines in nebular spectra and, in the usually applicable case where their emission is primarily by recombination, the intrinsic ratio is well known. However, these lines are problematic in Cas A for two reasons. First, the fast-moving knots that dominate

Cas A's optical spectra are composed of pure metals and are devoid of hydrogen lines. Second, while the quasi-stationary flocculi ("QSFs", shocked pre-SN circumstellar material) do emit in the Balmer series, the slow radiative shocks that illuminate these knots produce  $H\alpha$  by both recombination and collisional excitation, making the intrinsic  $H\alpha/H\beta$  (Balmer decrement) ratio uncertain. A value of 3.0 is usually assumed for radiative shocks, but this increases to slower shock speeds as collisional excitation becomes more important. HF96 report measurements of the Balmer decrement for two QSFs in Cas A, but regard their implied values ( $A_V = 5.3, 6.2 \pm 0.9$ ) as upper limits.

Alternatively, it is possible to measure the extinction with metal line ratios. In the case where collisional de-excitation is negligible, the intrinsic flux ratio of lines originating from the same upper term depends only on their energies and transition probabilities. Unfortunately, calculation of the Einstein A coefficients for the forbidden lines most often observed in optical/IR emission-line nebula is a difficult task, and results can vary by 20% or more for different calculations of the same transitions. Moreover, if collisional de-excitation is important the intrinsic flux ratio depends both on the electron density and theoretically calculated effective collision strengths, which may have systematic uncertainties equal to or greater than those of the transition probabilities.

The best extinction measurements for Cas A to date are from HF96, who examine the  $1.03\mu\text{m}$  blend and  $\lambda\lambda 4069, 4078\text{\AA}$  doublet of [S II], both of which originate in the  $^2P$  (second excited) term of  $S^+$ . (Collisional de-excitation of these transitions is unlikely to be important in the Cas A FMK's, as their critical densities are of order  $10^6\text{ cm}^{-3}$ .) The issue of the accuracy of the necessary atomic data is apparent in HF96, who assume a ratio 25% greater than had been used in an earlier study by Searle (1971). Aside from systematics related to the atomic data, two

practical considerations limit the utility of the [S II] diagnostic. As noted above, the lines of interest originate from the second excited term of  $S^+$ , so, unlike the ubiquitous [S II]  $\lambda\lambda 6717, 6731\text{\AA}$  doublet, at lower temperatures it is possible to have a significant  $S^+$  ionization fraction with little population of the higher term, resulting in weak lines. More importantly, the  $4070\text{\AA}$  lines are far into the blue, and are thus highly absorbed toward Cas A. Indeed, for  $A_V = 8$ , the highest derived extinction inferred from the radio study of Troland et al. (1985),  $A_{4070} > 11$ . HF96 only report reddenings in the northeastern bright ring of Cas A, where the radio-inferred extinction is the least. This is likely a selection effect, as it becomes increasingly difficult to measure the faint  $4070\text{\AA}$  lines in heavily absorbed regions. Since radio studies show the reddening toward Cas A to be patchy and variable across the remnant, in order to constrain more tightly the extinction at the explosion it is highly desirable to be able to measure reddenings closer to the expansion center or, at least, sample a more representative range of sight lines.

With the general availability of efficient near-infrared spectrographs, it is now possible to observe a wider selection of emission lines into regions of higher extinction. The strong  $1.257\mu\text{m}$  and  $1.644\mu\text{m}$  lines of [Fe II] both originate in the  $a^4D_{7/2}$  level of  $Fe^+$ , are bright in a range of emission-line nebulae, and in principle should be ideal reddening indicators for moderately absorbed sources. However, the intrinsic flux ratio of these important lines is a matter of some debate. Two modern calculations of the relevant transition probabilities (Nussbaumer & Storey 1988; Quinet et al. 1996) are discrepant by 30%. Because of the relatively small wavelength spacing of the two lines, this translates to a systematic error in  $A_V$  of several magnitudes. Hartigan et al. 2004 use the Quinet ratio ( $F_{1.2575}/F_{1.644} = 1.04$ ) in their models, since it implies an  $A_V$  in HH111 that is consistent with optical Balmer decrement measurements (Gredel & Riepurth

1993). However, Nisini et al. (2005) find that neither the Quinet nor the Nussbaumer & Storey ratios produce  $A_V$ 's consistent with optical data in HH1. In light of such theoretical uncertainty, an empirical determination is desirable. To our knowledge, there are no published  $1.257\mu\text{m}/1.644\mu\text{m}$  flux ratios for relatively unabsorbed sources (e.g., The Cygnus Loop or the Orion Nebula), but Smith & Hartigan (2006, hereafter SH06) present high S/N J and H band spectroscopy of P Cygni's nebula, and derive empirical Einstein A coefficients from their observations using the known optical reddening. This is, of course, dependent on their assumed extinction ( $A_V = 1.86$ , Lamers et al. 1983), itself reliant on the accuracy of B star NLTE model atmospheres, being correct. However, given the current uncertainty in the actual intrinsic ratio, we accept the SH06 measurement ( $F_{1.257}/F_{1.644} = 1.49$ ) as the best available, and use it throughout this work.

### 2.3.2 [Fe II] Reddening Measurements

We extracted numerous spectra from our coadded observations, seeking to maximize the signal to noise in the [Fe II] lines of interest. In Figure 2.2, we mark the positions of the 19 individual knots in which we measure the  $F_{1.257}/F_{1.644}$  ratio to better than 20%. Of these, 15 are fast-moving ejecta knots and four are QSFs, located both in the northern bright ring (where HF96 made their measurements) and the more highly reddened western and southern portions of the remnant. In Figure 2.3, we show the measured flux ratio against position angle in the remnant. While there is considerable scatter due to Poisson noise in the lines, there is significant real variation on small spatial scales, as well as a general increase in reddening from east to west. Both these attributes are broadly consistent with the radio measurements of Troland et al. (1985), who estimated  $A_V \sim 4 - 5$  for much of the remnant, increasing to  $A_V \sim 8$  in their western most observation. However, they argue that much of the molecular gas along the line of sight must

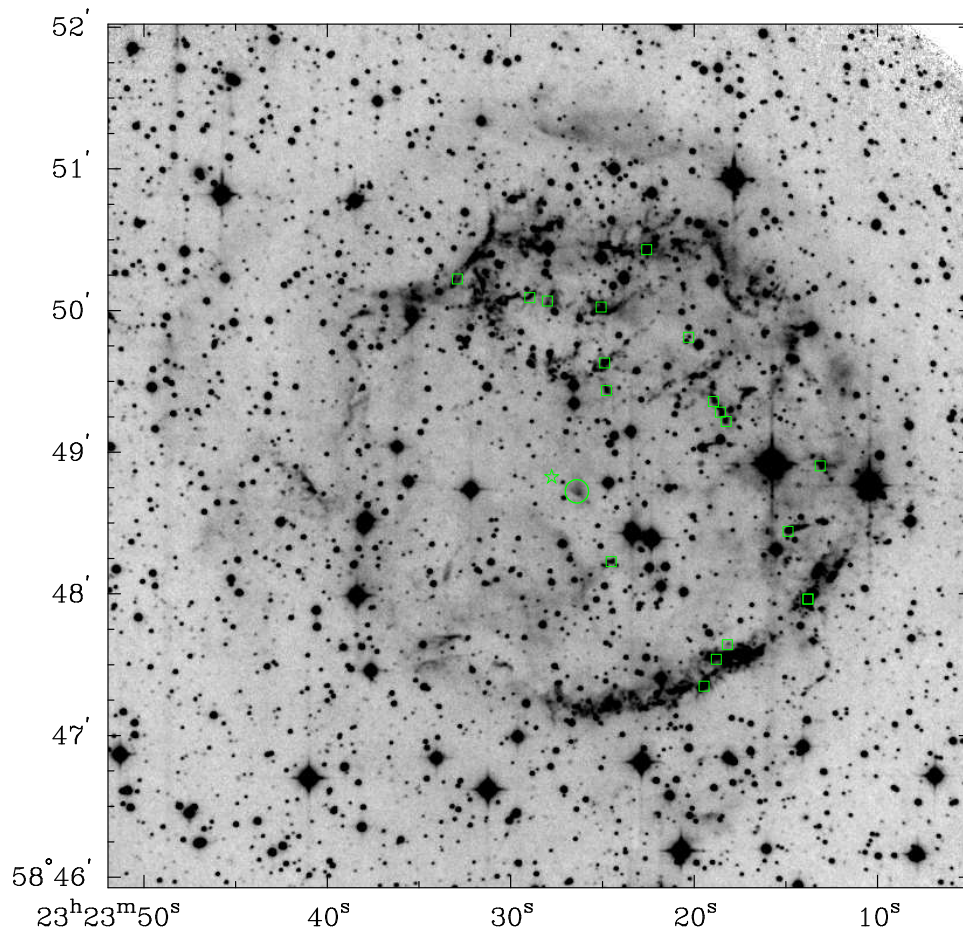


Figure 2.2 PISCES *H*-band image of Cas A. Our knots with successfully measured [Fe II] ratios are marked with boxes, and synchrotron knot N is marked with a circle. The star symbol marks the expansion center as measured by Thorstensen et al. (2001).

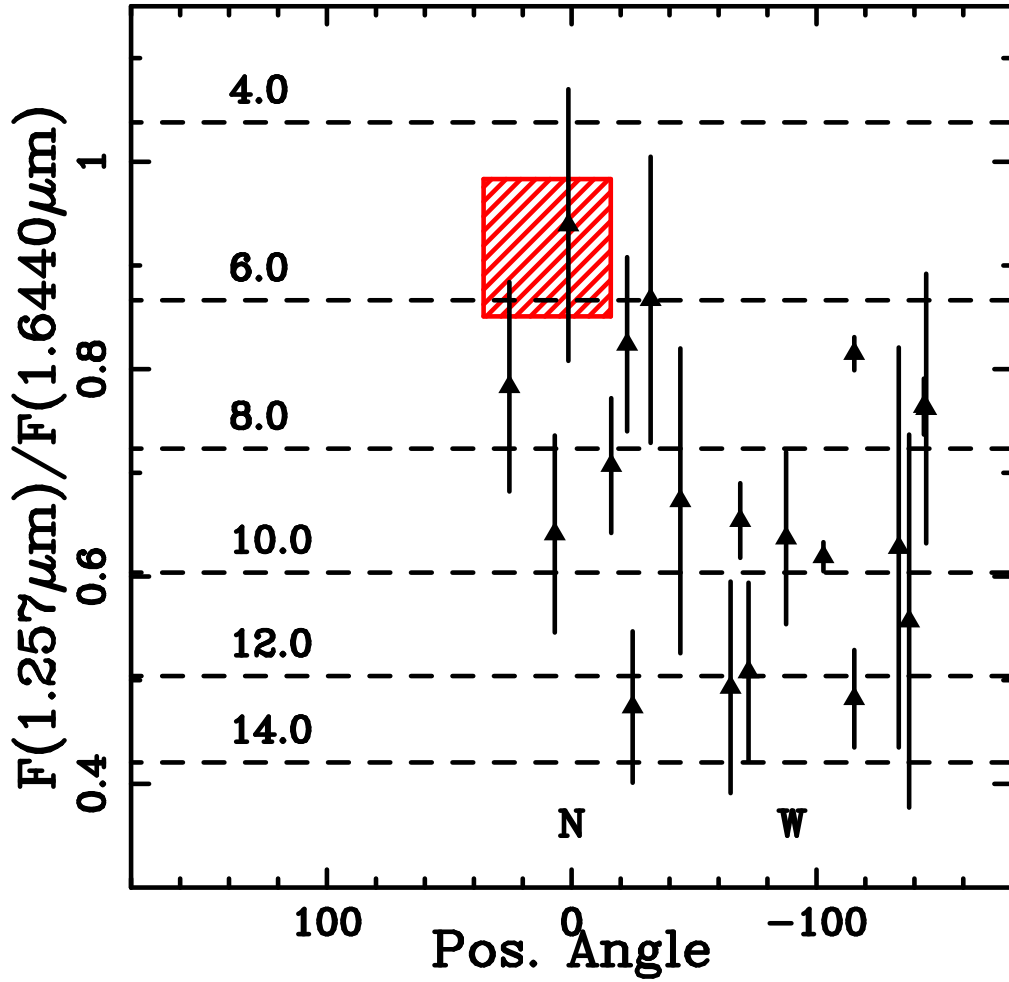


Figure 2.3 The observed flux ratios for 19 [Fe II] knots. The horizontal lines denote  $A_V$  assuming the empirical intrinsic flux ratio of Smith & Hartigan (2006). Adoption of the Nussbaumer & Storey (1988) ratio would decrease  $A_V$  by more than a magnitude. The hatched region shows the range of position angles sampled by HF96, and the range of reddenings from their optical [S II] lines.

be clumped in dark clouds smaller than their  $1'.1$  beam, so the extinction would be expected to be greater in places, and vary on scales smaller than an arcminute. This hypothesis is confirmed by the VLA  $\text{H}_2\text{CO}$  observations of Reynoso & Goss (2002).

Aside from the striking variation in reddening, an overall offset in the implied  $A_V$  as compared with the [SII] measurements from HF96 is clear. While there is no direct overlap in knots observed between the two samples, a number of our features are in the same area of the bright northern ring as the HF96 observations. Yet, there is a marked difference of several magnitudes. The most likely explanation for this is the still quite uncertain atomic data for the forbidden lines of interest. A small portion of this error may come from the [SII] measurements. Our own calculation of the intrinsic [SII] ratio using more modern atomic rates (Keenan et al. 1993; Keenan et al. 1996) suggests  $F_{1\mu\text{m}}/F_{4070} = 0.58$ , a revision down by approximately 10% compared with HF96's adopted value. However, given the large separation in wavelength of the two blends, this only accounts for a few tenths of a magnitude in  $A_V$ . Rather, the likely culprit is the large uncertainty in the intrinsic relative strength of the two [Fe II] lines. Indeed, if we were to assume the theoretical value of Nussbaumer & Storey (1988) rather than the empirical ratio of SH06, the derived  $A_V$  would decrease by more than a magnitude, and would bring our least reddened values closer in line with HF96. This adjustment is problematic though, in that it would imply essentially zero extinction to P Cygni given SH06's observed flux ratios, in conflict with ultraviolet and optical observations. Clearly, an empirical measurement on a less absorbed object is required to fix this distressing situation. Until its resolution, we caution that absolute measurement of  $A_V$  with these lines, for this SNR or any of the large number of astronomical objects that would benefit from NIR emission-line

extinction diagnostics, requires better atomic data. However, apart from an absolute measurement, the variation in the observed flux ratio is a clear indication of the high spatial variation of the reddening toward Cas A, and demonstrates that an accurate estimate of the extinction of Cas A's nascent supernova requires a measurement of  $A_V$  as close to the expansion center as possible. Our ability to reliably measure this ratio across the face of the remnant, even toward regions of comparatively high absorption, is a clear advantage over optical measurements.

Finally, we note the existence of two knots, one FMK and one QSF, within  $45''$  of the measured expansion center of Cas A. The reddenings for these knots are  $A_V = 7.4^{+2.1}_{-1.7}$  and  $A_V = 6.0^{+1.9}_{-1.6}$  (statistical errors only). These are the closest emission line features to the projected explosion site to date with measured reddenings.

### 2.3.3 Reddening Measurement from Infrared Synchrotron Emission

Relativistic electrons accelerated in Cas A's shocks produce copious amounts of synchrotron emission, and place Cas A among the brightest sources in the centimeter and millimeter sky. Cas A's X-ray spectrum has a hard, broken power-law component (Allen et al. 1997) in addition to its thermal plasma signature, and *Chandra* has revealed a number of discrete filaments with featureless spectra (e.g., Hughes et al. 2000), which are generally assumed to be synchrotron emission (though, see also Laming 2001). It is then perhaps not surprising that synchrotron emission would be detected in the  $\sim 8$  decades of energy in between. Gerardy & Fesen (2001) were the first to present high-quality near-infrared images of Cas A, and while their *J*-band image was similar in morphology to clumpy, filamentary optical images dominated by emission lines, they noted the striking similarity of their  $K_s$  image to radio continuum maps, and postulated they had detected infrared synchrotron emission. Jones et al. (2003, hereafter J03) confirmed this

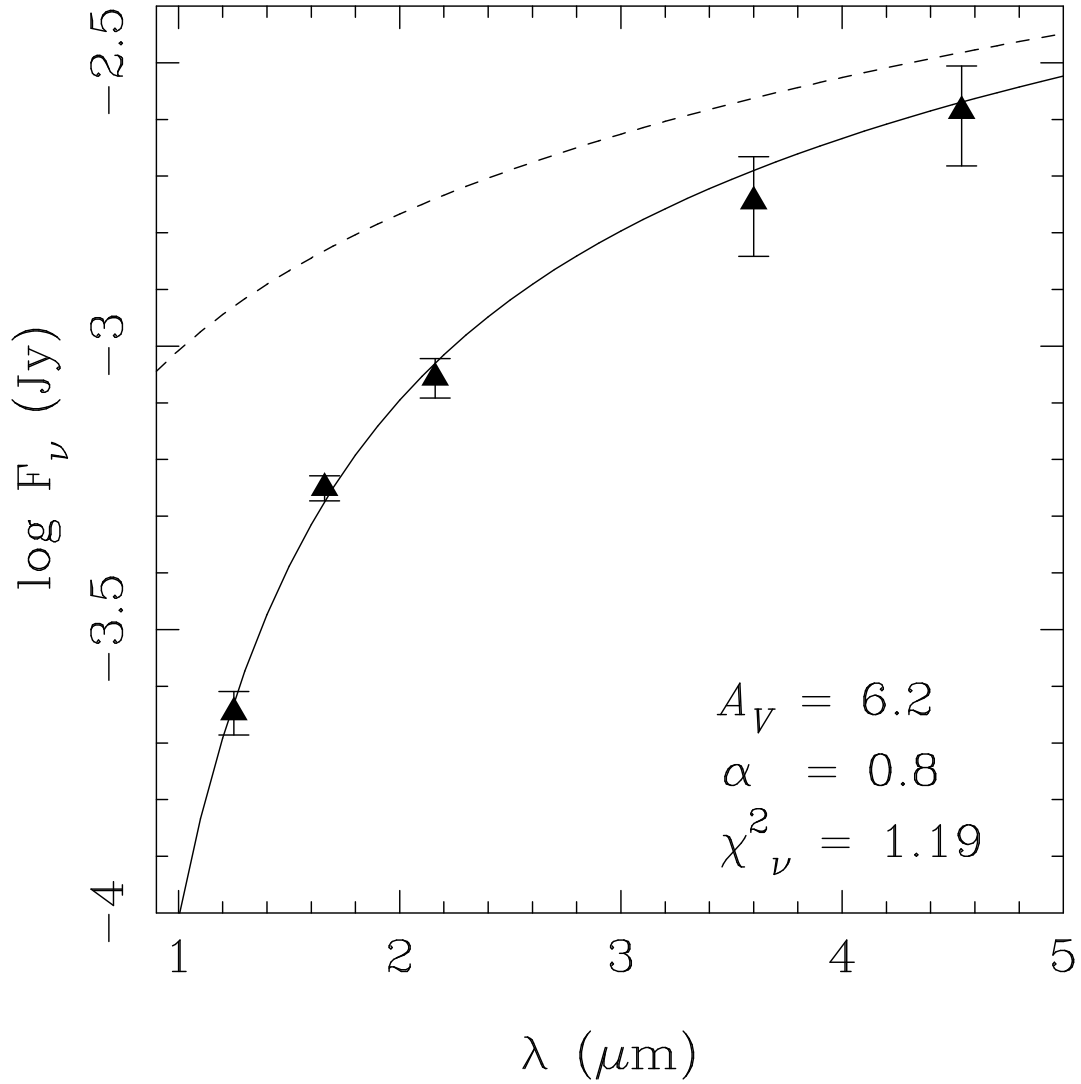


Figure 2.4 Measured infrared flux densities for Cas A synchrotron knot N. The solid line shows the best fit model for  $A_V = 6.2$  and  $\alpha = 0.80$ , while the dashed line is the unabsorbed model.

identification with  $K$ -band imaging polarimetry of a small portion of the western shell. They also found the  $2\mu\text{m}$  flux to be brighter than expected from simple extrapolation from the radio. Rho et al. (2003, hereafter R03) apparently confirm the “concave-up” nature of the Cas A synchrotron spectrum, though, since their measurement is summed over the entire remnant, systematics like incomplete star subtraction, contamination from line-emission, spectral index variation, and large-scale flat field errors are likely sources of systematic error. Indeed, Wright et al. (1999, hereafter W99) show significant variation of spectral indices for several knots in the millimeter-wave regime.

Departures from a broadband power law spectrum, either concave up or down, can be produced by a variety of plasma effects (e.g., Eichler 1984, Reynolds 1998), and the detailed broadband shape of Cas A’s nonthermal SED is still an open question. Of course, at optical through mid-infrared wavelengths, the situation is complicated by the substantial extinction along our sight line to the remnant. (For  $A_V = 4.5$  and a standard reddening law,  $A_{4.5\mu\text{m}} = 0.16$  and is obviously greater for shorter wavelengths.) Here, we reverse the question: we assume the departure from a power law is small over our limited range of energies, and determine  $A_V$  by fitting for the observed fall-off toward shorter wavelengths.

Practical measurement of the infrared synchrotron spectral index in Cas A is complicated in that in  $J$ ,  $H$ , and IRAC channel 2, most regions of bright synchrotron emission are also bright in emission lines. However, a number of isolated continuum knots are line free. Fortuitously, one of the brightest of these (“knot N” from W99, marked with a circle in Figure 2.2), is only  $13''$  from Cas A’s expansion center (Thorstensen et al. 2001) making this the closest feature to the projected SN observed from the optical through mid-IR. Thus, a measurement of  $A_V$  at this location provides the strongest constraint on the actual reddening of

Cas A's SN.

In Figure 2.4, we plot the  $1 - 5\mu\text{m}$  flux densities for a circular aperture of radius  $10''$  centered on knot N, with the background (determined from an annulus of inner radius  $10''$  and outer radius  $20''$ ) subtracted. For the ground-based  $JHK_s$  bands, we convert 2MASS magnitudes to Janskies using the flux zero-points from the 2MASS documentation (Cutri et al. 2006). The error bars reflect the Poisson noise from the source and sky, and do not include any systematic error due to large-scale flat-field error or nonzero color terms in the flux calibration. We estimate these systematics to be subdominant. For the IRAC bands, flux density is a product of the post-BCD processing. The Poisson errors are negligible. However, due to the extended wings in the *Spitzer*/IRAC point-spread function, there is substantial systematic error in the flux densities. We correct the fluxes from the images down by 2% (ch1) and 5% (ch2), and assume a conservative 20% error in the absolute value <sup>4</sup>.

In order to estimate  $A_V$ , we fit our data with a reddened power law and used a Markov Chain Monte Carlo (MCMC) technique to sample the three-dimensional parameter space of the fit. In Figure 2.5, we plot the likelihood contours in the  $A_V - \alpha$  projection, marginalizing (i.e. integrating the likelihood function) over the normalization parameter. With flat priors on the parameters, there is a strong degeneracy between the extinction and spectral index, as higher  $A_V$  compensates for flatter spectra. This leads to only loose constraints on reddening. Indeed, the distribution of  $A_V$  marginalized over both  $\alpha$  and  $k$  is quite broad and, without further constraints, we estimate  $A_V = 7.9 \pm 1.9$ .

The data and flat priors alone clearly allow nonphysical values of the spectral index, and improbable reddenings. In order to limit the range of likelihood space

---

<sup>4</sup><http://ssc.spitzer.caltech.edu/irac/calib/extcal/index.html>

available to the fit, it is clearly desirable to apply more stringent priors to the parameters. While one could choose somewhat arbitrary allowed ranges on the parameters (top-hat priors), we choose instead to apply a physically motivated prior on the spectral index, from the millimeter-wave radio observations. W99 report  $\alpha = 0.80$  for knot N. While they do not quote an error specific to this knot, they claim their general accuracies to be  $\pm 0.02 - 0.05$ . We ran a second set of Markov chains with a Gaussian prior with  $\sigma_\alpha = 0.05$ . This shrinks the likelihood contours significantly, and tightly constrains the marginal probability distribution of the reddening (Figure 2.5). For this prior, we find  $A_V = 6.2 \pm 0.6$ .

Given the evidence for departures from a power law in the broadband synchrotron spectrum of Cas A discussed previously, the actual uncertainty in the spectral index may indeed be greater than the statistical error quoted by W99. The concave-up spectra preferred by both J03 and R03 flatten the powerlaw, and would translate to a lower index in our model. Inspection of our likelihood contours shows that this would drive our fit to higher  $A_V$ . (Indeed, with the flat priors, our data prefers a flatter  $\alpha$  and more extinction.) One could construct more exotic priors that preferentially open parameter space toward lower spectral indices, but absent a strong theoretical guide of their functional form, and given the relatively paucity of data points, we rapidly approach art over science. Shorter wavelength data, whose extinction increase faster than the intrinsic spectrum drops, may have power to constrain more tightly either the spectral index or any significant departure from a power law. Imaging of Cas A's synchrotron emission should be feasible in the red end of the optical with moderate-sized telescopes. Ideally, one would like a  $0.8 - 2.5\mu\text{m}$  dispersed spectrum of the emission, though this would require a significant investment of time on a large aperture facility.

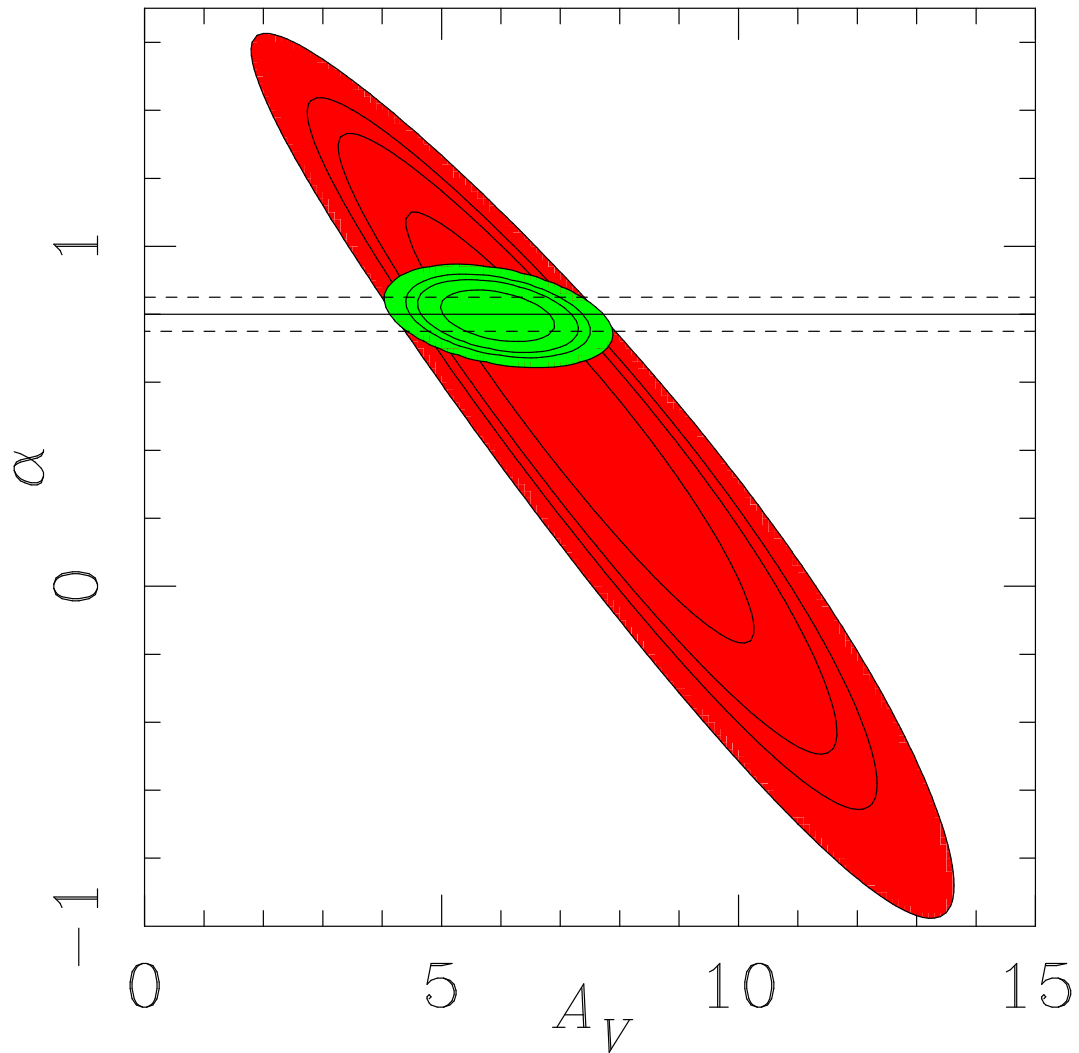


Figure 2.5 Likelihood contours for Cas A knot N for flat priors (red) and a Gaussian prior on the spectral index (green). The contours correspond to 68%, 90%, 95%, and 99% confidence for each set of priors. The horizontal line is the millimeter spectral index from Wright et al. (1999, solid), and their  $1\sigma$  errors (dashed).

## 2.4 Discussion

### 2.4.1 Cas A's Supernova at Maximum Light

Accepting our new extinction measurement from synchrotron knot N as the most likely  $A_V$  toward Cas A's nascent supernova, we now seek to constrain a range of possible intrinsic peak luminosities and, therefore,  $^{56}\text{Ni}$  yields. Following Young et al. (2006),

$$L_{peak} = M_{Ni} \Theta(t_{peak}) \Lambda(t_{peak}) \quad (2.1)$$

where  $M_{Ni}$  is the ejected mass of  $^{56}\text{Ni}$ ,  $\Theta(t)$  is the instantaneous energy decay rate of  $^{56}\text{Ni}$  and  $^{56}\text{Co}$ , and  $\Lambda(t)$  is the efficiency with which that energy is deposited in the supernova gas.  $\Theta(t)$  is defined as

$$\Theta(t) = \frac{N_A}{56} \left[ \frac{E_{Ni}}{\tau_{Ni}} e^{-t/\tau_{Ni}} + \frac{E_{Co}}{\tau_{Co} - \tau_{Ni}} \left( e^{-t/\tau_{Co}} - e^{-t/\tau_{Ni}} \right) \right]. \quad (2.2)$$

Here,  $N_A$  is Avogadro's number, while  $E$  and  $\tau$  are the  $\gamma$ -ray energy and mean decay lifetime of their respective nuclei (1.73 MeV and  $7.6 \times 10^5$  s for nickel; 3.69 MeV and  $9.6 \times 10^6$  s for cobalt). We choose  $t_{peak} = 20.7$  days (the rise time for the SN Iib 2008ax, Pastorello et al. 2008), and  $\Lambda(t_{peak}) = 0.95$  (the value for the most likely Cas A progenitor from Young et al., determined with  $\gamma$ -ray radiative transfer calculations).

First, we estimate the minimum possible luminosity. Willingale et al. (2003) inventory  $0.058 M_{\odot}$  (no error bar reported) of X-ray emitting iron in Cas A from X-ray observations, and conclude that most of this material is ejecta. Assuming plausible isotopic ratios, the vast majority of this material is  $^{56}\text{Fe}$ , the stable daughter product of  $^{56}\text{Ni}$ . If we allow Willingale's iron mass to be the sum total of  $^{56}\text{Ni}$  ejected, the supernova's absolute magnitude would be  $M_V = -16.5$ . At

a distance of  $3.4_{-0.1}^{+0.3}$  kpc, with  $A_V = 6.2 \pm 0.6$ , this translates to a peak apparent visual magnitude of  $m_V = 2.3 \pm 0.7$ . (We have included a 25% error in the X-ray emitting iron mass.)

Recently, Krause et al. (2008) observed the actual optical peak of Cas A's supernova through a light echo, and definitively classified it as a rare Type IIb. They use the nearby SN IIb SN1993J, which had a peak  $M_V = -17.5$  (Richmond et al. 1994) as a template, assumed the maximum reddening ( $A_V = 8$ ) inferred from the radio, and derived a peak visual magnitude of  $m_V = 3.2$ . Our study indicates the extinction is considerably less, with concomitant increase in apparent brightness. There is, however, significant variation in the peak luminosity of the peculiar SN IIb class, with SN1996cb peaking at  $M_V \approx -16.3$  (Qiu et al. 1999), so some care must be applied in treating the SN IIb as a homogenous population.

Clearly, Flamsteed's apparent observation of 3 Cas was not Cas A's SN at maximum light, though it may have been the supernova in decline. Krause et al. note that their light echo grew fainter by a factor of 18 in 140 days and that this  $\sim 3$  mag fading matches a similar decline in the light curve of 1993J. Morgan (2008) explore the observability of the putative SN1680 with new atmospheric radiative transfer calculations and a detailed discussion of the timing within the year. We summarize his argument here, with our new extinction result. Given Flamsteed's 1680 August 16 6 mag observation, and our assumed peak apparent magnitude of  $m \sim 1 - 3$ , SN1680's peak would have occurred in February–April. During this time, Cas A's position would have transited during daylight, and would not have been visible at maximum altitude by several magnitudes, given any of our estimates of its apparent magnitude. However, with Cassiopeia's circumpolar location in the northern sky, SN1680 would still have been quite high in both the morning and evening twilight. If Cas A's supernova were on the bright end

of our estimates, while it may not have been visible during daylight like other historical supernovae, it would briefly have been one of the 20 brightest stars in the northern sky, and likely would have been reported. Conversely, if its peak magnitude were toward the fainter end of our range, it may have been just faint enough to escape notice.

#### 2.4.2 $^{56}\text{Ni}$ and $^{44}\text{Ti}$

Given the probable range of luminosity for the supernova, we now seek to bound the total mass of ejected  $^{56}\text{Ni}$ . The detection of  $0.058 M_{\odot}$  of iron in the X-ray sets a hard floor. It is more difficult to derive a stringent upper limit, given the lack of a rigorous detection threshold. A 0 mag supernova would have garnered a great deal of contemporary attention; clearly Cas A's supernova did not. Would a  $2^m$  or  $3^m$  transient escape notice? Absent a clear answer, with the definition of the distance modulus and inverting Equation 2.1

$$M_V = m_v - A_V - \mu \propto \log_{10} M_{Ni} \quad (2.3)$$

we combine our ignorance into the  $m_V - A_V$ . In Figure 2.6, we plot this difference against the calculated ejected mass of nickel. The lower limit on  $M_{Ni}$ , combined with our best fit  $A_V$  implies  $m_V < 2.4$ . This is uncomfortably bright, but not an entirely unreasonable magnitude for an object that may have gone unnoticed in the twilight. If, instead we assume at  $1\sigma$  increase over our best  $A_V$  and assume that any transient with  $m < 2$  would merit at least a historical footnote, we place an upper limit on  $M_{Ni} < 0.16 M_{\odot}$ . We regard this as a conservative estimate. Plausibly shorter rise times and larger energy deposition efficiencies can lower this limit by  $\sim 20\%$ .

Gamma-ray observations have detected the nuclear decay lines of  $^{44}\text{Ti}$  daughter nuclei  $^{44}\text{Ca}$  and  $^{44}\text{Sc}$  (Iyudin et al. 1994, Vink et al. 2001) The latest  $\gamma$ -ray

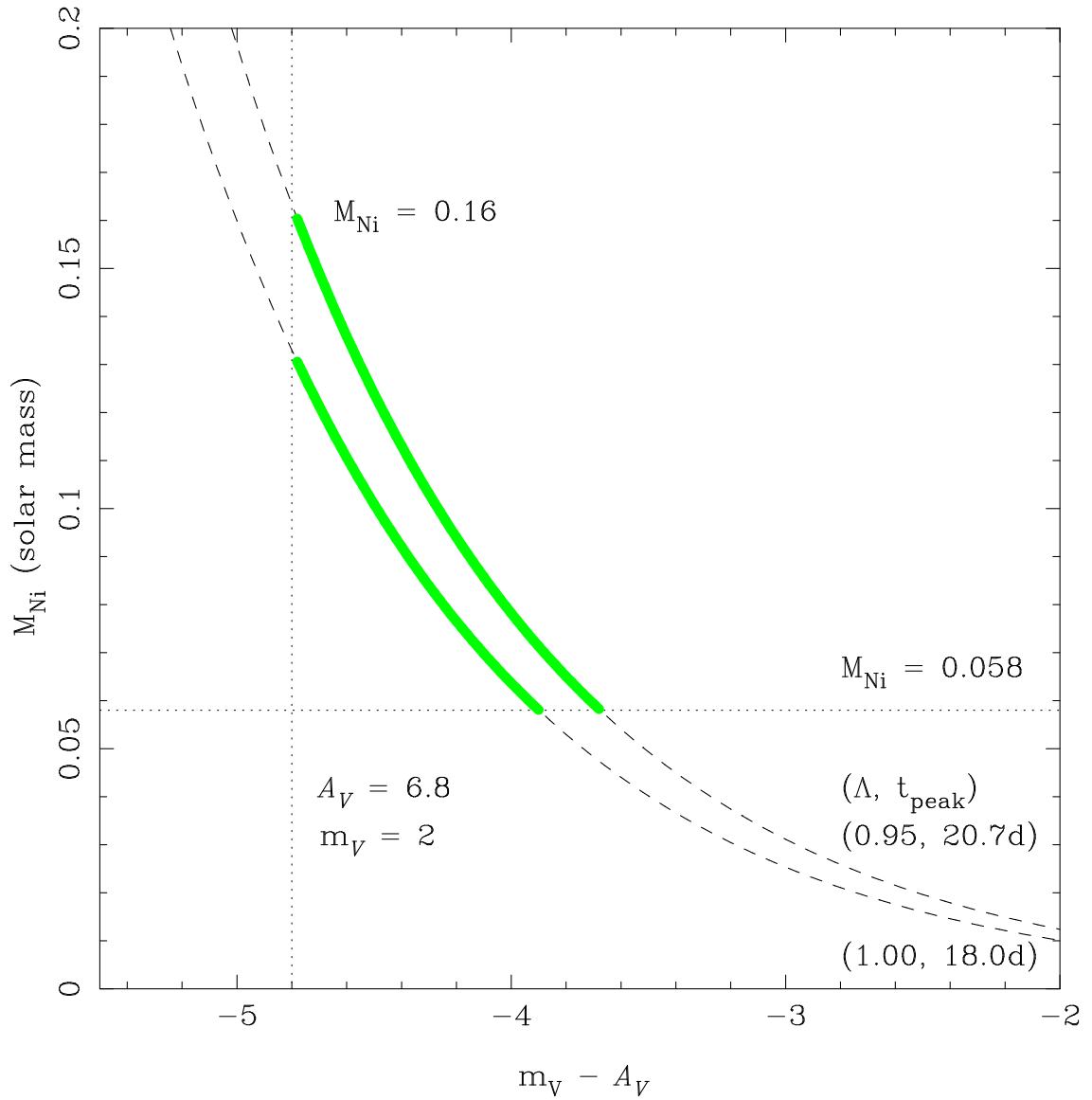


Figure 2.6  $^{56}\text{Ni}$  mass for two sets of assumptions for the supernova rise time and efficiency of  $\gamma$ -ray energy deposition. The horizontal dotted curve denotes the X-ray emitting iron mass, while the vertical dotted line represents the brightest plausible optical transient that might be missed ( $m_V = 2$ ), and our best fit  $A_V + 1\sigma$ . The green solid line marks the allowed range of  $^{56}\text{Ni}$  mass.

observations imply an initially synthesized  $^{44}\text{Ti}$  mass of  $1.6_{-0.3}^{+0.6} \times 10^{-4} M_{\odot}$  (Reinaud et al. 2006), for a  $^{44}\text{Ti}/^{56}\text{Ni} = 0.8 - 3.8 \times 10^{-3}$ . This high mass and ratio is problematic for spherically symmetric explosion calculations (Timmes et al. 1996), though in multidimensional asymmetric simulations some mix of differentially enhanced  $\alpha$ -rich freeze-out (Nagataki et al. 1998) and differential fall-back (Young et al. 2006) appear capable of reproducing a range of yields, some consistent with the observed value. Notably, the combination of the new *INTEGRAL* titanium measurements and our tighter bound on the ejected  $^{56}\text{Ni}$  mass shrink considerably the allowed abundance ratio space considered by Young et al (2006), and may provide important constraints on advanced supernova explosion calculations. Finally, we note that our radioactive Ti/Ni bound is consistent with the solar  $^{44}\text{Ca}/^{56}\text{Fe}$  ratio ( $1.5 \times 10^{-3}$ , Anders & Grevesse 1989) the stable isotopes of the considered decay chains. While is it dangerous to extrapolate from one observation, if this result is generally valid, Cas A-like supernovae may lessen the need for the sub-Chandrasekhar mass SN Ia required by Timmes et al. (2006) to match the solar abundance.

Finally, we note an alternative explanation for the apparent faintness of Cas A's supernova. While nearly all long duration gamma-ray bursts show late-time supernova light curves, a small number do not (e.g., GRB060606 and GRB060615, Fynbo et al. 2006). Calculations by Fryer et al. (2007) show that sufficiently delayed explosions (after core collapse) produce a large mass of material on gravitationally bound ballistic trajectories, which falls back onto the compact remnant (a black hole for GRBs) on a timescale of minutes after the explosion. A correspondingly small amount of nickel escapes into the remnant. In these cases, the light curve is powered not by radioactive decay, but by energy deposited by the blast wave. These supernova are fainter and decline faster. In principle, similar

such delayed supernovae could exist independently of GRBs, and their outbursts would be easier to hide. This idea is attractive in that the spectra of a number of the oxygen-rich supernova remnants lack iron, or even oxygen-burning ashes such as sulfur, argon, and calcium (e.g., N132D and E0102, Blair et al. 2000), which may well have fallen back onto the compact remnant. However, given the significant mass of iron detected in the X-ray spectrum of Cas A, its supernova was unlikely to have been such an event, so interstellar extinction remains the likely culprit in its apparent faintness.

## 2.5 Conclusion

We have presented new extinction measurements for Cassiopeia A that show the reddening to be more variable and of higher magnitude than had been derived from previous optical measurements, though our estimates of  $A_V$  are consistent with previous radio observations. The [Fe II] lines should be promising probes of reddening for regions of moderate extinction, though their use is still hampered by uncertainty in the intrinsic emissivity ratio of the two lines. Further atomic structure calculations, or more appropriately, observations of unabsorbed emission line sources are necessary to yield the full utility of these features. Nevertheless, the observed ratio is sufficient to show the east–west reddening gradient previously inferred in the radio, as well as small scale point-to-point variations.

We have also shown that estimation of  $A_V$  from the infrared synchrotron index combined with constraints from the radio yields statistical errors comparable to or better than those from the emission lines. Fortuitously, a bright synchrotron knot free from emission-line contamination is located just 13'' away from the derived expansion center of the remnant, and thus provides the strongest constraint on  $A_V$  toward Cas A's nascent supernova. Our new reddening, taken with the

lack of widespread reportage of the supernova and with an iron mass inventory from the X-ray, bounds the ejected mass of  $^{56}\text{Ni}$  to be  $0.058 - 0.16M_{\odot}$ . This nickel abundance and measurement of the  $^{44}\text{Ti}$  yield from  $\gamma$ -radiation both provide constraints on possible asymmetry in the supernova explosion, and imply a  $^{44}\text{Ca}/^{56}\text{Fe}$  ratio consistent with solar, which may have consequences for Galactic chemical evolutionary models.

## CHAPTER 3

## ILLUMINATING THE COLD EJECTA IN CAS A

We present a theoretical study of the ejecta recently detected interior to the reverse shock in the young oxygen-rich supernova remnant Cassiopeia A with the *Spitzer* IRS. Using simple physical arguments, we conclude that the ejecta is cold (100 – 500 K), and is photoionized by the EUV/X-ray emission from the forward and reverse shocks. A one-dimensional hydrodynamic simulation of the SNR evolution incorporating time-dependant radiative transfer and non-equilibrium ionization, coupled with simple one-zone calculations, shows the mid-IR bright material to be clumped at  $\sim 100\times$  the mean density of the interior ejecta, analogous to the dense knots which give rise to optically-emitting radiative cloud shocks when they encounter the reverse shock. Model spectra for the ashes of incomplete oxygen burning are broadly consistent with the observed line ratios, though the calculated [S III]  $18\mu\text{m}/33\mu\text{m}$  ratio is systematically low, suggesting a more detailed treatment of suprathreshold photoelectrons is necessary. The lack of observed iron lines indicates that any Si-burning products still interior to the reverse shock must be more tenuous than the O-burning products detected with *Spitzer*.

### 3.1 Introduction

Young supernova remnants (i.e. those whose ejecta are not yet diluted with interstellar matter) provide our most direct look at the ashes of advanced nucleosynthetic burning and are therefore among our most valuable laboratories for testing stellar and supernova physics. Their hydrodynamic structure is typically dominated by two shocks. The freely-expanding supernova ejecta drive a blast

wave into the surrounding medium, which sweeps up circumstellar material. This forward shock decelerates as it entrains mass, and the downstream ejecta, still traveling at free expansion velocities, catch up with the shell. The resulting over-pressure drives a reverse shock toward the center of the SNR. These two waves give young SNRs their characteristic double-ring X-ray morphology. Because the cooling times for the  $\sim 10^7$  K temperatures typical for the reverse shock are longer than the SNR's dynamical age, X-ray spectra allow direct study of the composition of the sum of the ejecta that have passed through the reverse shock to the present day.

Given the dramatic increase in size from explosion to supernova remnant,  $PdV$  cooling is fierce, and in the absence of additional heat sources, even core material that experiences temperatures of billions of degrees after the passage of the outgoing supernova shock could cool to tens of degrees Kelvin before it reaches the reverse shock. At early times the decay of  $^{56}\text{Ni}$  and its daughter product  $^{56}\text{Co}$  drive the SN luminosity and are the primary sources of internal energy in the ejecta. For some years, long-lived trace radionuclides such as  $^{44}\text{Ti}$  and its decay chain inject a non-negligible amount of energy in the form of  $\gamma$ -rays and positrons. However, after a decade or two of free expansion the density is too low for efficient thermal coupling of the radioactive products to the cold gas. By this time, the old SN is becoming a young SNR, and some of the copious X-rays emitted in the shocks propagate into the remnant interior and become the primary heat source for the unshocked ejecta. For the first several decades of SNR evolution, interior densities are high enough that the gas is optically thick, and the thermal evolution of the interior material is a complex balance between heating due to self-shielded photoionization and cooling due to line emission and expansion. At most wavelengths emission from the interior ejecta is swamped

by the luminous reverse shock-heated material to the point of being nearly invisible. This has made complete inventories of the nucleosynthetic yield (centuries after the SN) difficult, and has introduced ambiguities into comparisons of SNR abundances with SN yield calculations.

Smith et al. (2009, hereafter S09) recently reported an unambiguous detection with the *Spitzer* Infrared Spectrograph (IRS) of ejecta interior to the reverse shock in the young Galactic oxygen-rich supernova remnant Cassiopeia A (Cas A). These observations afford us, for the first time, a look at the final missing pieces in the census of Cas A's ashes, and should prove invaluable in informing computational studies of its SN. However, there to date have been no theoretical tools with which to interpret these data. This paper is a first step towards remedying this situation.

The remainder of the paper is organized as follows. In Section 2, we advance simple physical arguments to discern the basic physical conditions in the IR-bright internal ejecta. We validate our basic assumptions with detailed simulations of the hydrodynamic, thermal, and ionization history of Cas A, presented in Section 3. Section 4 describes our calculations of model mid-IR spectra. In Section 5 we discuss the successes and shortcomings of our models, and address their implications for the O-burning and Si-burning yields of Cas A. Finally, Section 6 contains a short summary of the present work.

## 3.2 Basic Conditions

### 3.2.1 Spectroscopy by Eye

The the bright-ring (i.e. reverse shocked) and “once-shocked” (i.e. interior) mid-IR spectra presented by S09 show key differences. The reverse shock spectra have strong lines from a variety of ionization states across the IRS band, the brightest

of which is [Ar II] 6.99 $\mu$ m. This is typical of the cooling and recombination regions behind radiative shock waves, which can be as high as  $10^6$  K immediately behind the shock, and cool to  $\sim 100$  K downstream, with emission lines spanning the full temperature range. The interior regions have strikingly different spectra. The brightest line is instead [Si II] 34.81 $\mu$ m, with a strong trend of decreasing line strength to shorter wavelengths. Of note is the near absence of the [Ar II] 6.99 $\mu$ m and [Ar III] 8.99 $\mu$ m lines, particularly relative to [S IV] 10.51 $\mu$ m. Because of the similar ionization potentials of Ar<sup>2+</sup>, S<sup>3+</sup> and their neighboring ionic states, their ionization fractions should trace fairly closely. However, while [Ar III] 8.99 $\mu$ m is generally stronger than [S IV] 10.51 $\mu$ m, in the reverse shock material, [Ar III] is much weaker in the interior. While it may be tempting to attribute this to elemental abundance effects (particularly in an object as chemically heterogeneous as Cas A), sulfur and argon are both oxygen burning products, and are produced in nearly lockstep ratio for both hydrostatic shell and explosive burning (Arnett 1996). Rather, the difference in the two spectral regions is indicative of fundamentally different plasma conditions, providing support to the supposition that we are observing photoionized rather than shock-heated plasma. Indeed, we can make strong inferences about the conditions in the interior with techniques not much more complex than “spectroscopy by eye.”

The gas-phase emission lines observed by the *Spitzer* IRS arise from fine structure transitions in ions whose ground terms are split by the spin-orbit interaction. In the limit of negligible collisional deexcitation or population of upper levels from cascades, the temperature dependence for the flux of a spectral line is

$$F \propto \Upsilon(T_e) T_e^{-1/2} e^{-\Delta E/kT_e} \quad (3.1)$$

where  $\Upsilon(T_e)$  is the effective (i.e. thermally averaged) collision strength, and is

Table 3.1. Model Abundances

Element	$X_i$ depleted solar	$X_i$ incomplete O-burning
O	0.7969	0.5899
Ne	0.0953	0.0001
Mg	0.0334	0.0100
Si	0.0287	0.3000
S	0.0152	0.1000
Ar	0.0031	0.0100
Ca	0.0018	...
Fe	0.0256	...

a slowly varying function. At low temperatures,  $\mathcal{Y}$  tends to a constant for ions, though it can fall dramatically for neutrals. Clearly, for  $kT_e$  near or below the excitation energy of the upper level,  $F$  is dominated by the exponential cutoff from the Boltzmann factor. Thus electron temperatures near or below the typical fine-structure excitation energies will produce a spectrum with of decreasing line-strength to shorter wavelength, as the lines are exponentially quenched. This is what S09 observe. The weakness of [SIV] and [Ar III] relative to the longer wavelength features [OIV] and [Si II] apparent in their Figure 1 (they do not tabulate quantitative line strengths) strongly implies  $T_e \sim 100 - 500$  K in the interior gas.

### 3.2.2 Photoionization Equilibrium

In order to calculate the thermal and ionization state of the unshocked material, it is necessary to estimate the average conditions interior to the reverse shock. Young et al. (2006) provide a detailed discussion of the allowed range of the mass of Cas A's progenitor at the time of core-collapse, considering constraints from the observed mass in the X-ray emitting ejecta (Willingale et al. 2003) and the observed positions of the forward and reverse shocks (Chevalier & Oishi 2003), and new stellar evolution and supernova calculations. They conclude that the most likely progenitor for Cas A was a  $16 - 25M_{\odot}$  star that lost much of its envelope in a phase of common envelope evolution, leaving perhaps  $4 - 6M_{\odot}$  of material at the time of core collapse. (They note that this scenario implies Cas A's supernova was an unusual event. Since then, a detection of the SN's light echo Cas A's SN definitively showed the SN to be of the rare type IIb.) Assuming that  $\sim 1.5M_{\odot}$  of material is locked in the compact remnant (presumed to be a neutron star), and the mass of the X-ray emitting ejecta is  $2 - 4M_{\odot}$ , we estimate a reasonable upper limit of  $1M_{\odot}$  of unshocked ejecta. The reverse shock angular radius of  $\sim 100''$  (Gotthelf et al. 2001) and a distance of 3.4 kpc (Reed et al. 1995) gives  $r_{RS} \sim 5.3 \times 10^{18}$  cm. For smoothly distributed ejecta and an average mass per nucleus of  $\bar{A} \sim 18 m_p$  (typical for oxygen-rich gas with solar metallicity ratios for  $Z \geq 8$  and completely depleted for  $Z < 8$ ), the average ion density is  $n_{ion} = 0.1$ . Further assuming a typical photoionization cross-section of 1 Mb (1 megabarn =  $10^{-18}$  cm<sup>-2</sup>) at threshold,  $\tau_{max} = n_i \sigma_{edge} r_{rs} \sim 0.5$ . However, given that the total optical depth will be spread across a range of ionization states with different edges, and given the steep decline of the PI cross sections away from threshold, it is reasonable to assume the interior material is optically thin to the ionizing flux from the supernova remnant shocks. Therefore, taking Cas A to be

a spherically symmetric annulus of outer radius  $R_{out} = r_{BW} = 8 \times 10^{18}$  cm, inner radius  $R_{in} = r_{RS}$ , and emissivity  $\epsilon_\nu$ , the mean intensity of the ionizing radiation at arbitrary radius  $r$  inside the annulus is

$$J_\nu(r) = \frac{\epsilon_\nu}{2} \int_{-\pi}^{\pi} \left[ R_{out} \left( 1 - \frac{r^2}{R_{out}^2} \sin^2 \theta \right)^{1/2} - R_{in} \left( 1 - \frac{r^2}{R_{in}^2} \sin^2 \theta \right)^{1/2} \right] \sin \theta d\theta \quad (3.2)$$

which can be solved numerically.

The simplest assumption for the physical state of the unshocked ejecta is photoionization equilibrium:

$$\Gamma_{ij} = \int_{\nu_0}^{\infty} \frac{4\pi J_\nu \sigma_{\nu,ij}}{h\nu} d\nu \quad (3.3)$$

$$n_{ion} X_i f_j \Gamma_{ij} = n_{ion} n_e f_{j+1} \alpha_{j+1}(T_e) \quad (3.4)$$

$$n_{ion} X_i f_j \Gamma_{ij} \bar{q}_{ij} = n_{ion} n_e X_i f_j \Lambda_{ij}(T_e, n_e) - P/d\rho \quad (3.5)$$

where summations over total number fraction ( $X_i$ ) and ionization fractions ( $f_j$ ) for each element are implied. The  $\Gamma_{ij}$ 's are the photoionization rate,  $\bar{q}_{ij}$  the heat per photoionization,  $\alpha_j(T_e)$  the recombination coefficient, and  $\Lambda_{ij}(T_e, n_e)$  the cooling coefficient for each ion. (A detailed discussion of the atomic data used for these calculations can be found in the Appendix.) Given  $n_{ion}$ ,  $J_\nu$  (from Equation 3.2), and a composition, the equilibrium temperature and ionization fractions can be solved by iteration.

An important property of photoionization equilibrium may be gleaned from Equations 3.3-3.5. Since cooling and recombination have different density dependences than their inverse processes, the equilibrium temperature and ionization state depend on the density. At low densities the  $n_{ion}$  processes (photoionization and its accompanying heating) dominate, resulting in hotter, more highly ionized gas, while denser gas is cooler, with lower ionization. (Indeed, photoionized

plasmas are generally characterized by their ionization parameter  $\Xi \propto J_\nu/n_{ion}$ .) In the case of Cas A where we know (to a degree) the intensity of the radiation, the ionization state can be used as a crude density diagnostic.

To model Cas A, we make the simplifying assumption that radiation field has a thermal bremsstrahlung spectrum with emissivity normalized to  $L_X = 10^{37} \text{ erg s}^{-1}$  (Favata et al. 1997). For these abundances, the ejecta is depleted of all nuclei lighter than oxygen, and we assume that O, Ne, Mg, Si, S, Ar, Ca, and Fe are present in their solar ratio (Table 3.1). Given these parameters and  $n_{ion} = 0.1$  as above,  $T_e \sim 6000 \text{ K}$  at the remnant center, rising toward the reverse shock. This is clearly hotter than the *Spitzer* spectra imply. Perhaps more instructive, however, are the equilibrium ionization states. Nearly 90% of the oxygen is in states He-like or higher, with  $f(\text{O}^{3+}) \sim 6 \times 10^{-4}$  and a correspondingly miniscule [OIV] emissivity. Clearly the relatively low ionization state lines observed by S09 can not be coming from ejecta of mean density. We are led to the conclusion that the gas detected with *Spitzer* is in clumps of higher densities, analagous to the high density ejecta which forms radiative shocks upon encountering the SNR reverse shock, giving the optical emission we see in Cas A. Indeed, raising the ion density to  $n_{ion} \sim 10 \text{ cm}^{-3}$  pushes the equilibrium temperature and ionization to values more consistent with the observed spectra. However, the calculated pressure varies widely with  $n_{ion}$ , though one expects these dense clumps to be at least close to pressure equilibrium with the surrounding medium. An estimate of the average pressure is thus necessary, and is discussed in the next section. We will return to the higher density clumps in greater detail in Section 4.

This basic physical model requires that the rates in Equations 3 and 4 be fast enough to maintain photoionization equilibrium as the SNR evolves. As the remnant expands, the density in the freely-expanding ejecta declines as  $t^{-3}$ . The cool-

ing and recombination rates drop even faster because of their dependence on  $n_e$ . The decline is actually slower than  $\rho^2$  since the higher ionization preferred at lower densities creates more free electrons, but these  $n_{ion} n_e$  rates eventually “freeze-out” and the gas will depart from equilibrium. We explore this process in the next section.

### 3.3 The Mean Density Ejecta

#### 3.3.1 One-dimensional Hydrodynamics, Radiative Transfer, and Non-equilibrium Ionization

To test the validity of our assumption of photoionization equilibrium and make quantitative estimates of the pressure and temperature of the interior ejecta, we calculated the time dependent thermodynamic and ionization states for the unshocked ejecta using a new hydrodynamics and photoionization code. A detailed description of the code, including the algorithms, initial conditions, and the assumptions contained therein can be found in the Appendix, though we provide a short summary here.

We use a standard finite difference, one-dimensional spherically symmetric Lagrangean hydrodynamics algorithm (Richtmyer & Morton 1967) to evolve the fluid variables. Following Truelove & McKee (1999), we initialize the cold ejecta with a constant density core and power law envelope distribution ( $n = 9$ , Laming & Hwang 2003), and free-expansion velocities. The ejecta encounter a  $\rho(r) \propto r^{-2}$  stellar wind medium, with the density normalized so that the total mass swept-up at  $t_{SNR} = 330$  years is  $8M_{\odot}$  (Willingale et al. 2003). The explosion energy is  $3 \times 10^{51}$  erg, with a total ejecta mass of  $4M_{\odot}$  (Young et al. 2006). Cooling due to line radiation, dust, or cosmic ray acceleration is neglected. This set of parameters yielded  $r_{BW} = 8 \times 10^{18}$  cm and  $r_{RS} = 5.5 \times 10^{18}$  cm, in reasonable agreement with

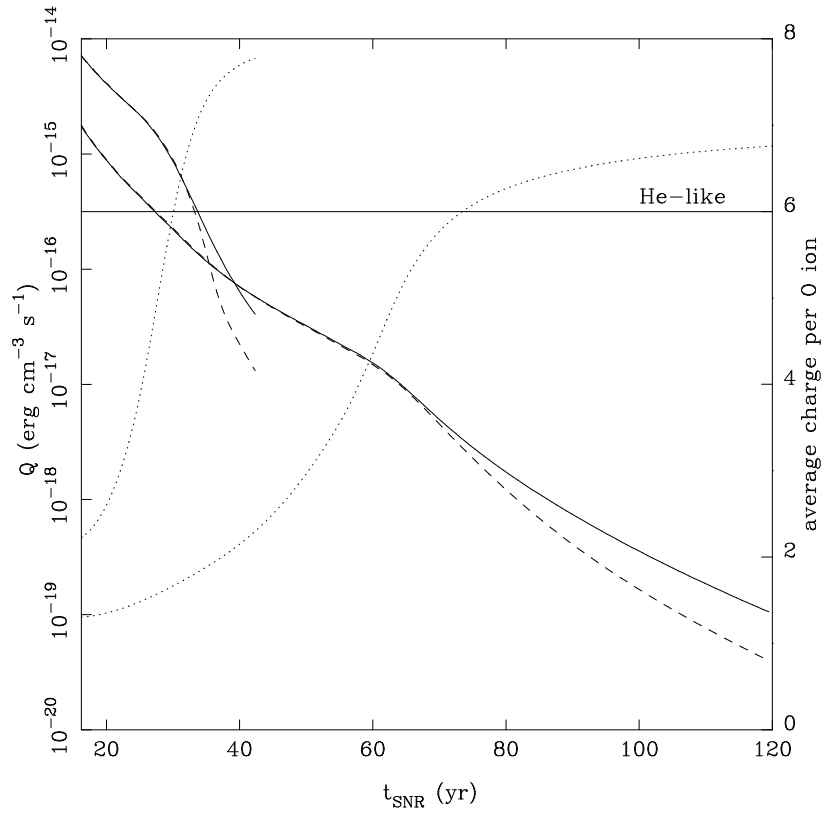


Figure 3.1 The heating and line cooling rates for two zones in our simulation. The heating rate is the solid line, the cooling rate is dashed. The lower curve is for the center zone, while the upper curve encounters the reverse shock at  $t_{\text{SNR}} \sim 42$  yr. The rates track very closely, until the oxygen becomes predominantly ionized to He-like and above, causing a dramatic drop in the cooling efficiency. The dotted line shows the average charge per oxygen ion (at  $X_i = 0.79$  oxygen is the primary coolant). The line cooling rate fails to track the heating rate as the oxygen ionizes to He-like and beyond.

observation.

While the ejecta at the present day are optically thin to the ionizing radiation of the SNR shocks, at early times they were not. In order to calculate the

time-dependent photoionization rate in the interior, every 100 hydrodynamic timesteps we mapped the hydrodynamic variables onto a radial grid, and calculated the radiative transfer with a simplified version of spherically symmetric algorithm described by Hummer & Rybicki (1972). The source radiation was assumed to have a two-temperature bremsstrahlung spectrum, with the normalizations and temperatures determined from the hydrodynamics. Absent a detailed prescription for mixing amongst the different nucleosynthetic layers of the progenitor star in the SN, we assumed fully mixed ejecta, with the depleted solar abundance ratios in Table 3.1.

Every 10 hydrodynamic timesteps we updated the time dependent ionization state of the interior ejecta, using the photoionization rate calculated from the radiative transfer, and collisional ionization and recombination rates determined from the electron density and temperature. The balance of photoionization heating, line cooling and adiabatic expansion determined the thermodynamic state of the interior ejecta, without significantly effecting the hydrodynamics, which are dominated by the momentum of the freely-expanding ejecta.

### 3.3.2 Fluid Evolution

At  $t_{SNR} \sim 15$  yr, when the full calculation begins, approximately  $3.1M_{\odot}$  of material is still interior to the reverse shock, which is located at  $r \sim 4.8 \times 10^{17}$  cm and is propagating into the power-law envelope of the ejecta. In the flat density core,  $n_{ion} = 435 \text{ cm}^{-3}$ , and  $O^+$  is the dominant ion, with  $f(O^+) = 0.76$  in the center zone ( $f$  is the fractional ionic abundance, and sums to 1 for each element). The gas is optically thick from the  $O^+$  edge at 35.1 eV to the oxygen  $K$ -edge at 544 eV, and well past 1 keV, with  $\tau_{35.1 \text{ eV}} > 600$  measured from the edge of the reverse shock to the center of the supernova remnant. Neon is roughly equal parts  $Ne^+$  and  $Ne^{2+}$ , while  $Si^{4+}$ ,  $S^{2+}$ ,  $S^{3+}$ ,  $Fe^{5+}$ , and  $Fe^{6+}$  are the most abundant species of

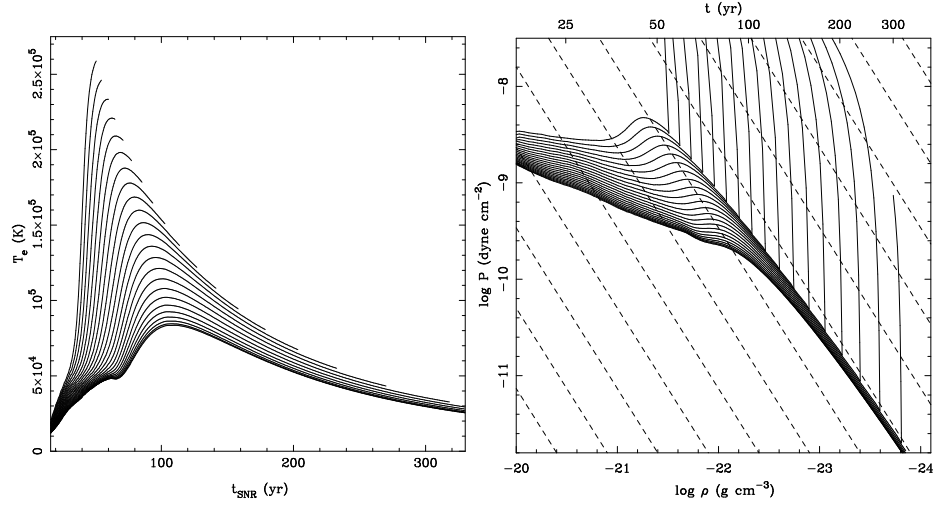


Figure 3.2 The pressure and temperature evolution for ejecta in our models. Each solid line represents an individual Lagrangean fluid element. The dashed lines in the pressure plot represent adiabatic expansion for a  $\gamma = 5/3$  equation of state. The shallower slope indicates that PI heating and line cooling have some effect through the whole simulation. The jump in pressure occurs at the reverse shock. The code does not follow the electron temperature after reverse shock passage, so the temperature tracks end when the fluid element reaches the reverse shock.

the heavier elements. The electron and ion temperatures in the central zone are approximately equal at  $T \sim 1 \times 10^4$  K, rising to  $T \sim 5 \times 10^5$  K in the outer envelope, where lower optical depth and limb-brightening result in a more intense radiation field, and the lower density shifts the balance between PI heating and line cooling.

The implicit assumption in the initial conditions of quasi-equilibrium in the temperatures and ionization states is that that the densities at early times are high enough that the photoionization, recombination, heating, and cooling rates are fast enough to balance. Figure 3.1 shows the heating and line cooling rates as

a function of time for two fluid elements, and confirms the validity of our initial conditions — heating and cooling track closely for a significant time after the start of the simulation. As stated in Section 2, the photoionization and heating rates are proportional to  $n_{ion}$ , and the cooling and recombination rates  $n_{ion} n_e$  (essentially a  $n^2$  dependence). Since the density drops as  $\rho \propto t^{-3}$  in free expansion, so the heating rates falls with time as well. At constant temperature, the line cooling drops faster due its  $n^2$  density dependence, and the temperature rises. However, for the composition and temperature range considered,  $\frac{d\Lambda}{dT_e} > 0$ , so as the temperatures rise, so does the cooling rate, and the quasi-equilibrium is maintained.

As the density drops further, photoionization dominates recombination, and the ionization shifts to higher states. Once the oxygen becomes predominantly He-like, H-like, and stripped, line cooling is no longer efficient and the temperature rises more rapidly (Figure 3.2). Eventually the PI heating rate falls enough that the expansion becomes the dominant thermal effect, and after  $t_{SNR} \sim 100$  yr, the interior gas temperature drops.

Since oxygen is the most abundant element for the chosen composition, its ionization state is the driving factor in the line cooling and PI heating rate. However, it is apparent in Figure 3.2 that the ejecta never reach purely adiabatic expansion ( $\gamma = 5/3$ ). This is because the heavier elements retain electrons in the average density ejecta throughout the simulation. At  $t_{SNR} = 330$ ,  $\text{Si}^{9+}$ - $\text{Si}^{12+}$ ,  $\text{S}^{9+}$ - $\text{S}^{12+}$ ,  $\text{Ar}^{10+}$ - $\text{Ar}^{12+}$ , and  $\text{Fe}^{13+}$ ,  $\text{Fe}^{15+}$  -  $\text{Fe}^{17+}$  all have  $f > 0.1$  in the central zone. Heating due to PI thus continues to the present age of the SNR. While the electron temperatures at these late times are too low for most of these ions to cool efficiently, some line emission through fine structure transitions does occur, chiefly [Fe XIV] 5303Å and [Si X] 1.43μm. As a result, at late times  $P \propto \rho^{-\gamma}$ ,  $\gamma < 5/3$  (Figure 3.2).

### 3.3.3 The Interior Pressure

From these calculations we can place constraints on the pressure in the knots detected with *Spitzer*. These knots must be in approximate pressure equilibrium with the average density medium in which they reside. Since there are no observations which directly infer the average density interior to Cas A's reverse shock, the density in our simulations is not particularly well constrained. Different choices for the explosion energy, the transition velocity from the power law envelope to the constant density ejecta, and the total ejecta mass may produce slightly different present day interior masses but similar shock positions. Moreover, our ionizing radiation spectrum is approximate, so variations in its detailed shape might produce a slightly different temperature evolution. However, given the tight relation in  $P$  and  $\rho$  seen in Figure 3.2, it is possible to estimate how these effects might alter the thermodynamic and ionization state of the interior ejecta. Because of limb-brightening, the radiation field is more intense towards the shell than in the center. Shells at higher radius thus feel more PI heating, and have correspondingly higher pressure. Similarly, since  $\rho$  is time-dependent, output from earlier timesteps can approximate higher interior ejecta masses. In our simulation, at  $t_{SNR} = 330 \text{ yr}$ , the pressure in the central zone is  $1.4 \times 10^{-12} \text{ dyne cm}^{-2}$ , and is about 20% higher just inside the reverse shock.

Table 3.2. One Zone Model Line Fluxes, Depleted Solar Abundances<sup>a</sup>

Ion	$\lambda$ ( $\mu\text{m}$ )	S5	S10	S25	S50	S100	S200
[Ar II]	6.99	1.86(-5)	5.44(-5)	1.77(-4)	4.70(-4)	1.47(-3)	4.88(-3)
[Ar V]	7.91	1.07(-4)	2.70(-5)	6.70(-6)	3.98(-6)	3.79(-6)	4.81(-6)
[Ar III]	8.99	3.15(-4)	5.91(-4)	1.08(-3)	1.77(-3)	3.24(-3)	6.17(-3)
[Fe VII]	9.51	3.09(-3)	1.01(-3)	3.09(-4)	1.66(-4)	1.13(-4)	9.60(-5)
[S IV]	10.51	2.00(-2)	2.57(-2)	3.54(-2)	4.93(-2)	7.62(-2)	1.24(-1)
[Ne II]	12.81	3.58(-4)	1.00(-3)	4.47(-3)	1.53(-2)	5.52(-2)	1.90(-1)
[Ar V]	13.07	7.94(-3)	5.99(-3)	4.19(-3)	3.65(-3)	3.66(-3)	4.07(-3)
[Ne V]	14.33	1.58(-2)	5.41(-3)	2.02(-3)	1.25(-3)	8.96(-4)	6.71(-4)
[Fe VI]	14.77	2.14(-3)	1.12(-3)	5.96(-4)	4.63(-4)	4.33(-4)	4.47(-4)
[Ne III]	15.55	1.13(-2)	1.75(-2)	3.81(-2)	7.64(-2)	1.58(-1)	3.14(-1)
[S III]	18.71	1.91(-3)	5.32(-3)	1.73(-2)	4.09(-2)	9.80(-2)	2.28(-1)
[Fe VI]	19.56	2.20(-2)	2.09(-2)	1.93(-2)	1.85(-2)	1.80(-2)	1.75(-2)
[Fe V]	20.85	7.16(-4)	6.81(-4)	6.87(-4)	8.07(-4)	1.09(-3)	1.51(-3)
[Fe III]	22.94	2.09(-4)	1.56(-3)	1.45(-2)	6.18(-2)	2.19(-1)	6.30(-1)
[Fe I]	24.04	7.40(-10)	1.90(-8)	8.19(-7)	1.06(-5)	1.16(-4)	9.88(-4)
[Ne V]	24.21	8.05(-2)	4.78(-2)	3.04(-2)	2.26(-2)	1.63(-2)	1.09(-2)
[O IV]	25.91	1.00(+0)	1.00(+0)	1.00(+0)	1.00(+0)	1.00(+0)	1.00(+0)
[Fe V]	25.92	3.61(-3)	4.94(-3)	7.14(-3)	9.66(-3)	1.33(-2)	1.79(-2)
[Fe II]	25.98	1.33(-5)	2.14(-4)	4.85(-3)	3.75(-2)	2.31(-1)	1.11(+0)
[Fe III]	33.05	1.88(-5)	1.07(-4)	7.70(-4)	2.97(-3)	1.03(-2)	3.05(-2)
[S III]	33.50	1.81(-2)	7.48(-2)	3.32(-1)	8.06(-1)	1.65(+0)	2.87(+0)
[Fe I]	34.71	2.51(-10)	5.83(-9)	2.25(-7)	2.80(-6)	3.01(-5)	2.60(-4)
[Si II]	34.82	7.35(-3)	5.01(-2)	3.53(-1)	1.14(+0)	3.03(+0)	6.67(+0)
[Fe II]	35.34	1.30(-6)	1.63(-5)	2.93(-4)	2.08(-3)	1.28(-2)	6.47(-2)
[Ne III]	35.97	4.86(-4)	6.03(-4)	1.06(-3)	1.95(-3)	3.96(-3)	7.92(-3)
[Fe V]	36.34	1.13(-2)	2.14(-2)	4.26(-2)	6.57(-2)	9.33(-2)	1.21(-1)
[Fe II]	51.33	2.02(-7)	2.17(-6)	3.29(-5)	2.17(-4)	1.29(-3)	6.34(-3)
[Fe III]	51.71	2.77(-6)	1.37(-5)	8.56(-5)	3.10(-4)	1.06(-3)	3.09(-3)
[O III]	51.81	1.80(-1)	4.17(-1)	1.12(+0)	2.15(+0)	3.79(+0)	5.97(+0)
[Fe I]	54.31	8.10(-13)	1.28(-11)	3.43(-10)	3.75(-9)	4.00(-8)	3.70(-7)
[O I]	63.20	7.32(-7)	6.28(-6)	8.02(-5)	4.68(-4)	2.52(-3)	1.25(-2)
[Fe V]	70.37	2.41(-2)	5.59(-2)	1.25(-1)	1.81(-1)	2.13(-1)	2.05(-1)

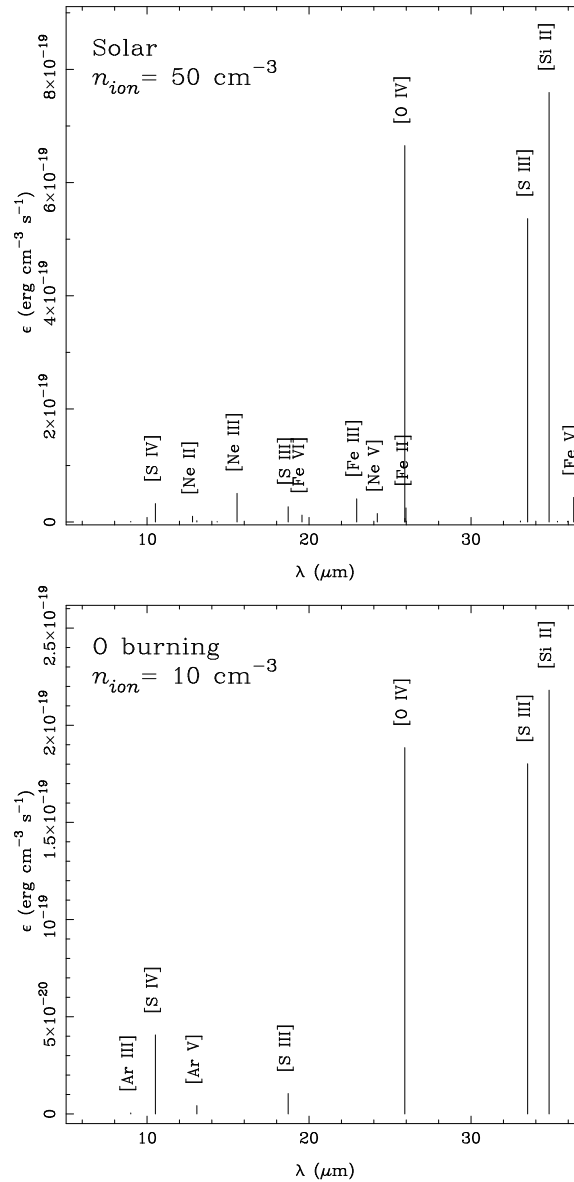


Figure 3.3 Sample calculated one zone spectra for the representative abundances. The approximate observed [S IV] : [O IV] : [Si II] ratios are best reproduced for ion densities several times higher in the solar abundance gas relative to gas containing incomplete O burning products. The non-negligible fraction of Ne and Fe in the solar abundance gas produces numerous emission lines from these elements that are apparently not observed.

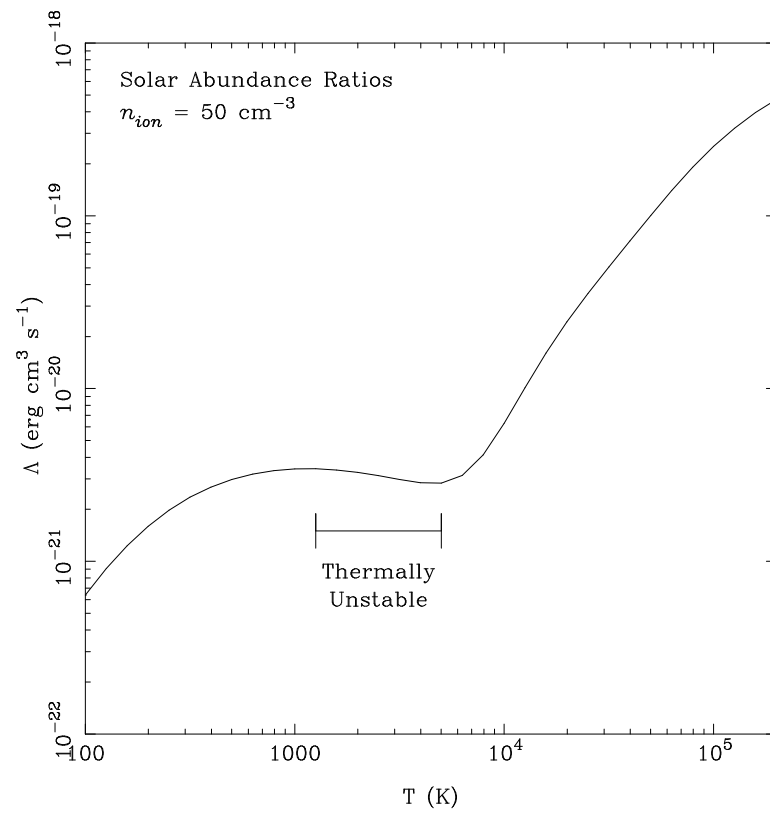


Figure 3.4 The cooling function for the solar abundance ratio and ionization fractions for the S50 ( $n_{ion} = 50 \text{ cm}^{-3}$ ) model.

Table 3.2—Continued

Ion	$\lambda$ ( $\mu\text{m}$ )	S5	S10	S25	S50	S100	S200
[O III]	88.35	4.08(-1)	9.40(-1)	2.19(+0)	3.40(+0)	4.47(+0)	5.05(+0)
[O I]	145.50	8.25(-8)	6.80(-7)	8.36(-6)	4.80(-5)	2.57(-4)	1.27(-3)
$n_{ion}$		5	10	25	50	100	200
$n_e$		14	23	46	78	134	235
$T_e$		456	356	296	277	274	278
$P^b$		1.16(-12)	1.62(-12)	2.89(-12)	4.90(-12)	8.87(-12)	1.67(-11)
$\epsilon([\text{OIV}])^c$	25.91	1.87(-19)	3.13(-19)	4.97(-19)	6.65(-19)	8.88(-19)	1.20(-18)

<sup>a</sup>X.XX(Y) = X.XX  $\times 10^Y$

<sup>b</sup>dyne  $\text{cm}^{-2}$

<sup>c</sup>erg  $\text{cm}^{-3} \text{s}^{-1}$

Table 3.3. One Zone Model Line Fluxes, Incomplete Oxygen Burning<sup>a</sup>

Ion	$\lambda$ ( $\mu\text{m}$ )	O5	O10	O25	O50	O100	O200
[Ar II]	6.99	1.44(-4)	2.49(-4)	1.45(-4)	1.09(-4)	1.04(-4)	2.23(-4)
[Ar V]	7.91	1.16(-3)	5.96(-5)	6.69(-7)	5.02(-8)	9.97(-9)	4.36(-9)
[Ar III]	8.99	2.06(-3)	2.57(-3)	1.34(-3)	8.81(-4)	7.17(-4)	9.32(-4)
[Fe VII]	9.51	...	...	...	...	...	...
[S IV]	10.51	2.64(-1)	2.16(-1)	1.12(-1)	7.86(-2)	6.61(-2)	8.17(-2)
[Ne II]	12.81	7.02(-7)	1.74(-6)	4.57(-6)	1.07(-5)	2.26(-5)	8.03(-5)
[Ar V]	13.07	4.37(-2)	2.25(-2)	7.48(-3)	4.01(-3)	2.79(-3)	2.46(-3)
[Ne V]	14.33	3.07(-5)	5.49(-6)	7.62(-7)	2.41(-7)	1.07(-7)	4.72(-8)
[Fe VI]	14.77	...	...	...	...	...	...
[Ne III]	15.55	2.06(-5)	2.68(-5)	4.04(-5)	6.36(-5)	9.48(-5)	1.83(-4)
[S III]	18.71	2.38(-2)	5.56(-2)	9.32(-2)	1.32(-1)	1.89(-1)	3.80(-1)
[Fe VII]	19.56	...	...	...	...	...	...
[Fe V]	20.85	...	...	...	...	...	...
[Fe III]	22.94	...	...	...	...	...	...
[Fe I]	24.04	...	...	...	...	...	...
[Ne V]	24.21	1.12(-4)	6.38(-5)	5.44(-5)	4.96(-5)	4.25(-5)	2.65(-5)
[O IV]	25.91	1.00(+0)	1.00(+0)	1.00(+0)	1.00(+0)	1.00(+0)	1.00(+0)
[Fe V]	25.92	...	...	...	...	...	...
[Fe II]	25.98	...	...	...	...	...	...
[Fe III]	33.05	...	...	...	...	...	...
[S III]	33.50	1.71(-1)	9.56(-1)	5.73(+0)	1.60(+1)	3.12(+1)	6.69(+1)
[Fe I]	34.71	...	...	...	...	...	...
[Si II]	34.82	1.01(-1)	1.16(+0)	1.20(+1)	4.65(+1)	1.14(+2)	3.49(+2)
[Fe II]	35.34	...	...	...	...	...	...
[Ne III]	35.97	1.02(-6)	8.31(-7)	6.14(-7)	6.28(-7)	7.04(-7)	1.14(-6)
[Fe V]	36.34	...	...	...	...	...	...
[Fe II]	51.33	...	...	...	...	...	...
[Fe III]	51.71	...	...	...	...	...	...
[O III]	51.81	1.71(-1)	5.26(-1)	1.86(+0)	4.15(+0)	7.51(+0)	1.43(+1)
[Fe I]	54.31	...	...	...	...	...	...
[O I]	63.20	7.38(-7)	1.10(-5)	2.43(-4)	1.86(-3)	9.09(-3)	7.39(-2)
[Fe V]	70.37	...	...	...	...	...	...

Table 3.3—Continued

Ion	$\lambda$ ( $\mu\text{m}$ )	O5	O10	O25	O50	O100	O200
[OIII]	88.35	3.53(-1)	1.22(+0)	5.00(+0)	1.12(+1)	1.77(+1)	2.81(+1)
[OI]	145.50	8.49(-8)	1.17(-6)	2.27(-5)	1.61(-4)	7.46(-4)	5.87(-3)
$n_{ion}$		5	10	25	50	100	200
$n_e$		16	25	46	75	128	209
$T_e$		549	323	201	165	148	139
$P^b$		1.57(-12)	1.57(-12)	1.98(-12)	2.84(-12)	4.65(-12)	7.86(-12)
$\epsilon([\text{OIV}])^c$	25.91	1.79(-19)	1.89(-19)	1.20(-19)	8.84(-20)	9.23(-20)	7.00(-20)

<sup>a</sup>X.XX(Y) = X.XX  $\times 10^Y$

<sup>b</sup>dyne  $\text{cm}^{-2}$

<sup>c</sup>erg  $\text{cm}^{-3} \text{s}^{-1}$

### 3.4 One Zone Models of the Dense Ejecta

#### 3.4.1 Model Calculations

As we hypothesized in Section 2 and showed in Section 3, the average density unshocked ejecta in Cas A is too tenuous, and thus too hot and overly ionized to emit the spectra observed with *Spitzer* IRS by S09. Instead, the generally low ionization state of the observed lines indicates overdense gas, analogous to the high density material which produces optically-emitting radiative cloud shocks when encountering the reverse shock.

For the calculations in this section, we used nearly the same procedure as outlined in Section 2 and Equations 3-5. Each model consists of a single optically thin fluid zone, with the radiation mean intensity from the 1D hydro calculations presented in the previous section, though in practice this slight change in the input spectrum has negligible effect on the equilibrium parameters and calculated line

emissivities. Given the single zone and small number of iterations necessary for convergence, for additional accuracy in the cooling calculation we directly solve the population matrix for the relevant ions rather than interpolating on precalculated tables as is done for the 1D simulations. Except where noted, all models in this section are for the exact center of the SNR at  $t_{SNR} = 330$  yr. Given the optically thin conditions in the average density medium, changing the radial position of our calculated zone changes only the normalization of the radiation; this is equivalent to the inverse change in density. The single zone (i.e. optically thin) assumption is valid for a spatial extent of approximately  $r \sim 10^{18} n_{ion}^{-1}$  cm (taking the characteristic photoionization cross section to be 1 Mb, as in Section 2.2). This translates to  $\theta \sim 60'' n_{ion}^{-1}$  at Cas A. This is well below *Spitzer's* diffraction limit for plausible ion densities, though it is approximately equal to the scale of optically emitting knots in the reverse shock resolved with *HST* (e.g. Morse et al. 2004). While there is a strong dust continuum in the observed mid-IR spectra, the thermal coupling between dust and gas is weak, and we neglect any solid state physics.

Table 2 lists the calculated equilibrium electron temperature, density and line emissivities, relative to  $\epsilon([\text{OIV}] 25.91 \mu\text{m}) = 1.0$ , for a grid of one zone models with the solar abundance ratios listed in Table 3.1. As explained in Section 2, as the density increases lines from lower ionization species become stronger relative to [OIV], and  $T_e$  decreases. It is interesting to note the diversity of ionization states present in the calculated spectra, with strong lines present from singly to four times ionized species. This is not typical of UV-photoionized gas such as is found in H II regions, whose spectra are generally dominated by a narrow range of ionization states. The soft X-rays in our models induce inner-shell photoionizations, which often are followed by multiple Auger ionizations, resulting

in significant populations of moderately ionized species such as  $O^{3+}$ ,  $Ne^{4+}$ , and  $Fe^{4+}$ . This is a well known property of X-ray photoionized plasma (e.g. Kallman & McCray 1982).

Absent published quantitative line strengths with which to compare, we instead show in Figure 3.3 a calculated spectrum in the *Spitzer* IRS band for direct comparison with S09's Figure 1. This model (S50,  $n_{ion} = 50$  cm) provides the best qualitative match to the observed strong line ratios on our rather coarse grid, though it is over-pressured relative to the mean density calculation by a factor of 3.5. Note that [Si II]  $34.82\mu\text{m}$  and [O IV]  $25.91\mu\text{m}$  are the brightest lines, with decreasing strength to shorter wavelengths, characteristic of the low equilibrium temperature for these parameters ( $T_e = 277$  K;  $hc/kT_e \sim 52\mu\text{m}$ ). For these abundances and temperatures, two lines in the *Herschel* band ([O III]  $88.35\mu\text{m}$  and [Fe V]  $70.37\mu\text{m}$ ) are quite strong, while a third ([O I]  $63.20\mu\text{m}$ ) is weak because of its low ionization fraction and vanishingly small collision strength at low  $T_e$  (Berrington 1988). Also of note are a number of lines of neon and iron (in particular [Ne III]  $15.55\mu\text{m}$  and [Fe V]  $35.31\mu\text{m}$ ) that are apparently weak or absent from the IRS spectra (Isensee, private communication).

Given that a number of the strongest observed lines in the interior ejecta in Cas A come primarily from O burning ashes (i.e. Si, S), we conclude that the absence of observed Ne (C-burning) and Fe (Si-burning) lines is an abundance rather than an ionization effect, and indicates stratification in the unshocked ejecta. To address this question further, we ran a second grid of models using an admixture of elements (Table 3.1) meant to approximate incomplete explosive oxygen burning (Arnett 1996). Table 3 lists the calculated line emissivities, and Figure 3.3 again shows our best qualitative match with the observations. The enhanced abundances of silicon and sulfur boost the strength of the [S III]  $33.50\mu\text{m}$

and [Si II] 34.82 $\mu$ m lines, which increases the total cooling efficiency, resulting in lower equilibrium temperatures for a given density. This model is much closer to being in pressure equilibrium with the mean density medium, with an overpressure of  $\sim 15\%$ .

The enhanced [S III]/[Si II] in our model relative to the observed has potential diagnostic value. The primary ashes of the O+O oxygen burning reaction are  $^{28}\text{Si}$  and an  $\alpha$ -particle. These excess  $\alpha$ 's are quickly captured onto  $^{24}\text{Mg}$  (also forming  $^{28}\text{Si}$ ) until magnesium is depleted, after which they are captured onto successively heavier  $\alpha$ -elements, forming nuclei such as  $^{32}\text{S}$  and  $^{36}\text{Ar}$  (Arnett 1996). The Si/S abundance ratio is therefore sensitive to the amount of oxygen depletion. We note that our choice for the amount of progression in the O burning was quite arbitrary, and significant variation in this ratio is possible. A quantitative study must wait for published line strengths, but the sensitivity of this line ratio to abundance (as well as ionization) warrants further investigation.

### 3.4.2 Fluid Behavior

For the models considered in the previous section, the electron temperature is a smooth and slowly varying function of the density. It is worth noting this behavior does not continue to arbitrarily low  $n_{ion}$ . Recall that photoionization heating has an  $n_{ion}$  dependence, while line cooling goes as  $n_{ion} n_e$ , so that heating dominates at lower density. For the temperature range in our grid, an equilibrium exists because  $d\Lambda/dT_e > 0$ . Specifically, line cooling adjusts to the relatively greater PI heating at lower density with higher temperature. This works only until a local maximum is reached in the cooling function, after which an increase in temperature results in less cooling. For the mixture of elements considered here, this maximum occurs near  $T_e \sim 1000$  K, beyond which the fine structure lines fade as  $T^{-1/2}$  while the optical forbidden lines (which arise from transitions between

separate spectroscopic terms) are still exponentially quenched (Equation 3.1). As an example, we show in Figure 3.3.3 the cooling function for the abundances and ion balance in model S50.

The steep (essentially exponential) shape of the cooling curve at low temperatures has a stabilizing effect on the high density gas. We have run exploratory simulations like those described in Section 3 for higher densities that indicate high density blobs like those modeled with our one zone calculations are stable and maintain photoionization equilibrium up to at least the current age of Cas A. The similar shape of the cooling curve for cosmic abundance gas in collisional ionization equilibrium gives rise to the multi-phase structure of the ISM (Spitzer 1978).

For ion densities less than  $\sim 1 - 5 \text{ cm}^{-3}$ , the optical forbidden lines are the primary coolants, and the equilibrium temperatures are of order  $10^4 \text{ K}$ . However, for these  $T_e$  the recombination coefficients are at least an order of magnitude smaller than for the  $\sim 300 \text{ K}$  gas, which, combined with the lower densities, means that the recombination rates are probably not fast enough to maintain photoionization equilibrium as the SNR expands, and dynamic calculations like those discussed in Section 3 are required.

## 3.5 Discussion

### 3.5.1 The [S III] lines

Much of the utility of nebular spectroscopy arises from the numerous emission-line diagnostics which derive directly from the level populations. (The most familiar are the [S II]  $\lambda\lambda 6717, 6731 \text{ \AA}$  density and [O III]  $\lambda\lambda 5007, 4364 \text{ \AA}$  temperature indicators.) In the *Spitzer* mid-IR band, the [S III]  $18\mu\text{m}/33\mu\text{m}$  ratio (hereafter F18/F33) has typically been used as density indicator. For the most common neb-

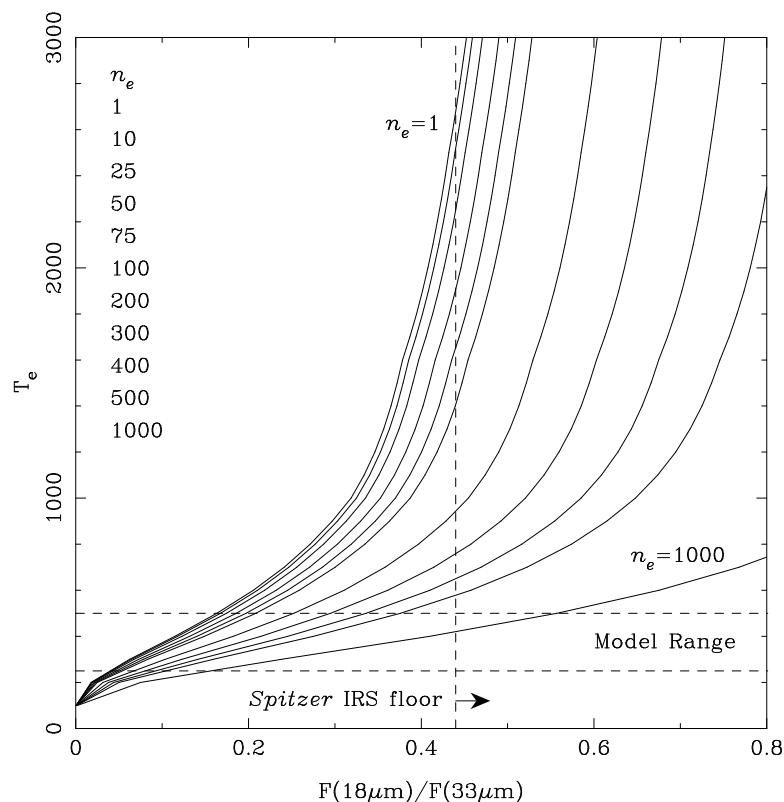


Figure 3.5 The  $F(18\mu\text{m})/F(33\mu\text{m})$  sensitivity to  $T_e$  and  $n_e$ . The horizontal dashed lines bracket the extremes of the model ratios, while the vertical dashed line represents the floor of the observed ratio (Smith, private communication).

ular conditions ( $T_e \sim 10^4$  K), the Boltzman factors of the all levels in the ground term are nearly 1, so the relative strength of the two lines depends only on the radiative lifetimes of the upper level (which depends only on atomic physics) and the collisional de-excitation rates (which depends on the electron density). However, for the low temperatures in our models, the Boltzman factors are much less than 1, and the higher levels are populated much less preferentially than the lower levels. This adds an additional dependence on  $T_e$ , which means this ratio may be used as a temperature diagnostic.

We plot in Figure 3.5 the temperature and density dependence for F18/F33, and indicate the range of values calculated in our models. S09 use F18/F33 to estimate the electron density within Cas A, though they assume its high temperature, low density limit of approximately 0.5 for map pixels with lower ratios. As shown in Figure 3.5, at low temperatures the ratio can drop significantly below this limit as the  $^3P_2$  level, which gives rise to the  $18\mu\text{m}$  line, is populated less than the  $^3P_1$  level, where the  $33\mu\text{m}$  line originates. We also plot the observed floor of F18/F33 in the IRS data (Smith, private communication). It is obvious that the calculated and observed F18/F33 ratios are discrepant. We now examine possible explanations for this.

The obvious first hypothesis is that the gas is actually at either much higher density or temperature than the models suggest. Neither of these is a likely explanation. In order to make the observations and models consistent by changing only the density,  $n_e$  must be very high, perhaps  $\sim 1000\text{ cm}^{-3}$ . This requires a similar ion density, which pushes the ionization equilibrium to very low states and produces a spectrum of mostly [Si II]  $34.82\mu\text{m}$  and little else. This is clearly not what is observed. Conversely, if one accepts the low densities indicated by the models, the observed ratios require  $T_e \sim 2000\text{ K}$ . This does not solve the discrepancy either. Taking the ion balance for O10 (the qualitatively best model for the long wavelength lines), and artificially imposing  $T_e = 2000\text{ K}$ , the short wavelength lines become much stronger. Indeed, this raises the [S IV] emissivity by a factor of 14, making it the strongest line in the IRS band, which is clearly not observed. While it is admittedly unphysical to raise the temperature without changing the ionization, we showed in Section 4.2 that this temperature range is thermally unstable, so there will be no gas in equilibrium at this temperature anyway. One could construct a physical scenario where the gas has recently crested

the maximum in the cooling curve and is on the way to higher temperatures, though it seems unlikely all the observed unshocked ejecta in Cas A would be transitioning through this phase at once, and it is unclear how this would maintain the observed [SIV]/[OIV]. Quantitative measurement of this ratio for multiple positions in the SNR would test this hypothesis directly, though we consider it physically contrived. We thus conclude that there are non-thermal effects not included in the code alter the [SIII] ratio.

One such effect is line emission from recombination cascades, which would populate the  $^3P_2$  level without requiring higher temperatures or densities. To our knowledge there are no level-resolved recombination coefficients for  $S^{3+}$ , required for calculating the recombination spectrum. While such coefficients could be obtained using the Milne relation and photoionization cross sections like those available through the Opacity Project (Seaton 1987), we can rule out recombination with a simpler approach. The [SIII]  $18.71\mu\text{m}$  emissivity from the O10 model is  $1.0 \times 10^{-20} \text{ erg cm}^{-3} \text{ s}^{-1}$ , so the radiative decay rate from the  $^3P_2$  level is  $\epsilon/h\nu = 9.1 \times 10^{-8} \text{ cm}^{-3} \text{ s}^{-1}$ . The recombination rate for  $S^{3+}$  for the physical conditions in our model is  $X_i f_i n_{ion} n_e \alpha(T_e) = 3.1 \times 10^{-10} \text{ cm}^{-3} \text{ s}^{-1}$ , or  $\sim 250\times$  smaller, meaning that even if all recombination cascades pass through the  $J = 2$  level, they would still have no appreciable effect on F18/F33. This estimate includes only the radiative recombination contribution. To our knowledge, no “low-T”  $\Delta n = 0$  dielectronic recombination calculations exist for  $S^{3+}$  (we use the Mazzotta et al. 1998 tabulation for this ion). For  $O^{3+}$ , which also has a  $ns^2p^1$  valence structure, the DR component is  $\sim 1.5\times$  stronger than the RR (Altun et al. 2004). Regardless, recombination cascades apparently have a negligible effect on F18/F33.

Another systematic effect that may alter the [SIII] ratio is the uncertainty in

the atomic data for the  $^3P$  ground term. For our calculations, we use the effective collision strengths (Galavis et al. 1995) and Einstein  $A_{ij}$ 's (Mendoza & Zeippen 1982) from the Iron Project (Hummer et al. 1993) database TIPBASE. Alternatively, we could have used the values in the CHIANTI 5.2 (Dere et al. 1997, Landi et al. 2006) database, which include radiative transition probabilities from Huang (1985) and  $\Gamma$ 's from Tayal & Gupta (1999). The main difference between these two datasets are a nearly factor of 2 disagreement in the  $A_{ij}$  for the  $33\mu\text{m}$  line, and collision strengths that can differ by nearly as much. Unfortunately, the CHIANTI data only worsen the disagreement between the observations and models. While the state of the atomic data for the ground term of S III is thus grim, we can not definitively localize the problem to the atomic data.

A final possibility, which we find most likely, is that the [S III] lines (and perhaps others) are affected by our approximate treatment of photoelectrons from inner-shell ionizations. We discuss this problem in detail in the Appendix, but in summary, inner-shell photoionizations followed by Auger ionization result in the injection of highly suprathermal electrons into the plasma which may thermalize, collisionally ionize additional ions, or collisionally excite bound electrons to energy levels many times  $kT_e$ . Shull & van Steenburg (1985) modeled this effect for cosmic abundance gas, though their results are not directly applicable to the metal-rich composition of our calculations. (They neglect metals.) Detailed treatment of these competing processes requires a Monte Carlo approach that accounts for thousands of bound levels of dozens of ions, and is beyond the scope of the current work. We instead ignore suprathermal ionization and excitation and assume all photoelectrons thermalize instantaneously. The high energy nature of the Auger- and photoelectrons, an interesting test for this scenario may be possible. If they are sufficiently abundant and energetic, emission lines such

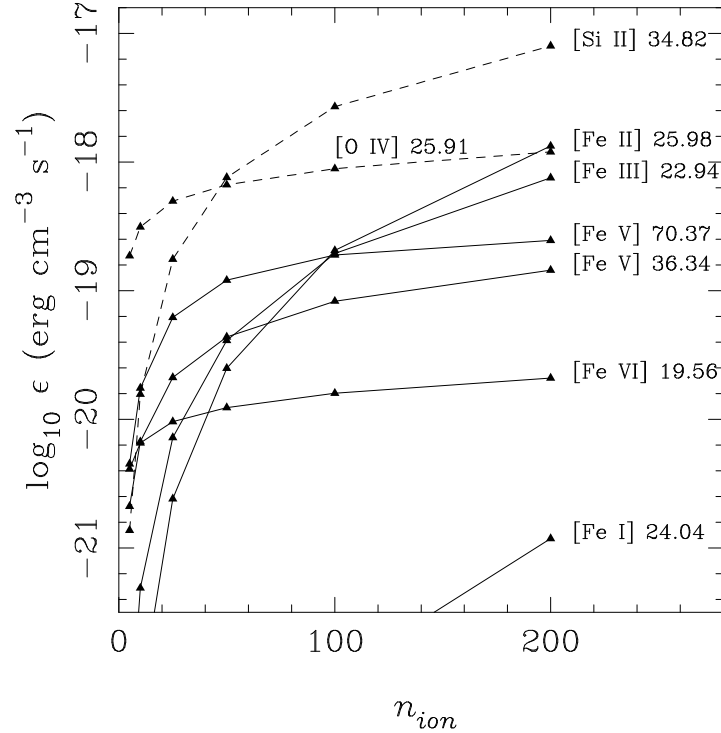


Figure 3.6 Calculated Fe line emissivities for the solar abundance gas. While [Fe II] 25.98  $\mu\text{m}$  is hopelessly blended with [O IV] when it is present at all, [Fe V] 36.34  $\mu\text{m}$  is detectable for all reasonable choices of density, while [Fe III] 22.94  $\mu\text{m}$  emerges at high  $n_{ion}$ .

as [S III]  $\lambda\lambda 9531, 9070\text{\AA}$  or [O III]  $\lambda\lambda 5007, 4959\text{\AA}$  may be produced in low temperature gas in Cas A with luminosities detectable from the ground. This possibility deserves additional theoretical and observational investigation.

### 3.5.2 Where is the Iron?

The vast majority of iron available in the ISM is  $^{56}\text{Fe}$ , which is synthesized in SNe as  $^{56}\text{Ni}$ . The nickel yield of a particular SN is of particular interest since it is sensitive to the detailed radiation hydrodynamic and nucleosynthetic processes operating in the deepest levels of the SN (and thus may constrain the mechanism),

and because radioactive decay of  $^{56}\text{Ni}$  sets the luminosity and drives the light curve of most SNe. The  $^{56}\text{Ni}$  yield in Cas A has been a matter of debate, since spherically symmetric supernova calculations (Timmes et al. 1996) require a large mass of nickel to match the observed  $^{44}\text{Ti}$  yield (Iyudin et al. 1994, Vink et al. 2001, Renaud et al. 2006). However, such an amount of  $^{56}\text{Ni}$  would have produced a very bright SN, though none was seen. This discrepancy has been attributed to asymmetric explosions (Nagataki et al. 2006) and differential fall-back (Young et al. 2006).

Willingale et al. (2003) inventory  $0.058M_{\odot}$  of iron in the X-ray emitting ejecta in the reverse shock, and Eriksen et al. (2009) constrain the  $^{56}\text{Ni}$  yield to be  $< 0.16M_{\odot}$  based on the lack of a widely reported naked eye SN and a new measurement of the interstellar reddening. The X-ray mass is obviously a lower limit, since it excludes iron in radiative shocks, material that has cooled to low temperature after reverse shock passage, or iron that is still in the interior of the SNR.

The mid-IR would seem to be the ideal regime in which to search for any cold, interior iron, since Fe I-III and Fe V-VIII all have fine-structure transitions in the *Spitzer* IRS band. (An accounting of the iron in radiative shocks is probably best accomplished in the optical/NIR where the sensitivity and resolution of ground based telescopes can be utilized, though this is complicated, of course, by the extremely short cooling times in metal-rich plasma.) We plot in Figure 3.6 the emissivities for the brightest iron lines in our depleted solar abundance model. In the *Spitzer* band, [Fe V]  $36.34\mu\text{m}$  is the strongest for low  $n_{ion}$ , though its location at the far red end of the IRS sensitivity may have limited its detectability. [Fe V]  $70.37\mu\text{m}$  is slightly brighter and, if present, should be observable with *Herschel*. [Fe II] is brightest at higher densities, though it is blended with [O IV]. However, [Fe III]  $22.94\mu\text{m}$  is also bright for the same  $n_{ion}$ . Of course, it is unlikely to find a single

plasma with solar abundance ratios, and for one zone calculations that give similar temperatures for Si-burning or  $\alpha$ -rich freeze-out abundances (the processes which produce  $^{56}\text{Ni}$ ), these aforementioned lines, as well as [Fe VI]  $19.56\mu\text{m}$ , are among the brightest features.

However, S09 report no iron lines at all. Hughes et al. (2000) showed that in the *Chandra* observations of Cas A the Fe-rich (Si-burning) material lay outside the Si-rich (O-burning) ashes, which they attributed to a neutrino-driven, convection-induced inversion in the SN. Was this overturn so pronounced that there is now no Fe-rich material interior to Cas A's reverse shock? Perhaps. Alternatively, if the  $^{56}\text{Ni}$  distribution was clumpy, as Li et al. (1993) suggested for SN1987A, the subsequent absorption of the radioactive decay energy (both in  $\gamma$ -rays and positrons) would have inflated these parcels of gas into low density "Ni-bubbles". If the temperatures in these bubbles were beyond the low- $T_e$  maximum in the cooling curve, the Fe-rich, Si-burning ashes would exist in presently Cas A at higher temperatures and lower densities than the low temperature gas detected with *Spitzer*. The exact physical state of this gas is more difficult to calculate, since the low densities invalidate the assumption of photoionization equilibrium in our single zone code, but searches for Fe-rich interior ejecta in Cas A are perhaps best accomplished with surveys for the optical fine-structure transitions of higher ionization states such as [Fe X] or [Fe XIV].

### 3.6 Summary

Simple physical arguments show that the ejecta detected interior to the reverse shock in the mid-IR are cold, and photoionized by the EUV/X-ray photons from the forward and reverse shocks. One-dimensional dynamic photoionization calculations demonstrate that the mean density ejecta is too highly ionized and ten-

uous to emit the observed spectrum, but one zone calculations indicate that photoionization equilibrium is maintained in dense clumps, stabilized by the steep cooling function at low temperatures due to fine structure line cooling. Model spectra for incomplete O-burning abundances are broadly consistent with the observed line ratios, though the systematically low [S III]  $18\mu\text{m}/33\mu\text{m}$  ratio hints that a more sophisticated treatment of suprathreshold photoelectrons is necessary to model the IR spectra precisely. The lack of any observed iron lines over a wide range of ionization states suggests that any Si-burning products still interior to the reverse shock are at lower density (and therefore hotter and more highly ionized) than the *Spitzer* clumps. Finally, two lines ([O III]  $88.35\mu\text{m}$  and [Fe V]  $70.37\mu\text{m}$ ) should be detectable with *Herschel* and could help further constrain the ionization (and therefore density) structure and place more stringent constraints on the iron abundance in Cas A's ejecta.

## CHAPTER 4

MULTI-DIMENSIONAL HYDRODYNAMICS AND NON-EQUILIBRIUM  
IONIZATION IN METAL-RICH PLASMA

## 4.1 The Physics of Supernova Remnant Shocks

In the strictest sense, a shock wave is a purely hydrodynamic phenomenon — a discontinuous jump in the pressure, density, and temperature, mediated in a thin layer by viscous forces, that propagates supersonically through the medium. However, since in situ measurement of the fluid variables is rarely possible for extraterrestrial shocks (limited only to the solar system), it is through the observation and calculation of the emission of the post-shock gas that we are able to gain insight into the physical conditions at work. Computational fluid dynamics is a notoriously expensive enterprise, and with the additional numerical machinery necessary to connect ideal hydrodynamics with the often untidy astrophysics, algorithmic compromise is required. The earliest codes used to model supernova remnant radiative shocks (e.g. Cox 1972; Raymond 1979) initialize a single Lagrangian fluid element using the Rankine-Hugoniot jump conditions, and follow its evolution isobarically as it cools, compresses, and recombines. This simplified, plane-parallel approach allows quite successful modeling of the spectra of radiative shocks in evolved SNRs such as the Cygnus Loop (Cox 1972; Raymond et al. 1988) and N49 (Vancura et al. 1992) as well as the Herbig-Haro objects (e.g. Hartigan et al. 1987). Other studies used similar shock models with enhanced metal abundances (e.g. Itoh 1981) to model the emission from young SNRs such as the Magellanic Cloud remnants N132D and E0102 (Blair et al. 2000, hereafter B2000) and Cas A (Morse et al. 2004). However, for both the cosmic and enriched abundance cases, a single shock speed is rarely sufficient to reproduce the

observed spectra. The most often utilized fix for this is to invoke a power law distribution of pre-shock densities, which leads to a range of initial post-shock conditions. While this produces acceptable fits to the data, the origin (or reality) of this pre-shock distribution is unclear. Moreover, especially in the metal-rich cases, the plane parallel assumption is clearly insufficient. *HST* images of Cas A (Morse et al. 2004) show dramatic clumping of the ejecta, and, perhaps more telling, B2000 had to impose a low- $T_e$  cut-off to their models to avoid overproduction of the O I recombination lines in the cold, photoionized downstream gas. The most likely physical explanation for the suppression of these lines is that the highly compressed cold gas (perhaps subject to cooling instability) present much smaller geometric area to photoionizing photons from the hot, upstream gas. Clearly, a step beyond plane-parallel is warranted.

Perhaps due to the complexity and computational expense of expanding the radiative shock wave problem to multi-dimensions, the original single zone models are still the most common tools for studying SNR shock emission. Some work has been done by coupling full 1D hydrodynamic codes with time dependent ionization solvers and radiative transfer methods (e.g. Innes et al. 1987, Gaetz et al. 1988), though the additional expense of these codes is not balanced by their incremental improvement in efficacy over the single zone approach. Pure hydrodynamic calculations of shock-cloud interactions exist in two (e.g. Patnaude & Fesen 2005) and three dimensions (Stone & Norman 1992a), though it is unclear how to connect a simulated monolithic fluid to actual astrophysical observables given the real-world complexities of composition, ionization, and emission.

An ideal calculation of SNR radiative shock waves would include three dimensional hydrodynamics (to handle shock heating and simulate fluid flow), time dependent (i.e. non-equilibrium) ionization and cooling (to calculate the

spectrum and thermal evolution of the gas), and multi-group radiative transfer (for the photoionization of cool downstream and pre-shock gas). While 3D ideal hydro is now feasible on the desktop, the added complexity of multi-species advection and the time dependent ionization inherent in our problem would require weeks of computation time on a Beowulf cluster or supercomputer. There is certainly much to be learned from such calculations, though it is still not feasible to run the large exploratory grids necessary in order for these to be a truly diagnostic tool. Radiative transfer is reasonably simple in one dimension, requiring only one upstream and one downstream ray per energy bin. However, the problem is considerably more complex in two or three dimensions, given the much larger number of angles, and that each cell is coupled to every other cell. Thus, we present here a step along the path towards solution of the full problem. Our new code couples a simple, parallel, multi-D, multi-species hydrodynamics method with a non-equilibrium ionization solver, that allows simulation of radiative shocks in 2D on the desktop. Radiative transfer is absent, though we discuss prospects for adding it to the code, perhaps using Monte Carlo techniques that take advantage of the highly parallel graphics cards now common on high-end desktop machines. In the remainder of this section, we briefly outline the underlying physics in our calculations. The following section describes our algorithms in detail. We then present a few test and sample problems, and end with a discussion of what is still to come.

#### 4.1.1 Hydrodynamics

The Euler equations describe inviscid, compressible fluid flow, and are the standard prescription of astrophysical hydrodynamics. The three differential equations are statements of the conservations of mass, momentum, and energy for a continuous system, and are closed by an equation of state. The Euler equations

are usually formulated for a single fluid, with a single internal (or total) energy. However, the ion and electron temperatures are often out of equilibrium in SNR shocks, so we include separate internal energies for electrons and ions. (In reality, each element could have its own temperature, though we assume a single ion internal energy for simplicity.) Equations 4.1 - 4.4 are the resulting fluid equations.

$$\frac{\partial \rho}{\partial t} + (\nabla \cdot \mathbf{v})\rho = 0 \quad (4.1)$$

$$\frac{\partial \mathbf{v}}{\partial t} + (\nabla \cdot \mathbf{v})\mathbf{v} = -\nabla P/\rho \quad (4.2)$$

$$\frac{\partial e_e}{\partial t} + (\nabla \cdot \mathbf{v})e_e = -P(\nabla \cdot \mathbf{v}) + \frac{dq_e}{dt} \quad (4.3)$$

$$\frac{\partial e_i}{\partial t} + (\nabla \cdot \mathbf{v})e_i = -P(\nabla \cdot \mathbf{v}) + \frac{dq_i}{dt} \quad (4.4)$$

Note that the energies considered here ( $e_i$  and  $e_e$ ) are internal energy densities, not the total energy density ( $u = e_i + e_e + \frac{1}{2}\rho v^2$ ). This simplifies the inclusion of additional cooling physics at the possible expense of local energy conservation, though this effect is quite small. The additional source terms in Equations 4.3 & 4.4:

$$\frac{dq_e}{dt} = -n_e n_{ion} \sum_m^{N(Z)} \sum_l^{Z(m)} Y_m f_l \Lambda_{m,l}(T_e, n_e) - Q^{Coul} \quad (4.5)$$

$$\frac{dq_i}{dt} = Q^{Coul} \quad (4.6)$$

allow for cooling due to line radiation (which only directly effects the electron gas), and couple the ion and electron internal energies through Coulomb interactions. Here,  $Y_m$  is the number fraction per element (and sums to 1 in each zone), and  $f_l$  is the ionization fraction for each element (which sums to 1 for each element in each zone). In practice, these equations are not solved as part of the hydrodynamics, but are included through operator splitting (Section 4.2.2).

In order to account for the time-dependent composition of nebular gas (due to ionization), we evolve an additional continuity equation for each ionization

species:

$$\frac{\partial}{\partial t}(X_m f_l \rho) + (\nabla \cdot \mathbf{v})X_m f_l \rho = 0; \quad (4.7)$$

Here,  $X_m$  is the mass fraction per element (and sums to 1 in each zone).

#### 4.1.2 Non-equilibrium Ionization

The ionization state behind supernova remnant shocks is often far from thermal equilibrium. For the fast, non-radiative shocks in young SNRs that emit primarily in X-rays, the ionization from the pre-shock conditions progresses rapidly in the hot post-shock gas until the ions are He-like, at which point the ionization potential jumps (e.g. the IP for oxygen jumps from 138 eV for  $O^{5+}$  to 739 eV for  $O^{6+}$ ), and the cross section for collisional ionization of tightly bound K-shell electrons is much smaller than for the outer L- and M-shells. For these ions, and for typical SNR  $n_e$ , the ionization timescale is comparable to, or longer than, the age of the remnant.

In the radiative shocks that emit from the ultraviolet to the infrared, several competing processes set the post-shock conditions. The standard Rankine-Hugoniot jump conditions require that the ions and electrons are initially heated in proportion to their mass ratio ( $T_{ion}/T_e \sim m_{ion}/m_e$ ). Coulomb interactions will equilibrate these temperatures eventually, though the rapid equilibration seen in slower non-radiative shocks (Ghavamian et al. 2007), and presumed to extend to the even slower radiative shocks implies that additional plasma processes dominate. As ion-electron equilibration progresses, so do the competing effects of collisional ionization and line cooling, requiring time-dependent evolution of all these processes in a code.

Equation A.1 in the Appendix gives the general form of the ionization rate equations for a particular chemical element. For the calculations described in this Chapter, we neglect photoionization, and the rate equations are much simplified.

$$\frac{1}{n_e} \frac{df_l}{dt} = f_{l-1} q_{l-1}^{CI} - f_l \left[ \alpha_l^R(T) + q_l^{CI}(T) \right] + f_{l+1} \alpha_{l+1}^R(T) \quad (4.8)$$

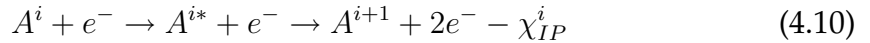
As in Equation 4.7,  $f_l$  is the fractional abundance for each ion,  $q^{CI}$  is the total collisional ionization coefficient, and  $\alpha^R$  is the total recombination coefficient, and includes the radiative and dielectronic contributions. (Because our calculations are for nebular densities, we neglect three body recombination.) A brief description of these processes, and a discussion of our sources for the necessary atomic data follows.

#### 4.1.2.1 Collisional Ionization

Collisional ionization consists of two processes, direct ionization (DI)



and excitation-autoionization (EA)



in which the colliding electron excites (but does not unbind) an inner-shell electron. The resulting ion is unstable to autoionization, and relaxes either by emission of a photon (fluorescence, resulting in no net change in ionization state), or ejection of another electron. DI is dominant for the hydrogen through neon isosequences; EA is most important for ions with more than 10 electrons. We use the collision ionization rate coefficients from Dere (2007), which includes both processes.

#### 4.1.2.2 Radiative Recombination

Radiative recombination (RR) is the capture of an electron into a bound state by emission of a photon.



In many ions with at least one bound electron, this process dominates below  $T_e \sim 1 - 5 \times 10^4$  K, though a number of ions have significant “low-T”  $\Delta n = 0$  dielectronic recombination cross sections even at these temperatures. For the hydrogen through sodium isosequences, we use the RR coefficients from the intermediate coupling calculations of Badnell (2006), and the similar calculations of Altun et al. (2007) for the magnesium isosequence. To our knowledge, no such calculations are available for ions with more than 12 electrons. For these, we use empirical fits from Shull & van Steenburg (1982), and its Erratum.

#### 4.1.2.3 Dielectronic Recombination

Dielectronic recombination (DR) is a multi-step process which is initiated by the excitation of an inner-shell electron, and simultaneous capture of the incident electron into a high- $nl$  orbital. This leaves the ion in a doubly excited state



which decays either by autoionization (resulting in no net change in ionization), or by the radiative decay of the inner-shell electron



The resulting photon is called a “satellite line.” The ion is stabilized against autoionization, and subsequently relaxes by radiative cascade. As with radiative recombination, we use, where available, intermediate coupling calculations the Badnell group (Badnell et al. 2003 provides a summary; each isosequence is presented in a separate paper), which exist for the hydrogen- through magnesium-like ions. For ions with more than 12 electrons, we use the fits from Mazzotta et al. (1998). In the interest of brevity, we list reference for each isosequence in Table 4.1.

Table 4.1. Dielectronic Recombination Coefficient References

Isosequence	Reference
H	Badnell (2006)
He	Bautista & Badnell (2007)
Li	Colgan et al. (2004)
Be	Colgan et al. (2003)
B	Altun et al. (2004)
C	Zatsarinny et al. (2004a)
N	Mitnik et al. (2004)
O	Zatsarinny et al. (2003)
F	Zatsarinny et al. (2006)
Ne	Zatsarinny et al. (2004b)
Na	Altun et al. (2006)
Mg	Altun et al. (2007)
Al-Fe	Mazzotta et al. (1998)

### 4.1.3 Cooling and Heating

Aside from  $PdV$  work, which is calculated in the hydrodynamics, the internal energy of the electron gas can change due to heating by recombination or photoelectrons, and by cooling due to line emission or collisional ionization. In addition, the electron and ion gases exchange energy due to the Coulomb interaction. The details of these processes are discussed in Section A.4 in the Appendix.

### 4.1.4 Photoionization and Radiative Transfer

The structure of a typical radiative shock consists of three regions: a thin ionization zone (where collision ionizations dominate), a cooling zone (where line cooling due to electron collisional excitation dominates), and a photoionization zone (where the gas has cooled enough that EUV photons generated upstream can ionize newly recombining low-ionization species). While the first two regions are adequately modeled with the physics we have described thus far, a proper treatment of the photoionization zone requires a method to transfer the ionizing photons to the cool gas. As discussed above, plane parallel radiative transfer is relatively simple (where only two rays are needed per frequency bin), while other 1D geometries are slightly more complicated (see the Appendix). The problem is considerably more daunting in higher dimensions, where each zone is coupled to every other zone, and a significant number of angle bins are necessary. The general problem of multi-D radiative transfer is still an area of active research, though most in the astrophysical literature pertains to stellar interiors and atmospheres, with dubious applicability to nebular conditions (though, see Ferland 2003). Given the expense and complexity of the calculations undertaken here even without radiative transfer, and its tertiary position in relevance behind hydrodynamics and ionization/cooling for our current problem, our calculations are as yet without a transfer module. We discuss the potential for future addition

of this last piece of physics in Section 4.5.

## 4.2 Algorithms

For simplicity in coding, we implemented the hydrodynamics and time-dependent ionization and cooling as separate modules. The fluid variables are evolved using “operator-splitting.” In a single computational cycle, the hydrodynamics are calculated without the source terms due to line cooling or Coulomb equilibration, followed by an update to the internal energies and ionization fractions from the NEI+cooling. For the following timestep, the order of the NEI+cooling and hydro updates are reversed.

### 4.2.1 Hydrodynamics

Given the complexity of the additional physics required for faithful simulation of radiative shocks, a simple, lightweight hydrodynamics solver is paramount. While high-end codes such as FLASH (Fryxell et al. 2000) are available, the complexity involved in adding additional physics to their large codebase, and the considerable computational power they require, make them less ideal for our problem. Instead, our hydrodynamic algorithm is a new implementation in C (with OpenMP parallelism) based heavily on the venerable finite-difference code ZEUS-2D (Stone & Norman 1992b, hereafter SN92), with considerable modification to simulate fluids with variable composition (due to changes in ionization state and spatially variable abundance), to allow for independent evolution of the ionization and electron internal energies, and to include a parameter to set the initial ratio of electron and ion temperature behind a shock. In addition, while the original ZEUS-2D incorporates a “covariant formalism” to readily accommodate curvilinear geometries, this results in many additional operations per zone per timestep for the slab geometry we are most likely to simulate. We have omitted

this extraneous numerical machinery, though there is nothing in our design that precludes adding this feature for future non-rectilinear calculations.

We follow the two-step approach of SN92, and split each computational cycle into a Lagrangian step, in which the fluid variables are updated for the effects of the source terms (i.e. the right hand side) in Equations 4.1-4.4, and a transport step, which accounts for the flux of the fluid variables due to advection across the grid.

Our code, like ZEUS-2D, uses a staggered mesh, with scalar variables defined at the zone center and the velocity defined at zone faces. In the traditional nomenclature for finite difference equations, each spatial coordinate is designated by a subscript, with face-centered variables labeled with integers, and zone-center variables with half-integers. For readability in the equations below, we shorten this convention. The centering for each variable is implied by its type (i.e. scalar or vector), and half-integer labels are included only for an average or difference across two zones. In addition, while the SN92 code is 2D, we have implemented all our equations in 3D for possible use on faster desktops or shared-memory supercomputers, though the  $z$ -dimension has not yet been thoroughly tested. We have omitted the third dimension in the equations below. The three spatial dimensions are labeled with the indices  $(i, j, k)$ , corresponding to  $(x, y, z)$ . Since arrays in C are contiguous in memory along the last dimension, and in order to make reasonably efficient use of the cache on Intel Core 2 processors for calculations of any dimensionality, array indices for fluid variables in the code are implemented as  $q[k][j][i]$ . To correspond as closely to the code as possible, we have left this seemingly backward order of the indices in the finite difference equations below. The chemical element index is  $m$ ; ionization states within that element are labeled by  $l$ . Finally, we adopt the usual convention to denote time

evolution, with the superscripted indices indicating time-updated values.

#### 4.2.1.1 Source Step

The source step consists of three substeps. In the equations below, the superscript labels the evolution of a variable through each step as  $n, n + a, n + b, n + c$ .

*Part 1:* Update velocities for pressure gradients. There are two possible sets of finite-difference equations for this step, depending on the chosen equation of state. For a gamma-law EOS, where the pressure depends only on the sum of the ion and electron internal energies,

$$vx_{k,j,i}^{n+a} = vx_{k,j,i}^n - (\gamma - 1) \frac{\Delta t}{\Delta x} \frac{eion_{k,j,i+1/2}^n + ee_{k,j,i+1/2}^n - eion_{k,j,i-1/2}^n - ee_{k,j,i-1/2}^n}{(\rho_{k,j,i+1/2}^n + \rho_{k,j,i-1/2}^n)/2} \quad (4.14)$$

$$vy_{k,j,i}^{n+a} = vy_{k,j,i}^n - (\gamma - 1) \frac{\Delta t}{\Delta y} \frac{eion_{k,j+1/2,i}^n + ee_{k,j+1/2,i}^n - eion_{k,j-1/2,i}^n - ee_{k,j-1/2,i}^n}{(\rho_{k,j+1/2,i}^n + \rho_{k,j-1/2,i}^n)/2} \quad (4.15)$$

For more general equations of state, which might include, for instance, a prescription for non-thermal pressure:

$$vx_{k,j,i}^{n+a} = vx_{k,j,i}^n - \frac{\Delta t}{\Delta x} \frac{P_{k,j,i+1/2}^n - P_{k,j,i-1/2}^n}{(\rho_{k,j,i+1/2}^n + \rho_{k,j,i-1/2}^n)/2} \quad (4.16)$$

$$vy_{k,j,i}^{n+a} = vy_{k,j,i}^n - \frac{\Delta t}{\Delta y} \frac{P_{k,j+1/2,i}^n - P_{k,j-1/2,i}^n}{(\rho_{k,j+1/2,i}^n + \rho_{k,j-1/2,i}^n)/2} \quad (4.17)$$

Equations 4.14 & 4.15 execute slightly faster, since the equation of state is embedded in the finite difference equation, eliminating the need for a function call.

*Part 2:* Update velocities and internal energy for artificial viscous heating. The Euler equations have no inherent mechanism for the generation of entropy due to short-range viscous forces in shocks, and simulations without modification generate large, unphysical oscillations behind non-linear waves. Several prescriptions for handling shocks exist (e.g. Godonuv's 1959 method, which includes

the a solution of the shock tube problem at each zone interface, and is the basis of most finite volume methods, such as PPM). The method we use, artificial viscosity, was developed by von Neumann & Richtmyer (1950), who found that an additional heating term  $Q$ , active only for compressions and propotional to the square of the velocity divergence, gives the correct shock jump conditions.

$$Q = \begin{cases} l^2 \rho (\partial v / \partial x)^2 & \text{if } \partial v / \partial x < 0 \\ 0 & \text{otherwise} \end{cases} \quad (4.18)$$

In practice, the artificial viscosity has components for compression in each spatial direction:

$$Qx_{k,j,i}^n = \begin{cases} C_Q \rho_{k,j,i+1/2}^n (vx_{k,j,i+1}^n - vx_{k,j,i}^n)^2 & \text{if } (vx_{k,j,i+1}^n - vx_{k,j,i}^n) < 0 \\ 0 & \text{otherwise} \end{cases} \quad (4.19)$$

$$Qy_{k,j,i}^n = \begin{cases} C_Q \rho_{k,j+1/2,i}^n (vy_{k,j+1,i}^n - vy_{k,j,i}^n)^2 & \text{if } (vy_{k,j+1,i}^n - vy_{k,j,i}^n) < 0 \\ 0 & \text{otherwise} \end{cases} \quad (4.20)$$

For the velocity update, we use a procedure identical to SN92:

$$vx_{k,j,i}^{n+b} = vx_{k,j,i}^{n+a} + \frac{\Delta t}{\Delta x} \frac{(Q_{k,j,i+1/2}^n - Q_{k,j,i-1/2}^n)}{(\rho_{k,j,i+1/2}^n + \rho_{k,j,i-1/2}^n)/2} \quad (4.21)$$

$$vy_{k,j,i}^{n+b} = vy_{k,j,i}^{n+a} + \frac{\Delta t}{\Delta y} \frac{(Q_{k,j+1/2,i}^n - Q_{k,j-1/2,i}^n)}{(\rho_{k,j+1/2,i}^n + \rho_{k,j-1/2,i}^n)/2} \quad (4.22)$$

However, since our code has separate ion and electron internal energies, which receive different amounts of heating at shocks due to the inequality in the electron and nuclear masses, we require a modification of the ZEUS-2D prescription for viscous heating in the energy equations. Recall that while the jump conditions require that ions and electrons be heated in proportion to their masses, it is observed that plasma effects cause some degree of prompt equilibration

(Ghavamian et al. 2007). It can be shown that for a given post-shock electron/ion temperature ratio  $T_{rat} \equiv T_e/T_{ion}$  and a gamma-law EOS, the proportion of artificial viscous heating is

$$Q_{ifrac} = \left( \frac{n_e}{n_{ion}} T_{rat} \right)^{-1} \quad (4.23)$$

$$Q_{efrac} = 1 - Q_{ifrac}. \quad (4.24)$$

Thus, the finite-difference equations for viscous heating are:

$$eion_{k,j,i}^{n+b} = eion_{k,j,i}^{n+a} - \quad (4.25)$$

$$- \frac{\Delta t}{\Delta x} Q_{ifrac} Qx_{k,j,i}^n (vx_{k,j,i+1}^{n+a} - vx_{k,j,i}^{n+a}) \quad (4.26)$$

$$- \frac{\Delta t}{\Delta y} Q_{ifrac} Qy_{k,j,i}^n (vy_{k,j+1,i}^{n+a} - vy_{k,j,i}^{n+a}) \quad (4.27)$$

$$ee_{k,j,i}^{n+b} = ee_{k,j,i}^{n+a} - \quad (4.28)$$

$$- \frac{\Delta t}{\Delta x} Q_{efrac} Qx_{k,j,i}^n (vx_{k,j,i+1}^{n+a} - vx_{k,j,i}^{n+a}) \quad (4.29)$$

$$- \frac{\Delta t}{\Delta y} Q_{efrac} Qy_{k,j,i}^n (vy_{k,j+1,i}^{n+a} - vy_{k,j,i}^{n+a}) \quad (4.30)$$

*Part 3: PdV Work.* As in *Part 1*, there are two possible finite difference equations for  $PdV$  work. For both ions and electrons, and a gamma-law equation of state,

$$e_{k,j,i}^{n+c} = \left[ \frac{1 - 0.5\Delta t(\gamma - 1)(\nabla \cdot \mathbf{v})}{1 + 0.5\Delta t(\gamma - 1)(\nabla \cdot \mathbf{v})} \right] e_{k,j,i}^{n+b} \quad (4.31)$$

where,

$$\nabla \cdot \mathbf{v} = \frac{vx_{k,j,i+1} - vx_{k,j,i}}{\Delta x} + \frac{vy_{k,j+1,i} - vy_{k,j,i}}{\Delta y} \quad (4.32)$$

For a more general EOS, we use a predictor-corrector method, as in ZEUS-2D.

$$e_{k,j,i}^{pred} = (eion_{k,j,i}^{n+b} + ee_{k,j,i}^{n+b}) - P_{k,j,i}^{n+b} (\nabla \cdot \mathbf{v}) \Delta t \quad (4.33)$$

$$eion_{k,j,i}^{n+c} = eion_{k,j,i}^{n+b} - \frac{1}{2} (P_{k,j,i}^{pred} + P_{k,j,i}^{n+b}) (\nabla \cdot \mathbf{v}) \left( \frac{1}{n_e/n_{ion} + 1} \right) \quad (4.34)$$

$$ee_{k,j,i}^{n+c} = ee_{k,j,i}^{n+b} - \frac{1}{2} (P_{k,j,i}^{pred} + P_{k,j,i}^{n+b}) (\nabla \cdot \mathbf{v}) \left( 1 - \frac{1}{n_e/n_{ion} + 1} \right) \quad (4.35)$$

### 4.2.1.2 Transport Step

Advection can be understood as the net the flux of a fluid quantity across the surface of a zone. Rewriting the continuity equation (Equation 4.1) further illustrates this definition.

$$\frac{\partial \rho}{\partial t} = -\nabla \cdot \mathbf{v} \quad (4.36)$$

Applying the divergence theorem and integrating over the zone volume, the finite difference representation of Equation 4.36 is

$$\rho_{i+1/2}^{n+1} = \rho_{i+1/2}^n - \frac{\Delta t}{\Delta x} (F_i - F_{i-1}) \quad (4.37)$$

where  $F_i = \rho_i^* v_i$  is a face-centered flux and  $\rho^*$  is defined below.

On our staggered mesh, proper spatial centering requires a face-centered scalar quantity (density in Equation 4.36). The simplest solution is to choose the density in the “up-wind” zone.

$$\rho_i^* = \begin{cases} \rho_{i-1/2} & \text{if } v_i < 0 \\ \rho_{i+1/2} & \text{if } v_i > 0 \end{cases} \quad (4.38)$$

This is known as “donor-cell” advection.

It must be recalled that our finite difference representation is a (necessary but unfortunate) discretization of a continuous field. This introduces non-physical diffusion into our approximate hydrodynamic equations which manifests itself in the advection step. Essentially, the finite size of the grid cells imposes a low-pass filter on the waveforms in the simulated fluid, and sharp features can not be maintained. This is a fundamental limitation of Eulerian hydrodynamics, and much work has been done on minimizing this numerical diffusion by extracting sub-grid resolution from the fluid by interpolation. The donor-cell method makes no use of these techniques; its diffusion is significant and is an unacceptable algorithm for scientific work. Simple interpolation introduces non-monotonic ar-

tifacts into the fluid variables near discontinuities like shocks, so more sophisticated algorithms are necessary.

van Leer (1977) developed the following second-order accurate, monotonic interpolation scheme:

$$q_i^* = \begin{cases} q_{i-1} + (\Delta x_{i-1} - v_i \Delta t)(dq_{i-1}/2) & \text{if } v_i > 0 \\ q_{i+1} + (\Delta x_i - v_i \Delta t)(dq_i/2) & \text{if } v_i < 0 \end{cases} \quad (4.39)$$

where  $dq$  are monotonized slopes:

$$dq_i = \begin{cases} \frac{2\Delta q_{i-1/2}\Delta q_{i+1/2}}{\Delta q_{i+1/2} + \Delta q_{i-1/2}} & \text{if } \Delta q_{i+1/2} q_{i-1/2} > 0 \\ 0 & \text{otherwise} \end{cases} \quad (4.40)$$

This method reverts to donor cell near shocks, which spread over several zones to minimize Gibbs noise, though it limits diffusion sufficiently in regions of smooth flow, for reasonable fidelity in the representation of the simulated fluid. Many other flux-limiters of varying complexity exist, perhaps most notably the piecewise parabolic method of Colella & Woodward (1984). However, we feel that the van Leer procedure is the best trade-off of speed and simplicity for performance, and use it for our code.

Unlike the source step, the transport or advection step proceeds in a directionally split manner. That is, in one computation cycle all fluid variables are updated for flow across the grid in one direction, followed by an update for flow in the orthogonal direction (or directions, for 3D). In order to optimize local conservation of energy and momentum, which may be affected by machine round-off and numerical diffusion inherent in the interpolation routine, we take the same approach as SN92 and make the flux of these quantities consistent with the mass flux. That is, we advect the specific internal energies ( $e/\rho$ ) and momenta ( $s \equiv \rho v$ ).

The specific momenta are calculated at the start of the transport step

$$sx_{k,j,i}^{n+1/2} = vx_{k,j,i}^{n+1} (\rho_{k,j,i-1/2}^{n+1/2} + \rho_{k,j,i+1/2}^{n+1/2})/2 \quad (4.41)$$

$$sy_{k,j,i}^{n+1/2} = vy_{k,j,i}^{n+1} (\rho_{k,j-1/2,i}^{n+1/2} + \rho_{k,j+1/2,i}^{n+1/2})/2 \quad (4.42)$$

where the half-integral time indices denote the values at the end of the source step. The resulting fluxes for the  $x$ -direction sweep are defined as

$$F_i^{n+1/2} = \rho_i^* vx_i^n \Delta x^N \quad (4.43)$$

$$Frac_{iml}^{n+1/2} = (Y_{mfl}\rho_i)^* vx_i^n \Delta x^N \quad (4.44)$$

$$Ee_i^{n+1/2} = (ee_i/\rho_i)^* vx_i^n \Delta x^N \quad (4.45)$$

$$Eion_i^{n+1/2} = (eion_i/\rho_i)^* vx_i^n \Delta x^N \quad (4.46)$$

$$S_{i+1/2}^{n+1/2} = sx_{i+1/2}^* (vx_{i+1}^n + vx_i^n)/2 \Delta x^N \quad (4.47)$$

$$T_i^{n+1/2} = sy_i^* vx_i^n \Delta x^N \quad (4.48)$$

where  $S_{i+1/2}$  denotes of the flux of (vector)  $x$ -momentum and  $T_i$  the flux of (vector)  $y$ -momentum due to flow in the  $x$ -direction (note the spatial centering). The fluid variables  $\rho$ ,  $ee$ ,  $eion$ , and the  $s$ 's are updated as in Equation 4.37, and the appropriate velocities are used for sweeps in the subsequent spatial directions. The velocities,  $v$ , are not updated until the after final directional sweep to maintain proper time centering. To approximate second-order time centering, the order of the directional sweeps is rotated each timestep.

#### 4.2.1.3 Boundary Conditions

Calculation of the fluid variables at the domain boundaries requires additional information in ghost zones. Since we use van Leer interpolation only one ghost per row or column is required, though in practice we included two ghosts for possible future implementation of higher-order schemes. The ghost zones are

updated after each source substep, the transport step, and the NEI+cooling step. We have included three types of boundary conditions. In the following descriptions, the velocity at the boundary is denoted by the index  $i$ , while the scalar quantity in the ghost zone is denoted by  $i - 1/2$ .

*Reflecting:* This BC is exact.

$$v_i = 0.0 \quad (4.49)$$

$$q_{i-1/2} = q_{i+1/2} \quad (4.50)$$

*Periodic:* For this BC,  $-i$  and  $-i + 1/2$  refer to the value in the last active zone on the opposite side of the domain.

$$v_i = v_{-i} \quad (4.51)$$

$$q_{i-1/2} = q_{-i+1/2} \quad (4.52)$$

*Flow-through:* This BC is exact for supersonic flow, though missing characteristics cause spurious reflections for subsonic flow.

$$v_i = v_{i+1} \quad (4.53)$$

$$q_{i-1/2} = q_{i+1/2} \quad (4.54)$$

## 4.2.2 Time-Dependent Ionization and Cooling

Equations 4.5 & 4.6 demonstrate the effects of cooling by line radiation and the Coulomb interaction on the ion and electron internal densities. The numerical evolution of these quantities involves updates to the ionization state of the gas (which depends on the electron temperature and density) and the internal energy densities (which depend on the temperatures, electron density, and the ionization state). We use a simple midpoint method to integrate explicitly the energy

equations, with the ability to subcycle in zones with short cooling times, and an implicit matrix inversion to advance the ionization state.

The artificial viscosity spreads shocks across several zones, and cells within this diffusive region have unphysical intermediate fluid conditions. If the artificial viscosity is greater than  $10^{-4}$  times the gas pressure, the zone is skipped.

For zones not in shocks, the first step is to calculate the electron temperature, and determine the cooling timescale:

$$\tau_e = \frac{e_e}{n_e n_{ion} \sum_m^{N(Z)} \sum_l^{Z(m)} Y_m f_l \Lambda_{ml}(T_e, n_e) - Q^{Coul}} \quad (4.55)$$

$$\tau_{ion} = e_{ion}/Q^{Coul} \quad (4.56)$$

$$\tau_{cool} = \min(\tau_e, \tau_{ion}) \quad (4.57)$$

The cooling coefficient for each ion,  $\Lambda_{lm}$  is interpolated from a pre-tabulated cooling curve in a similar manner as that described in the Appendix. The cooling timestep is then set to  $t_{cool} = 0.01 \tau_{cool}$ , or to the global timestep, whichever is shorter. The ionization state is then advanced for  $1/2 t_{cool}$ , using the rate equations (Equation 4.8) and the implicit Euler method (Equation A.2). The electron density, cooling coefficients, and Coulomb rate are recalculated, and the internal energy densities are updated for the full  $t_{cool}$  subcycle. This process is repeated until the total time elapsed equals the global timestep, at which point the ionization state is updated again. If the gas pressure decreased by more than 5% during the total timestep, the next global timestep is not allowed to be longer than  $0.05 \tau_{cool}$ .

### 4.2.3 Timestep Control

The timestep in our simulations can be set by three physical effects: the Courant-Friedrichs-Lewy (often shortened to Courant or CFL) condition, the diffusive timescale imposed by the artificial viscosity, or the cooling timescale mentioned

in Section 4.2.2. In addition, we require that the timestep not increase by more than 20% over the previous cycle.

The Courant timescale for hydrodynamics on an Eulerian zone is

$$t_{CFL} = C_{CFL} \min\left(\frac{\Delta x}{c_s + |v_x|}, \frac{\Delta y}{c_s + |v_y|}\right) \quad (4.58)$$

where  $c_s$  is the sound speed and  $C_{CFL}$  is a “safety factor,” typically set to 0.5. This is essentially a statement of the locality of hydrodynamics — each zone only “feels” the effect of its neighbors. The CFL condition imposes a causality constraint, that no information can propagate over more than one zone per timestep.

The artificial viscosity timescale, which may be derived from the stability constraint for a diffusion equation (Bowers & Wilson 1991), is

$$t_Q = \min\left[\frac{\Delta x}{4} \left(\frac{\rho}{Q_x}\right)^{-1/2}, \frac{\Delta y}{4} \left(\frac{\rho}{Q_y}\right)^{-1/2}\right] \quad (4.59)$$

So, the global timestep, including the previous cycle constraint, is

$$\min[t_{CFL}, t_Q, t_{mincool}, 1.2 t_{old}] \quad (4.60)$$

#### 4.2.4 OpenMP Parallelization

Racks of commodity desktop computers linked by ethernet, the so-called Beowulf clusters, are perhaps the form of parallel computing most familiar to modern astrophysicists. The advantages of these systems are self-evident — scalable, low-cost hardware can provide supercomputing power on a department or research group level of funding. Indeed, the Bunyip cluster, constructed at the Australian National University and consisting of 192 Pentium III machines, won the 2000 Gordon Bell prize in the Price/Performance category, and was the first computer which cost less than \$1/MegaFLOP/s. The disadvantages are also readily apparent. Many dozens of machines running at peak performance means frequent equipment point failures, communication between nodes, even across switched

Gigabit ethernet, is slow and inefficient, and the tools required to parallelize a serial code can be inelegant and require substantial programmer effort. While Beowulfs are indeed valuable for large-scale computation, they are less suited for the exploratory or diagnostic grid calculations required for rigorous comparison to observations.

For the last several years most workstations have shipped with one or more “multi-core” CPUs, meaning that parallel computing is now possible on the desktop. These new computers, while currently lacking the sheer number of processors of even a small Beowulf, provide a user-friendly platform for calculations larger than typically possible on previous generations of workstations, but smaller than those requiring supercomputer power. In addition, programming for these multi-core machines is considerably easier than for clusters.

Most simple Unix programs run as a single process, and all computing associated with that process is handled on a single CPU. Parallel code for multi-core machines generally makes use of Unix threads, which allow multiple lines of control within a single process, and have very little operating system overhead in creation and termination (Stevens & Rago 2005). The OS kernel farms these threads to their own cores, allowing parallel execution and a corresponding performance gain. This architecture has an additional advantage over clusters as well. Since all cores share a single main memory space, communication between threads running on separate cores happens over the fast system bus, rather than by interprocess communication over comparatively slow ethernet, as in a Beowulf.

One could in principle program multiple threads at the OS level, which would require proficiency in Unix system programming. However, the OpenMP programming model (e.g. Chandra et al. 2001) greatly simplifies this process, and

facilitates sophisticated parallelism with an API consisting of not much more than a few C preprocessor directives. (A similarly simple OpenMP interface exists for Fortran.) OpenMP has been supported in GCC since v4.3.0, which is the version we used for all calculations in this dissertation.

At its simplest, OpenMP exploits loop-level parallelism, demonstrated with the code fragment below.

```
#include <omp.h>
// Initialize x with some junk.
for ( i = 0; i < arraySize; i++ ){
    x[i] = ( (double) i ) / ( i + 1000 );
}
// Here's the OpenMP pragma that parallelizes the for-loop.
#pragma omp parallel for
for ( i = 0; i < 10000000; i++ ){
    y[i] = sin( exp( cos( - exp( sin(x[i]) ) ) ) );
}
```

The most expensive portion of this program is clearly the loop containing the assignment to `y[i]`, as it calls five transcendental functions per iteration, and is a strong candidate for parallelization. The `#pragma omp parallel for` preprocessor directive tells an OpenMP-enabled compiler to spawn a number of threads specified by the `OMP_NUM_THREADS` environment variable at the `for` loop, and automatically divides the loop index evenly amongst the new threads. (Non-enabled compilers ignore the OpenMP pragmas, and compile serially.) Once the loop is completed, the new threads are destroyed and control returns to the original master thread. On our Apple Macintosh Pro with two dual core Intel Core 2 processors (a total of four cores), the above code runs in 2.19 seconds for one core, and 0.58 seconds on four cores, a speed-up of a factor of 3.7. A full factor of four is not realized in part because of the overhead of the thread creation, and in part

because the rest of the program runs serially.

While this gain in performance is impressive both for its bump in speed and ease of implementation, for a complex program such as a hydro code, which may contain dozens of loops, it is clearly not efficient to create and destroy thread teams at each `for` statement. We thus take an only slightly more complex approach in our code, which we demonstrate with the following code fragment, which comes partly from our initialization routine, and partly from Part 1 of the hydro source step.

```
#include <omp.h>

// this code is in hydroInit.c
threadptr = threadstr;
threadptr = getenv("OMP_NUM_THREADS");
if( strcmp(threadptr,"(null)") ) nthreads = 1;
else                               nthreads = atoi(threadptr);
nthreads = atoi(threadptr);

#if DIM == 1
    omp_set_num_threads(1);
#endif

// this code is in hydroMPsource.c
#pragma omp parallel private(i,j,k,ithread)
{
    ithread = omp_get_thread_num();

    HYDROPREC delP;

    // part 1
    // update velocities for pressure gradients
    //fac = 2.0 * xtfac * EOSgamma1;
```

```

#pragma omp for
    FORCOLS(j, JZoneMIN, JZoneMAX, k, KZoneMIN, KZoneMAX) {
        FORROW(i, IFaceMIN, IFaceMAX) {
            delP = eion[k][j][i+1]+ee[k][j][i+1] -
                (eion[k][j][i]+ee[k][j][i]);
            vx[k][j][i] -= xfac1 * delP/(rho[k][j][i+1] + rho[k][j][i]);
        }
    }

#if DIM > 1
#pragma omp for
    FORCOLS(i, IZoneMIN, IZoneMAX, k, KZoneMIN, KZoneMAX) {
        FORROW(j, JFaceMIN, JFaceMAX) {
            delP = eion[k][j+1][i]+ee[k][j+1][i] -
                (eion[k][j][i]+ee[k][j][i]);
            vy[k][j][i] -= yfac1 * delP/(rho[k][j+1][i] + rho[k][j][i]);
        }
    }
#endif

// full code includes a #if DIM == 3 loop here for 3D calculations

// end part 1

// update BC's
#pragma omp critical
{
    if(ithread == 0) BoundaryConditions();
}

// parts 2 & 3 would follow here

```

```
} // closes threads
```

We have found that one dimensional calculations benefit little from parallelization, since the thread overhead is significant relative to the science computation, and manually set the number of threads to one with the `omp_set_num_threads(1)` function call. Conversely, 3D calculations are still quite burdensome with only four cores. So, we have optimized the code for two dimensions.

In the section of code from `hydroMPsource.c`, the `#pragma omp parallel` directive tells the compiler to create a thread team for the following code block, while the `private(i,j,k,ithread)` clause creates private instances of those variables in each thread. `HYDROPREC` is a preprocessor `#define` (normally set to `double`) and declares `delP` as a lexical variable within the parallel block, so it too has separate copies in each thread. `FORCOLS()` and `FORROWS()` are also preprocessor `#define`'s, and expand to nested `for` loops over the spatial coordinates. Within the parallel block, the `#pragma omp for` directives split the outermost nested loop between the threads. Finally, the `#pragma omp critical` directive halts execution in all threads at that point, allowing synchronization and call to the boundary condition routine in only one of the threads.

The parallel block continues through the rest of `hydroMPsource.c`, meaning only one thread team is created and destroyed for the entire source step. The parallelization of the NEI+cooling module is, with only one spatial loop, is even simpler. While the advection routine is more involved, the general procedure is the same.

The success of any parallelism scheme is ultimately measured in its perfor-

mance. While it is possible in certain special cases on advanced shared memory NUMA supercomputers to achieve super-linear speed-up per processor due to their advanced memory caching (Chandra et al. 2001), the gain on commodity workstations is likely to scale as slightly less than the number of available CPUs. For our code, we see nearly a factor of two going from one to two cores. With four cores (the maximum currently available to us), we see a gain of just greater than  $3.6\times$ , which we consider quite good. It will be interesting to see how this performance scales as greater numbers of cores become available in desktop workstations.

### 4.3 Test Problems

That we resort to numerical simulation of hydrodynamics betrays the fact that there are few exact solutions for any but the simplest of problems. Over the decades a number of well-understood one- and two-dimensional problems have become canonized as standard test problems, used to validate that a new code works as expected, and to evaluate the relative performance of disparate algorithms. We have run the standard problems (e.g. the Sod shock tube, Kelvin-Helmholtz and Rayleigh-Taylor instability growth, the shock bubble) as well as most of the new problems posed by Liska & Wendroff (2003), for a single-fluid version of our code. Since these problems offer little new physics, and because the code performs as expected for a moderately diffusive second-order finite difference code (indeed, the results are, not surprisingly, quite similar to those presented by SN92), we will not discuss them further here.

Conversely, we are aware of very few calculations — multi-species hydrodynamics with nebular cooling and ionization — like our own. This makes verification of our results tricky. We present here two sets of tests of our code, one which

validates the non-equilibrium ionization solver, and another which may be compared with single zone model like Itoh (1981) or B2000, with the caveat that those calculations include radiative transfer and photoionization, while ours do not.

#### 4.3.1 Collisional Ionization Equilibrium

A non-equilibrium ionization solver must both accurately produce the time-dependent ionization state throughout the calculation, and must also converge to the equilibrium populations as  $t \rightarrow \infty$ . In this subsection, we show that our code meets both requirements.

To test that our calculation reproduces the correct equilibrium ionization state, we set the left-hand side of Equation 4.8 to zero ( $\partial f_i / \partial t = 0$ ), and solve for the ionization fractions. In Figures 4.1 & 4.2, we show our calculated collisional ionization equilibrium (CIE) fractions for oxygen and iron, and compare them with the ionization balance from Mazzotta et al. (1998). The agreement is quite good, with the minor departures likely due to our differing ionization and recombination rate coefficients.

As with CIE, there is no analytic solution for non-equilibrium ionization fractions. In Figures 4.3 & 4.4 we compare our NEI fractions for oxygen and iron with those of Hughes & Helfand (1985), a paper often cited for NEI analysis of X-ray spectra from supernova remnants. Again, the agreement is excellent, with minor differences mostly likely resulting from our use of more modern atomic data.

#### 4.3.2 One Dimensional Shocks

To test the integration of our hydrodynamics and plasma codes, we have run a suite of increasingly complex 1D shock models matched as closely as possible to the conditions in Cas A. For simplicity and to minimize run-time, all our models are for shocks in pure oxygen, though the code is capable of evolving an arbitrary

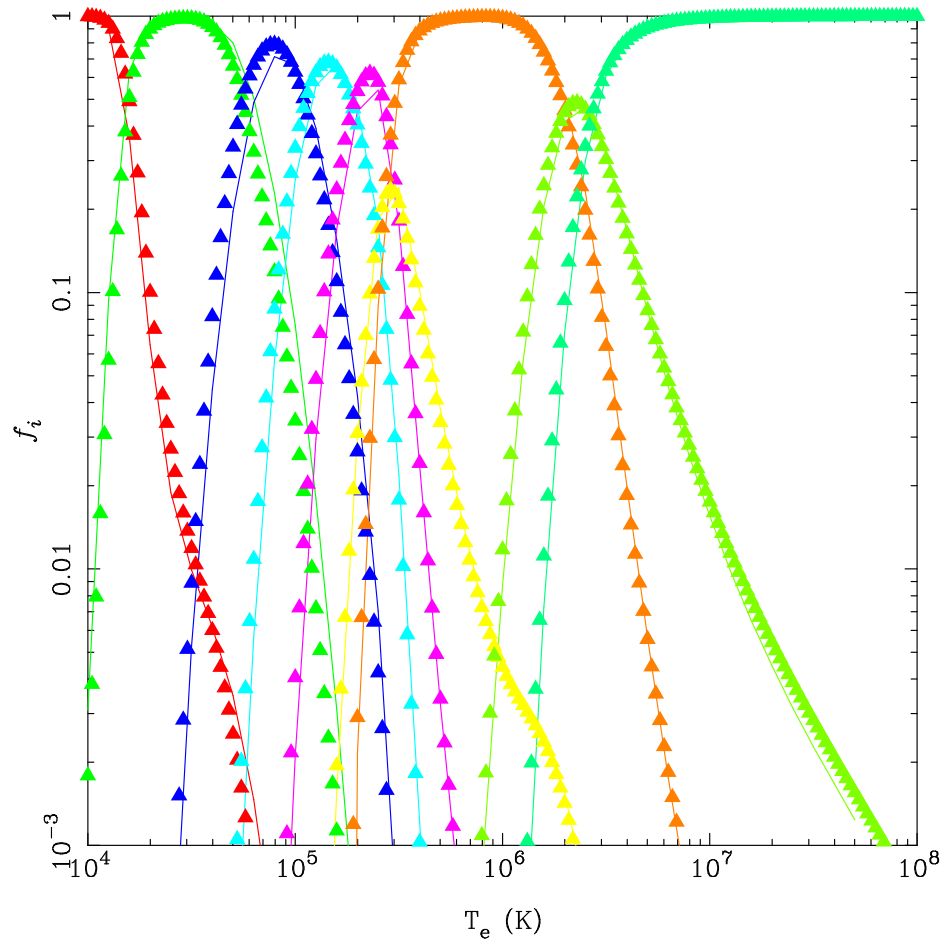


Figure 4.1 Collision ionization equilibrium for oxygen. The solid lines are calculations from our code, while the triangles are from Mazzotta et al. (1998). The slight disagreement between the two calculations are most likely due to differing atomic data.



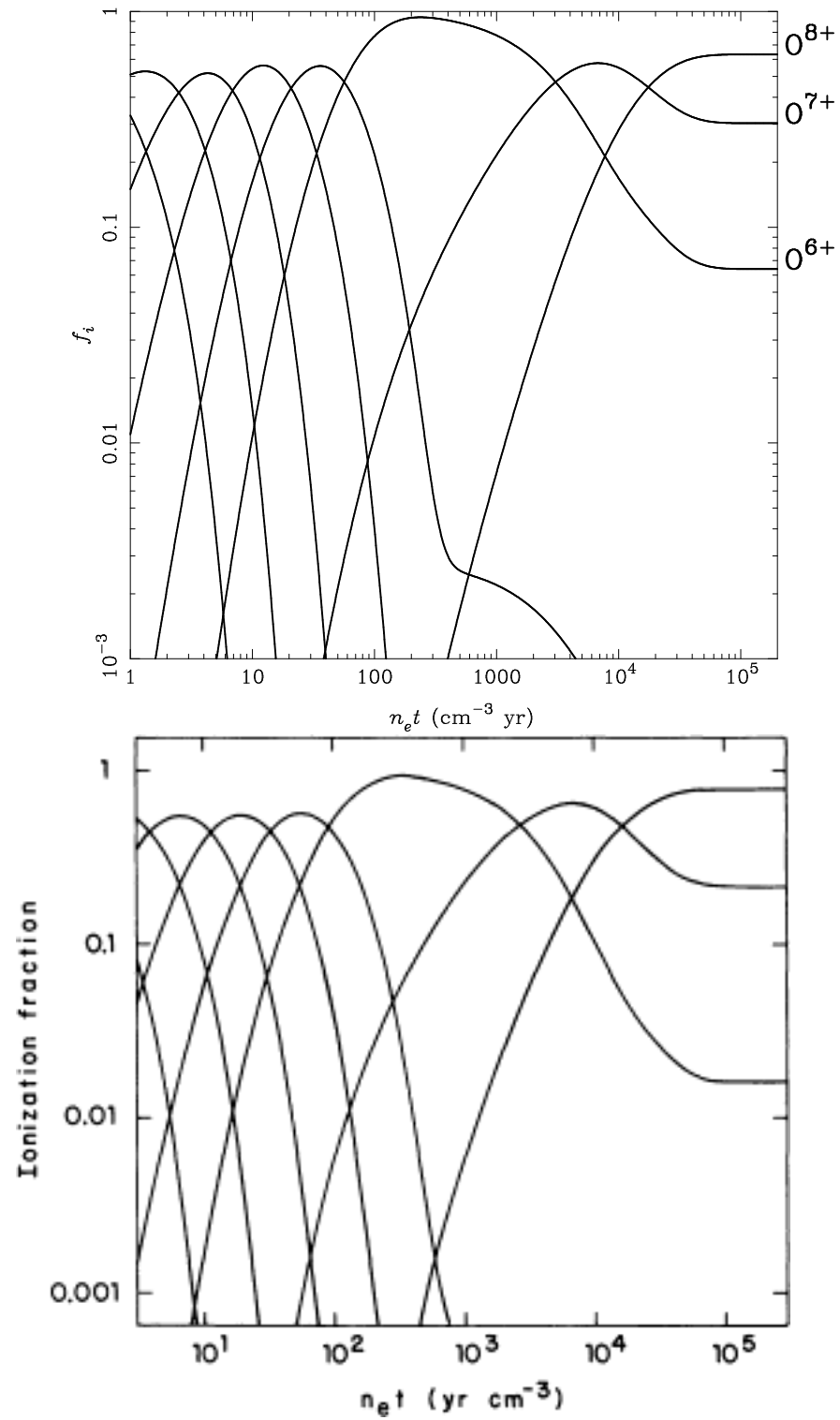


Figure 4.3 Ion fraction versus ionization age ( $n_e t$ ) for oxygen. The top figure is our calculation. The bottom figure is from Hughes & Helfand (1985).

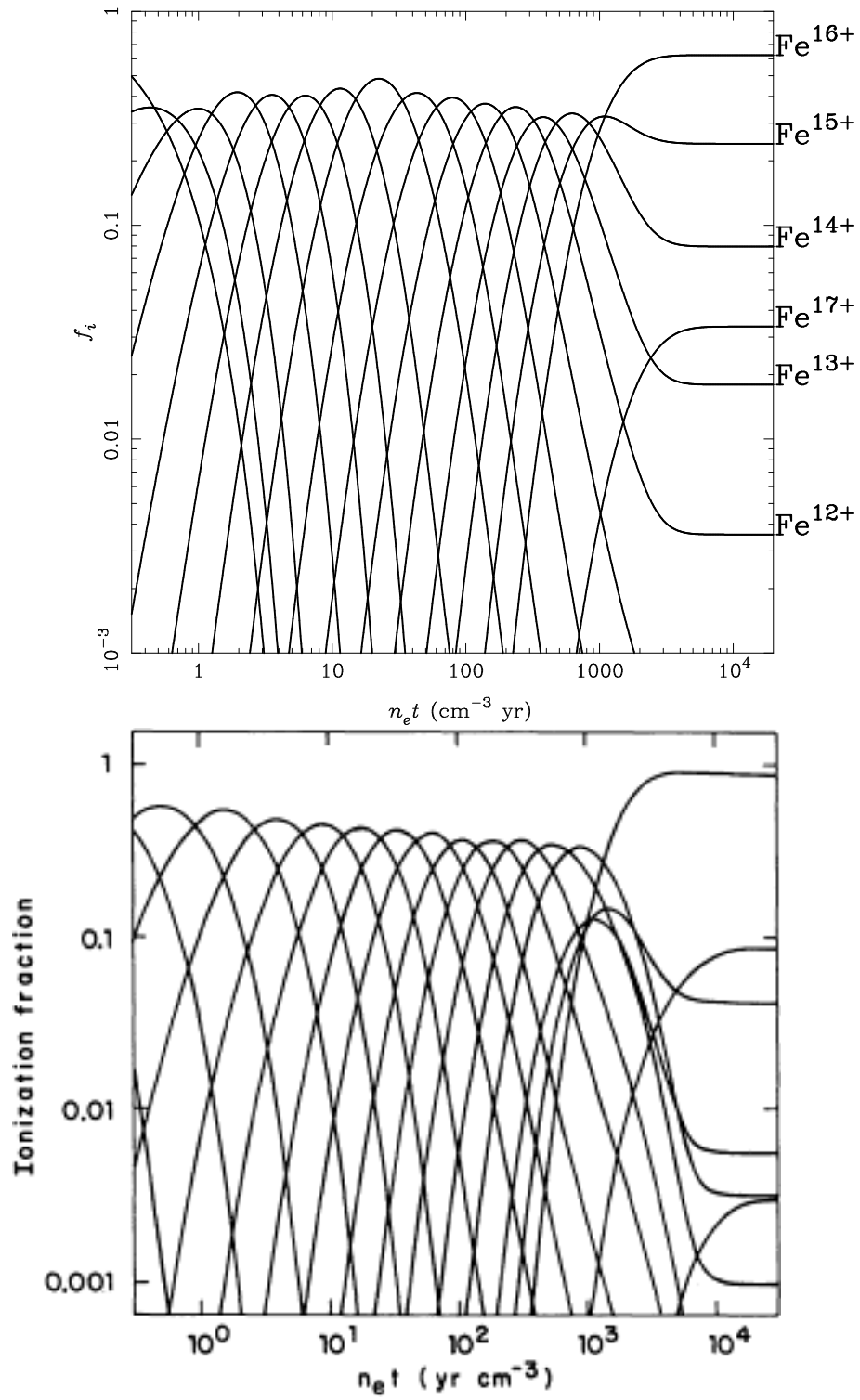


Figure 4.4 Same as Figure 4.3, but for iron.

number of elements. In addition, all simulations use a simple  $\gamma = 5/3$  equation of state (i.e. no non-thermal pressure), since the predictor-corrector algorithm for the hydrodynamic energy source equation is not yet fully tested.

Morse et al. (2004) used *HST* observations of Cas A to localize and measure the proper motion of the reverse shock, which they find on average to be propagating into a medium if  $n_{ion} \sim 0.25 \text{ cm}^{-3}$ , with  $v_{shock} \sim 2500 \text{ km/s}$ . This fast wave drives cloud shocks into denser clumps, which produce the observed optical/NIR emission. For our first set of test models, we ran a series of simulations for these parameters with 600 zones, and a computational domain of  $5 \times 10^{17} \text{ cm}$ . We initialized a 2500 km/s shock to be stationary on the mesh (i.e. the velocity upstream of the shock was 2500 km/s, and was 625 km/s after the jump). Each simulation spans 10 years of flow time, approximately equal to the cloud-crushing timescale for Cas A's optical knots.

#### 4.3.2.1 Static Shock, No Cooling

For the first simulations, we ran the code with the cooling and ionization disabled, to demonstrate the hydrodynamic module's ability to accurately reproduce the jump conditions. Figure 4.5 shows the temperature structure of two such models, one with the initial post-shock ion and electron temperatures equal, the other with  $T_{ion}/T_e = 0.2$ . In both simulations, the oxygen enters the shock preionized to He-like, which is approximately what is expected for low density gas in Cas A subject to photoionization from the shock X-rays (see Chapter 3). Since the post-shock conditions were initialized to the exact values, the shock should remain stationary on the mesh; any movement indicates conditions significantly deviant from the expectation. As can be seen, the shock is indeed stationary, and the specified post-shock temperature ratio is reproduced. In addition, Figure 4.5 also demonstrates the effect of the artificial viscosity in spreading the shock over

$\sim 5$  zones.

#### 4.3.2.2 Static Shock, With Ionization and Cooling

For the next test, we ran the same initial conditions with the cooling and ionization enabled. A 2500 km/s shock will be non-radiative, (i.e. cooling losses behind the shock front should be minimal), so it too should be stationary on the grid. In Figures 4.6 & 4.7 we plot the temperature and ionization structure for two simulated shocks, one with oxygen preionized to He-like, the other C-like. Since the post-shock temperature for a  $\gamma = 5/3$  gas and complete electron-ion equilibration is

$$T = \frac{3}{16} \frac{\mu m_p v_s^2}{k} \quad (4.61)$$

the He-like gas ( $\mu = 2.28$ ) will initially be cooler than the C-like gas ( $\mu = 5.33$ ) by the ratio of their mean molecular weights (a little more than a factor of two). This is indeed what the code produces. As the C-like gas ionizes, more free electrons are added to an essentially adiabatic gas, and the electron temperature drops. Note that the Coulomb equilibration timescale is quite long, and very little energy is exchanged between the electron and ion gases. Also note that while the equilibrium ionization state for oxygen at these extreme temperatures is fully stripped, the finite collisional ionization timescale and relatively short duration of the simulation leaves the gas far from ionization equilibrium.

#### 4.3.2.3 Dynamic Radiative Shock

The hydrodynamics are considerably more complex if line cooling behind the shock front is dynamically important. In this case, the downstream gas can radiate away a significant fraction of its internal energy, resulting in pressure gradients in the cooling zone. This leads to bulk flow in the cooling region, and variable shock conditions.

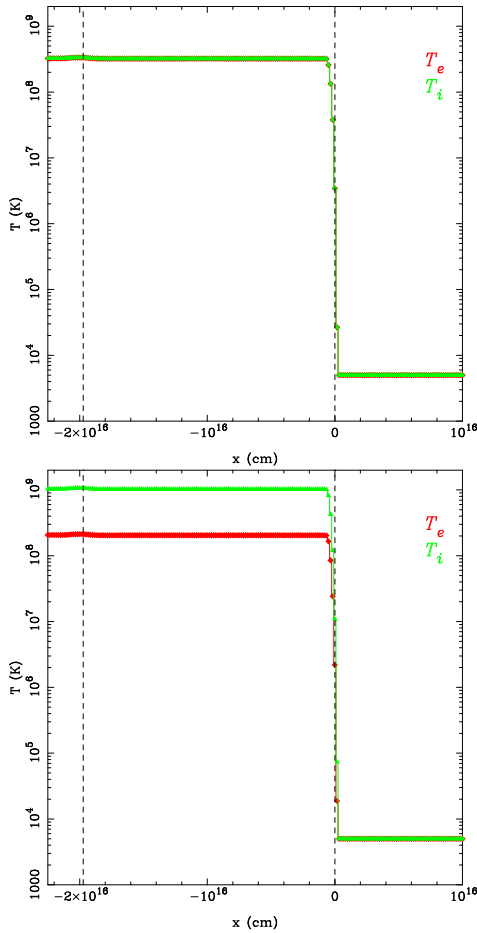


Figure 4.5 Temperature structure for a 2500 km/s shock in pure oxygen with  $n_{ion} = 0.25 \text{ cm}^{-3}$  at  $t = 10 \text{ yr}$  and with the cooling routine turned-off. The flow is from right to left, with the fluid variables set to produce a stationary shock at  $x = 0$ , denoted by the right-hand vertical dashed line. The left-hand vertical line marks the maximum extent of flow since the start of the simulation. In the top plot, the initial postshock ion and electron temperatures (a free parameter) were set to be equal; in the bottom plot  $T_e/T_{ion} = 0.2$ . In both cases, the gas enters the shock pre-ionized to  $\text{O}^{6+}$  (He-like). Note that the shock is spread over  $\sim 5$  zones, and stays stationary throughout the simulation.

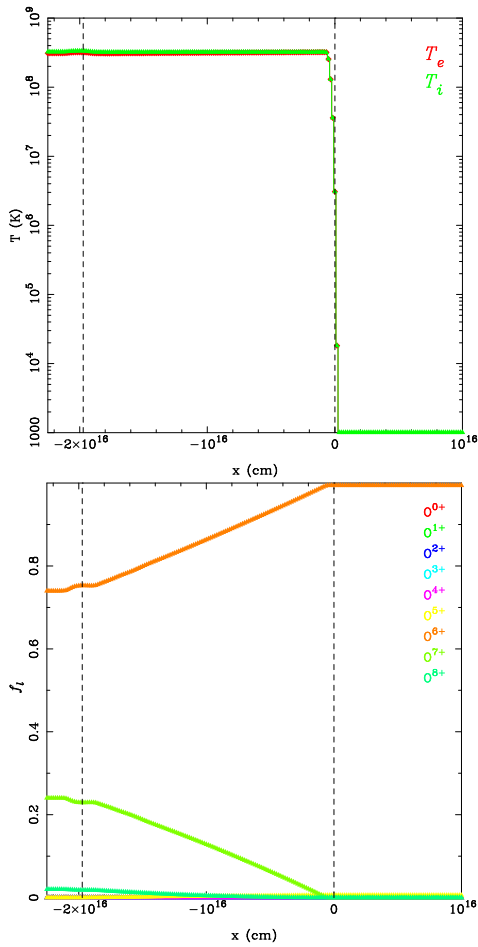


Figure 4.6 Temperature (top) and ionization (bottom) structure for a 2500 km/s shock in pure oxygen, with  $n_{ion} = 0.25 \text{ cm}^{-3}$  and  $T_{ion}/T_e = 1.0$  at  $t = 10 \text{ yr}$ . The flow is from right to left, with the fluid variables set to produce a stationary shock at  $x = 0$ , denoted by the right-hand vertical dashed line. The left-hand vertical line marks the maximum extent of flow since the start of the simulation. The gas enters the shock pre-ionized to  $O^{6+}$  (He-like), and ionizes to  $\sim 25\%$  H-like in 10 years.

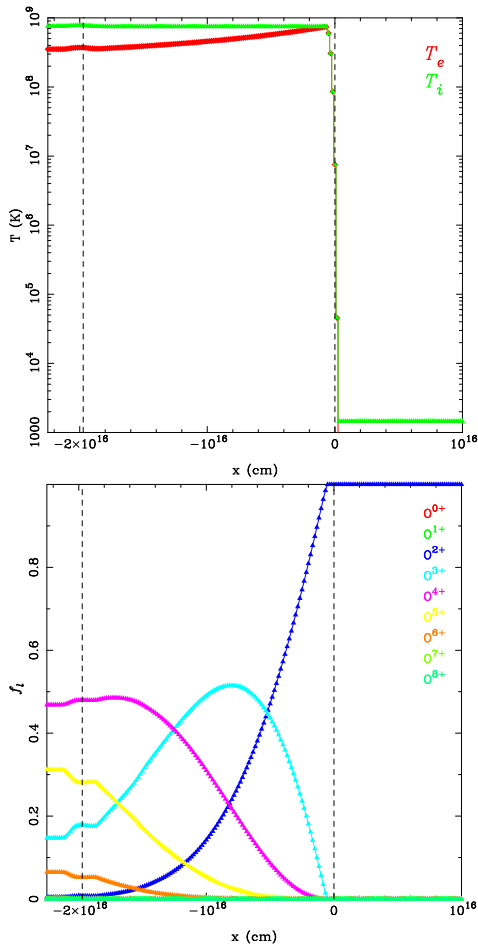


Figure 4.7 Same as Figure 4.6, except the gas enters the shock as  $O^{2+}$  (C-like). Note the initially higher temperatures relative to the He-like case because of the lower initial electron density. The electron temperature decreases as more free electrons are created by collisional ionization, increasing the number of particles at essentially constant internal energy.

These effects are demonstrated in our last set of 1D simulations. We initialized a 100 km/s shock to be initially stationary on the grid, with pre-shock density of  $n_{ion} = 25 \text{ cm}^{-3}$ . The pre-shock gas is N-like; the post-shock gas is initially C-like. Figure 4.8 shows the pressure and velocity of the initial configuration and for 500 timesteps into the simulation. At  $t \approx 2.4 \times 10^6 \text{ s}$  the pressure away from the shock is  $\sim 30\%$  its starting value, which has driven bulk flow in the downstream direction, causing the shock front to slide along the mesh towards negative  $x$ . As a result, the net velocity of the incoming gas (still at  $v_x = -100 \text{ km s}^{-1}$  on the grid) relative to the shock is less than that derived from the original jump conditions, and the post-shock pressure and the deceleration of the incoming gas are correspondingly less.

The compression of the post-shock gas driven by the shock's propagation across the grid has two effects. The electron cooling rate, proportional to  $n_{ion} n_e$ , is enhanced, while the ions, which can only cool due to Coulomb interaction with the electrons, initially increases due to  $PdV$  work. The disparity in the electron and ion temperatures then speeds the exchange of energy between the two fluids, and a quasi-equilibrium is established between line cooling and compressional and Coulomb heating (Figure 4.9), and the electron temperature is nearly constant ( $0.45 < x < 0.51$ ). Once the ion internal energy is significantly depleted and the temperatures equilibrate, compression is the main source of heat. Figure 4.10 shows the ionization fractions, pressure and velocity at the same timestep as Figure 4.9. Zones  $x < 0.35$  have not yet reacted to the shock and have cooled passively throughout the simulation. However, for cells affected by the shock, the gas is primarily  $\text{O}^{2+}$ , though earlier timesteps had a significant fraction of  $\text{O}^{3+}$ . This is a general feature of metal-rich radiative shocks — the quasi-equilibrium between line cooling and Coulomb and compressional heating results in a nearly

flat electron temperature profile, and produces a spectrum dominated by one or two ionization stages (B2000).

#### 4.4 Two Dimensional Simulation of a Shock-Cloud Interaction

##### 4.4.1 Justification for Two Dimensions

While one-dimensional test problems are useful for understanding the behavior of the code in relatively simple physical configurations, they do not represent a substantial advance over previous work. Here we present initial 2D calculations for a cloud-shock interaction in a pure oxygen gas, for conditions relevant to the radiative, optically-emitting shock waves observed in Cas A. Incorporating the multi-D hydrodynamics and NEI+cooling described in the previous sections, they are the first calculations of their kind of which we are aware.

Given its expense and complexity, the extension to multi-dimensions is best justified if there are specific questions left unanswered by simpler calculations which may be addressed by more a sophisticated simulation. In Section 4.1, we identified two such problems with the single zone calculations that may potentially be explained with non-planar flow. First, recall that typical studies with radiative shock codes have required previous authors to invoke a (usually power law) distribution of pre-shock densities to match the observed line spectrum. For example, B2000 published the most extensive comparison of models with oxygen-rich spectra, and found that the cooling times in metal-rich plasma are much faster than the recombination times, so that a nearly constant  $T_e$  post-shock flow is established, with the Coulomb interaction with the ions nearly balancing the energy loss from the electrons due to lines. (Indeed, our 1D simulation showed the same.) As such, the spectrum for a single shock speed is dominated by one or two ionization species, in contrast with their *HST* observations of

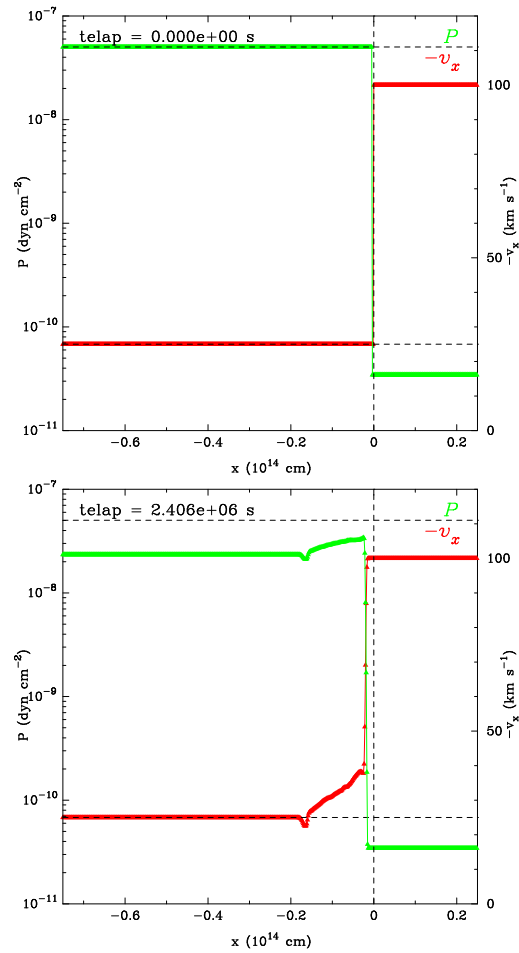


Figure 4.8 Pressure and velocity plots for a radiative shock. The top panel shows the initial conditions. The horizontal dashed lines denote the initial post-shock pressure and velocity, and the vertical dashed line is the initial position of the shock. Note that in the bottom panel cooling has reduced the post-shock pressure. This pressure gradient causes the front to move on the mesh. (The dip at  $x = 0.1$  is start-up error due to the initially discontinuous shock jump.)

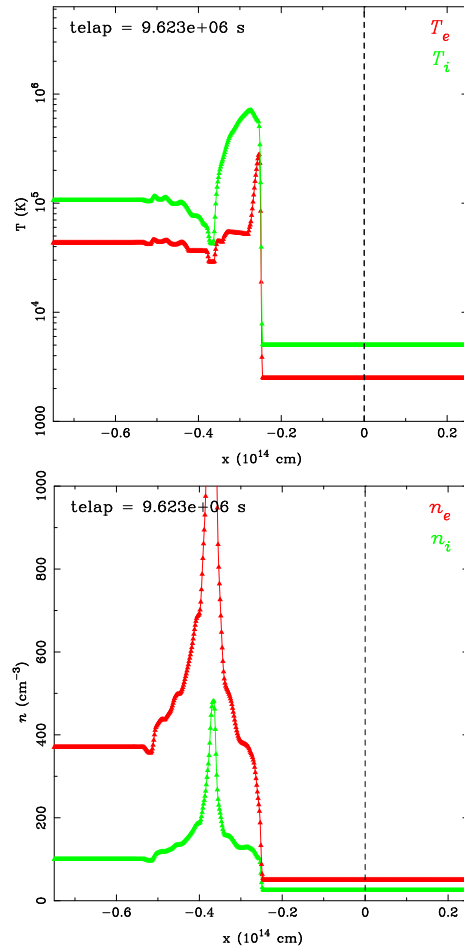


Figure 4.9 The temperature and density structure of the simulation after the shock has propagated a significant distance across the grid. The post-shock electrons cool prodigiously, until a quasi-equilibrium is established between line cooling and heating due to compression and the Coulomb interaction.

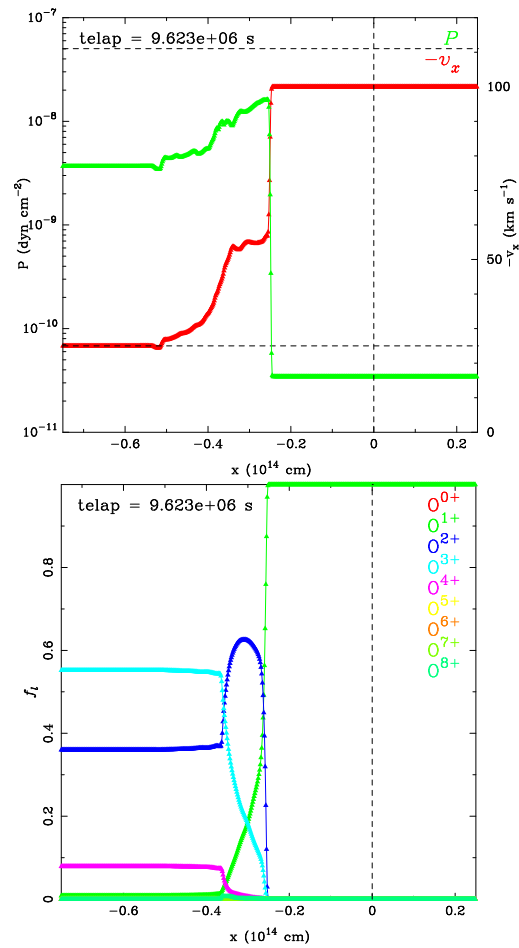


Figure 4.10 Pressure and velocity (top) and ionization fraction (bottom) at the same elapsed time as Figure 4.9. Note that the primary ion in the cooling region is  $\text{O}^{2+}$ . This shock is bright in  $[\text{O III}]$ .

N132D and E0102, which exhibit lines from many species. Second, B2000 found it necessary to impose a low-temperature cut-off to their post-shock flow in order to avoid overproducing OI recombination lines. They postulated that cooling instabilities might shred the cooling gas and break the planar flow assumption. Perhaps the cold gas compresses and presents a smaller geometric area to incoming photoionizing photons, resulting in fewer recombinations. We seek to address these questions in this Section.

As in the previous Section, we use the observations Cas A’s reverse shock by Morse et al. (2004) to guide our simulation. The basic physical situation we wish to simulate is a fast shock (i.e. Cas A’s X-ray emitting reverse shock) encountering a dense clump, driving slower cloud shocks, which may emit in the optical. For the incident shock, we used a shock velocity 2500 km/s, propagating into an unshocked pure oxygen “intercloud” medium with an ion density of  $n_{ion} = 0.25 \text{ cm}^{-3}$ . We chose  $n_{ion} = 50 \text{ cm}^{-3}$  for the cloud density for two reasons. First, a number of emission features in Morse et al. 2004’s WFPC2 images of Cas A’s knots show a non-intuitive convex morphology, when one might expect a shocked cloud to be concave. This might be explained if the secondary shock on the (windward) front of the cloud, driven by the ram pressure of the incident shock, is non-radiative and emits mostly in the X-ray and the EUV, while the backside (leeward) shock, driven only by gas pressure, is slower and radiative. Since

$$v_{cloud} \approx \sqrt{\frac{\rho_{ICM}}{\rho_{cloud}}}, \quad (4.62)$$

the initial leeward shock will be a few hundred km/s, sufficiently fast to be non-radiative. Our second reason for this choice of density is more pedagogical — this configuration demonstrates clearly the different hydrodynamics of radiative and non-radiative shocks. For the cloud, oxygen is initialized to be 100%  $\text{O}^{++}$ , with

the intercloud medium and postshock gas 100%  $O^{6+}$ . The cloud and intercloud are initially in pressure equilibrium.

We used  $750 \times 500$  zones, with a total physical extent of  $10^{15}$  cm in the  $x$ -direction. This is an order of magnitude smaller than the typical scale of an optical knot in Cas A, but given the extremely short cooling length of radiative shocks in metal-rich gas, it is not feasible to simulate a large clump. (Indeed, as we show in the next section, the leeward radiative shock is essentially unresolved even at this scale.) Due to the symmetry of the problem, to maximize resolution we only simulated half a cloud — in the following figures one of the two plotted variables is reflected about the  $y$ -axis.

#### 4.4.2 Cloud-shock Simulation

In Figures 4.11 & 4.12, we present the time evolution of the electron density and temperature for the simulation described above. The top panel of Figure 4.11 shows the incident shock sweeping past and driving a secondary shock into the front of the cloud. In the lower panel, the shock has wrapped around the cloud (i.e. reflected off the  $y = 0$  axis for our half-cloud geometry). The leeward side of the cloud is now subject to high gas pressure from the incident shock and its reflection. This pressure pushes a secondary shock into the back side of the cloud. As the simulation progress (Figure 4.12), Kelvin-Helmholtz instabilities are evident along the windward exterior; Richtmyer-Meshkov instabilities can be seen in a stream of material ablated from the cloud. At late times, the cloud is completely disrupted.

Note the relative physical extent of the hot post-shock gas in the two main cloud shocks. Behind the ram-pressure driven shock, He-like oxygen is the dominant ionization species ( $f(O^{6+}) > 0.9$ ), so cooling is inefficient and dynamically unimportant. In contrast, the leeward shock is slow enough that cooling

dramatically affects the propagation of the shock, which radiates a sufficiently large fraction of its post-shock internal energy that the cooling zone is essentially unresolved. Also of note is that this rapid cooling appears to have made the intercloud-cloud contact unstable, which has a noticeably corrugated, lumpy morphology. However, since this region is under-resolved it is difficult to make definitive statements as to whether this clumping is real, or if it might continue to break up the nearly-planar flow in the post-shock gas. To explore this further, we re-ran the simulation with the same initial conditions, but with a physical scale ten times smaller.

#### 4.4.3 The Effects of Resolution

In Figure 4.13, we show the electron temperature and average ionization state ( $n_e/n_{ion}$ ) for the original calculation (right), and the finer scale simulation (left) at approximately the same cloud-crushing time. Direct comparison is a bit tricky. Since the total elapsed time in the finer simulation is approximately ten times less, the cooling instability was able to act significantly longer in the coarse calculation. However, a few features are apparent. Indeed, at the coarse resolution the radiative shock's cooling zone is essentially unresolved, with lower temperatures and average ionization relative to the resolved case. At finer resolution, in the leeward shock  $T_e \sim 4 \times 10^5$  K, the oxygen is nearly 20%  $O^{5+}$ , and the O VI  $\lambda\lambda 1032, 1038\text{\AA}$  resonance lines provide prodigious cooling, modifying the downstream flow. Also apparent is the formation of several lower-temperature, lower-ionization (mainly  $O^{4+}$  and  $O^{3+}$ , though  $f(O^{2+}) \sim 0.05$ , producing some  $\lambda\lambda 5007, 4959\text{\AA}$  emission) clumps which are also cooling fiercely. While these dense regions are still poorly resolved, the leeward shock produces significant emission from O III - O VI, and provides tantalizing hints that hydrodynamic cooling instability produces a wider range of post-shock temperatures in the cooling

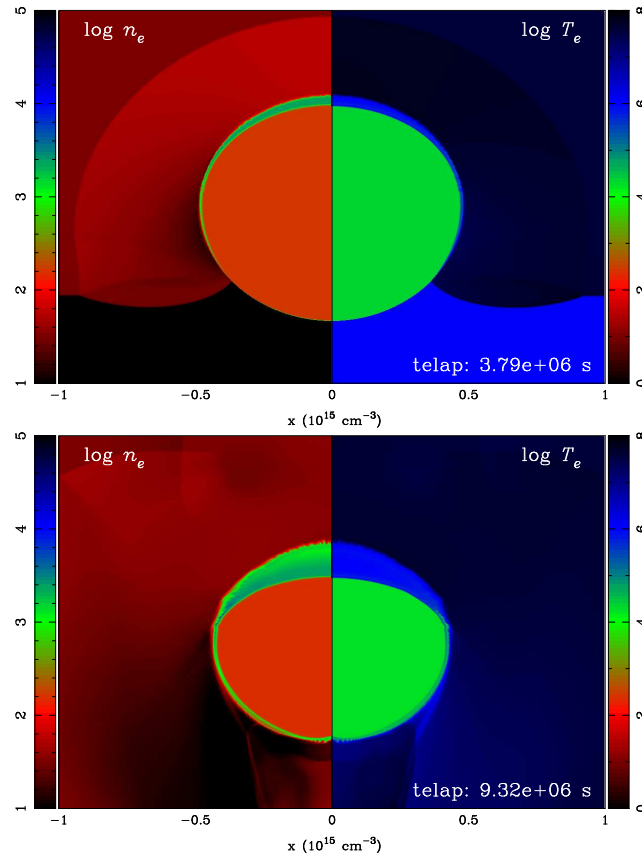


Figure 4.11 Electron densities (left) and temperatures (right, both log scale) for two outputs for the 2D cloud-shock interaction described in Section 4.4. In the top panel, the incident shock is sweeping past the cloud, and driving a non-radiative secondary shock into the windward side of the cloud. In the bottom panel, the incident shock has propagated past and wrapped around the cloud. The high pressure behind the reflected incident shock drives a slow radiative shock into the leeward side of the cloud.

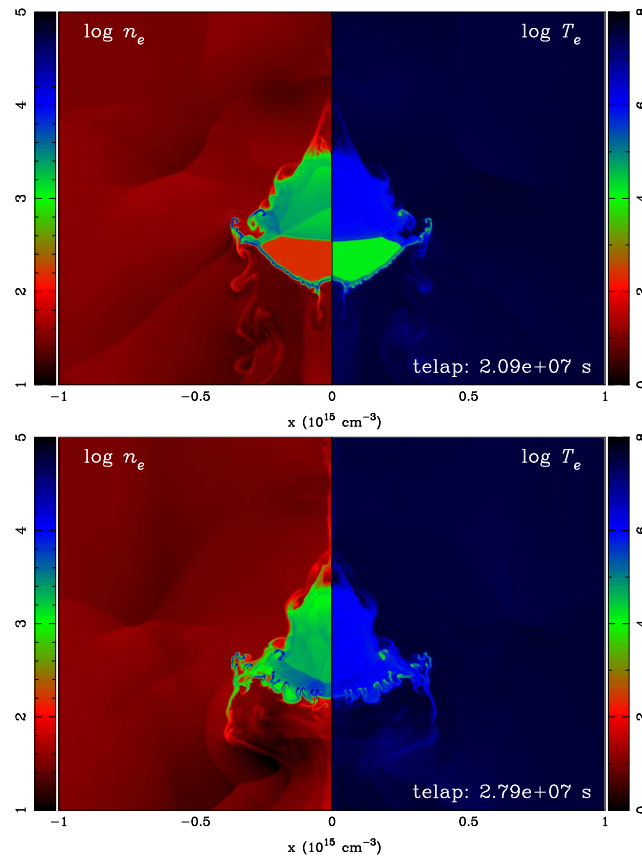


Figure 4.12 Same as Figure 4.11, for two later outputs. Kelvin-Helmholtz instabilities are evident along the front and side of the cloud, and a cooling instability has begun to corrugate the back surface. In the bottom panel, the forward cloud shock has propagated through the entire cloud and impacted the dense material in the cooling zone of the radiative shock. The cloud is nearly completely disrupted.

zone than is predicted by single-zone models. Furthermore, if this clumping continues to lower temperatures (when fully resolved), simulations such as our may provide evidence for the suppression of photoionization-recombination lines due to gas fragmentation. High resolution calculations of a subset of the physical domain explored here seem in order.

#### 4.5 Where to Go

In Section 4.1, we described the ideal calculation of supernova remnant shocks. We clearly are not there yet. However, the work in this Chapter has advanced the problem, perhaps most importantly by setting the scale of what is still yet needed, and what is possible. In this Section, I identify three unresolved issues with the current work, and discuss possible avenues for improvement.

The most obvious piece of physics missing in our current code is a radiation transport method, necessary for calculation of the photoionization rate in regions of cool gas, and in the shock precursor. In astrophysics, computational radiative transfer has largely been the domain of stellar atmosphere research and its derived fields (such as supernova calculations), where the detailed transport of the radiative flux is of paramount importance to the calculated structure and emergent spectrum. Computational methods typically derive in some degree from the diffusion approximation (e.g. the variable Eddington factor, VEF, method) which is particularly bad in the nebular condition where most zones are optically thin. One potential method, the so-called “flux-limited diffusion” (FLD, Levermore & Pomraning 1981), greatly simplifies the aforementioned VEF method by modifying the diffusion coefficient such that in regions of low optical depth the flux stays finite, and has been used successfully for neutrino transport in supernova explosion calculations (Fryer et al. 2006). However, as our problem is mostly optically

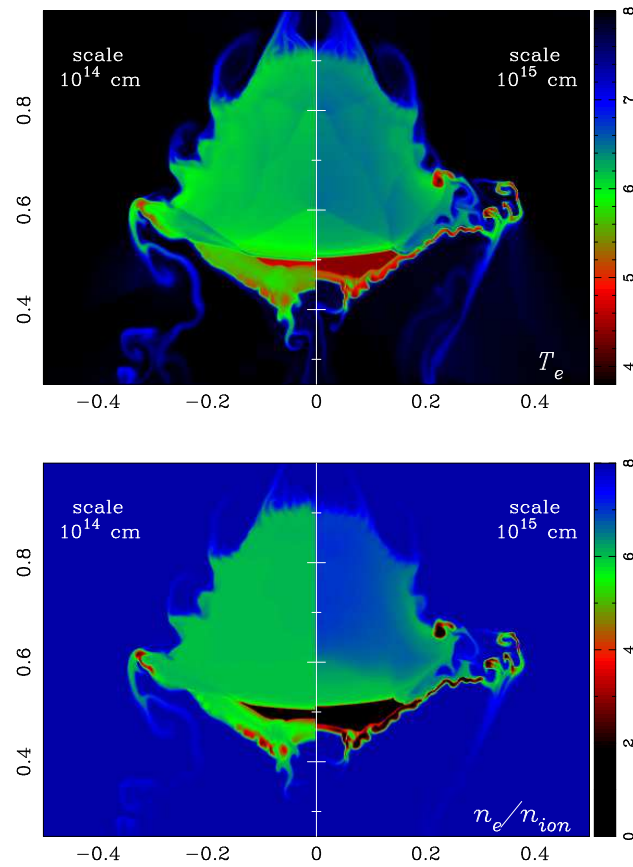


Figure 4.13 Electron temperature (top, log scale) and average ionization state ( $n_e/n_{ion}$ , bottom) for two cloud-shock simulations with identical initial conditions at nearly the same cloud-crushing time, except the physical scale of the left panel is  $10\times$  smaller.

thin, the flux limiter will almost always be active, and the solution approximate at best. Nebular radiative transfer has generally relied on even more approximate escape probabilities and the on-the-spot approximation (Ferland 2003), though recent QSO broad-line region work (e.g. Sigut & Pradhan 2003) is beginning to make use of the more advanced (and complex) accelerated lambda-iteration (Rybicki & Hummer 1991). We suggest another possibility. Monte Carlo radiative transfer methods are quite simple in principle, and for sufficiently large number of particles, nearly exact. The obvious pitfall is the great expense of a sufficiently large computation on a multi-dimensional spatial domain and multi-group frequency mesh. However, computer hardware newly accessible to general purpose programmers may make such calculations feasible on the desktop.

Despite the high clock speeds of today's CPU's (3.0 GHz in the machine used for this dissertation), much of their computational power is hampered by the relatively slow coupling to main memory (800 MHz on a good workstation). To make up for this speed mismatch, most of the silicon on a typical chip is dedicated to fast cache, leaving comparatively less room for arithmetic logic. This design has apparently lead to an actual degradation in performance for certain codes on newer, supposedly faster chips. While Moore's Law may be nearly dead for scientific computation on CPU's, the power in the graphics hardware on most new desktop machines is still growing exponentially. These GPUs (graphics process units) are highly parallel (the nVidia GE 80 has 128 cores, with nearly all of the silicon dedicated to arithmetic logic), and are able to hide memory latency for properly designed code with their parallel execution model. While the programming of GPU's for general purpose non-graphics calculations has typically been difficult, nVidia's CUDA extension to the C language makes general purpose programming for GPU's accessible to the scientific programmer. In addi-

tion, the upcoming OpenCL standard abstracts the hardware even further, and should greatly simplify coding. The highly parallel architecture of modern GPUs lends itself quite well to Monte Carlo type calculations. Indeed Alerstam et al. (2008) found a greater than  $1000\times$  speed-up in their Monte Carlo photon propagation code for biological tissues over a single CPU. It seems time to apply such power to our astrophysical problem.

Another shortcoming apparent in the 2D calculation in Section 4.4 is the dynamical range of scales in the radiative shockwave problem, particularly for the metal-rich plasma considered in this dissertation. Already our simulated shock-cloud interaction is mismatched by an order of magnitude relative to the observed optical clump scale in Cas A, and resolution is noticeably lacking in the radiative shocks on the lee of the cloud. This is a fundamental limitation of our hydrodynamic method, which can be partially ameliorated by re-simulating smaller subsets of the relevant physical domain at higher resolution. (As ad hoc as this may be, it should be noted that any two or three-dimensional problem begins with a more-or-less contrived set of spatial initial conditions.) However, if one requires truly higher dynamic range, a change of hydrodynamic method is required. The two schemes most often used in computational astrophysics to achieve orders of magnitude in physical scale are adaptive mesh refinement on Eulerian grids (AMR), or gridless Lagrangian methods. It may be interesting to integrate the cooling and NEI code here with a more advanced hydro code like FLASH or an SPH package.

Finally, our primary design choice was to focus on 2D rather than 3D in order to facilitate diagnostic and exploratory science. This is, however, not without its physical implications. Fluid instability growth in 2D and 3D dimensions is quite different, which must be considered when interpreting the results of two-

dimensional calculation. We know this intuitively from our own experience — cold milk poured into hot coffee (a 3D problem) forms unstable convective cells which decay into a fully mixed cafe-au-lait, while flows in the atmosphere (which is nearly 2D for large enough spatial scales) form pinned vortices: hurricanes. Very little in the Universe is really 2D (accretion disks may be close), and the artifacts of these limited calculations can be readily seen in monolithic shock-cloud calculations. The finely detailed filigree and structured vortex rings seen in Patnaude & Fesen (2005)'s 2D calculations devolve into turbulence in even low-resolution 3D simulations (Stone & Norman 1992a). While calculations like ours in 3D are impractical for now on the desktop (and therefore as exploratory tools), much can likely be learned from a 3D supercomputer simulation, which more closely approaches our ideal calculation.

## CHAPTER 5

## CONCLUSION

Cas A's youth, relatively small distance from Earth, and its large number of observed nuclear species provide a near unique look at the advanced burning stages and nucleosynthetic yield of massive stars and supernovae. Observations over the last decade with the NASA Great Observatories and a number of ground-based facilities, plus powerful new theoretical calculations, promise to advance greatly our understanding of this important object. To help utilize fully both these high quality data and sophisticated calculations, we have in this thesis narrowed the allowed  $^{56}\text{Ni}$  yield of Cas A's explosion, and written new tools to connect observation with theory.

### 5.1 Results

In the first science chapter (Chapter 2) of this dissertation, we sought to apply two techniques not previously utilized in Cas A to measure more accurately the reddening to the expansion center. The first, more traditional method, involved measuring spectroscopically the  $1.257\mu\text{m}$  and  $1.644\mu\text{m}$  near-IR lines of [Fe II], which arise in the same upper level, and so, in principle, should have a fixed emissivity ratio. While a measurement of the absolute value of  $A_V$  from these lines is hampered by uncertain atomic data, we were able to measure the relative extinction across a larger fraction of the remnant, into regions of higher extinction, and closer to the expansion center than had been previously reported with optical line ratios. Our second technique was more novel. In NIR images taken with PISCES on the  $90''$ , we detected for the first time in the  $J$  and  $H$  bands the non-thermal synchrotron emission from Cas A's shocks. Using the known spectral index from

published mm-wave observations, we were able to measure the departure from a pure power-law spectrum, which is well-fit by an interstellar extinction law. Using a synchrotron knot only  $13''$  from the expansion center, we find  $A_V = 6.2 \pm 0.6$ ,  $1.0 - 1.7$  mag greater than the most commonly assumed  $A_V$  toward Cas A. With an assumption of the brightest the SN could have been without wide-scale contemporary reportage, this constrains the allowed range of luminosity of the supernova. The derived  $^{56}\text{Ni}$  yield is then  $0.058 < M_{\text{Ni}} < 0.16 M_{\odot}$ . (The lower limit is from published X-ray observations.) This result, combined with the  $^{44}\text{Ti}$  yield from gamma-ray observations, produces a  $^{44}\text{Ca}/^{56}\text{Fe}$  (the stable daughter nuclei) ratio consistent with the measured solar abundance.

In Chapter 3, using simple physical arguments and detailed hydrodynamic, radiative transfer and non-equilibrium photoionization calculations (described in the Appendix), we inferred the physical conditions in the cold ejecta recently detected with the *Spitzer* IRS interior to the reverse shock in Cas A. While in-depth comparison with the observations was difficult since the observers neither published nor were willing to provide line fluxes, we were able to determine that the mid-IR knots are photoionized by the emission from the SNR shocks, that they are denser than the average expected for the interior of the remnant, and that their spectra imply abundances consistent with incomplete oxygen burning. Interestingly, the non-detection of any of the numerous iron lines in the *Spitzer* band implies that any Si-burning ashes still interior to the reverse shock are more tenuous than the O-burning products. This may either be due either to bubbles in the iron-rich material evacuated by gamma-rays from the decay of  $^{56}\text{Ni}$  and  $^{56}\text{Co}$ , or large-scale convective over-turn in the explosion, which might also have resulted in the spatial inversion of ejecta seen in X-ray observations.

Finally, we presented algorithms and early results from a new hydrodynamic

and non-equilibrium ionization and cooling code we developed to model supernova remnant shocks. With OpenMP shared-memory parallelism and modern multi-core workstations, it is now possible to run 2D hydro+NEI+cooling calculations on the desktop in times short enough to allow exploration of parameter space. Simulations of a 2D shock-cloud interaction in a pure-oxygen plasma with flow parameters relevant to Cas A show a wider range of temperatures and ionization states than is generally seen in single-zone or 1D calculations, indicating that cooling and fluid instabilities play an important role in producing the rich optical emission line spectrum seen in oxygen-rich supernova remnants.

## 5.2 Future Work

The near-IR images utilized in Chapter 2 were quite shallow (typically less than 1 hour), and were taken under sub-optimal conditions at the Bok 90". It is thus possible to do much better in a relatively small amount of time on 2 or 4 meter class telescopes. The radio maps of Cas A (which show only synchrotron emission) have much more detail than our own data, so we likely are seeing only the brightest peaks in the IR. In comparison with centimeter-wave radio (which is unaffected by interstellar extinction), spatially discrete absorbers should show up as shadows on NIR images. This could give a true measure of the patchiness of the reddening toward Cas A, and give a handle on that source of systematic error in our estimate of the supernova luminosity. In addition, departures from a true power-law could be measured in two ways. It might be possible to image directly the synchrotron emission in the  $R$ ,  $I$ , or  $z$  bands in the optical with red optimized CCDs like those in MARS, the red spectrograph on the KPNO 4 meter. Ideally, of course, one would like a dispersed spectrum of the IR emission to measure directly the IR spectral index. With NIR spectrographs on 6.5-8

m telescopes (e.g. MMIRS on the MMT, GNIRS on Gemini, or LUCIFER on the LBT), this should be feasible for the brightest knots with several hours of exposure. Finally, while it seems unlikely that the theoretical calculations of the [Fe II] transition probabilities will radically improve, we note that an empirical measurement is straightforward with an observation of both lines on the same slit in an unabsorbed object like the Cygnus Loop.

The work in Chapter 3 suggests several enhancements. First, a more realistic ionizing spectrum, incorporating the NEI line spectrum in the X-rays and EUV emission from radiative shocks, is clearly desirable, at least as a check against the simple thermal bremsstrahlung we assume. Second, comparison with actual data (!) is clearly warranted. Our communication with the authors of the first papers on the *Spitzer* IRS data have been helpful, though they have not yet agreed to collaborate or provide their data. We are also in contact with a graduate student at Minnesota who is working with a higher resolution and high sensitivity data set, though our efforts to collaborate have not yet been successful. Finally, two lines from the cold ejecta, [Fe V]  $70.4\mu\text{m}$  and [O III]  $88.4\mu\text{m}$ , are prime targets for the recently launched *Herschel* far-infrared mission, while a third, [OI]  $63.2\mu\text{m}$ , should be bright in the recombination zones of the radiative shocks. Observations with *Herschel* similar to the *Spitzer* IRS campaigns would seem to be similarly useful.

Finally, the numerical modeling in Chapter 4 is obviously still in progress, and Section 4.5 provides a long discussion of future work. The code consumed by far the most effort of any work in this dissertation, and it perhaps has the most promise for future contributions to the study of supernova remnants. The optical emission from the radiative shocks will provide the best data on Cas A for years to come, and adequate interpretation of these data requires a tool like the one I

have written. As desktop power (either in the CPU or GPU) continues to advance, 2D simulations like those we have presented will become more routine, and more physics can be added. 3D simulations are feasible with supercomputers, and would provide additional insight into the growth of fluid and cooling instabilities and the role they play in the emission spectrum of shocked metal-rich plasmas.

## APPENDIX A

A ONE DIMENSIONAL HYDRODYNAMICS, RADIATIVE TRANSFER, AND  
NON-EQUILIBRIUM IONIZATION CODE

This Appendix details the new hydrodynamic, radiative transfer, and non-equilibrium ionization code we used to calculate the time-dependent thermodynamic variables, ionization state, and heating and cooling rates for the average density interior ejecta in Cas A.

## A.1 Hydrodynamics

For the hydrodynamics, we employ a standard spherically-symmetric, one-dimensional Lagrangean method (Richtmyer & Morton 1967), which includes artificial viscosity to treat shocks. We use the finite difference scheme described in the Appendix of Truelove & McKee (1999). Energy loss due to line cooling, dust, or the acceleration of cosmic rays is assumed to be dynamically unimportant.

## A.2 Time-Dependent Ionization

The time dependence of a the ionization state for a particular element in a fluid zone is described by a coupled set system of rate equations:

$$\begin{aligned}
 \frac{1}{n_e} \frac{df_i}{dt} = & f_{i-1} q_{i-1}^{CI} + \frac{1}{n_e} \sum_{j=0}^{i-1} \left[ f_j \int_{\nu_{edge}}^{\infty} \frac{4\pi J_\nu}{h\nu} \sigma_{ji}(\nu) d\nu \right] - \\
 & - f_i \left( \alpha_i^R(T) + q_i^{CI}(T) + \frac{1}{n_e} \int_{\nu_{edge}}^{\infty} \frac{4\pi J_\nu}{h\nu} \sigma_i^T(\nu) d\nu \right) + \\
 & + f_{i+1} \alpha_{i+1}^R(T)
 \end{aligned} \tag{A.1}$$

Here,  $f_i$  is the ionization fraction, which sums to 1 for each element by construction.

The recombination coefficients  $\alpha^R(T)$  are the sum of the contributions from the radiative and dielectronic processes, and are taken from the literature as follows. For radiative recombination (RR) onto ions with 11 electrons (Na-like) initially or fewer, we use the calculations of Badnell (2006), with Mg-like coefficients from Altun et al. (2007). For initial ions with more than 12 electrons, we use the RR coefficients from Shull & van Steenberg (1982) and its Erratum. The dielectronic recombination (DR) coefficients for ions with 12 electrons and fewer are taken from new intermediate coupling calculations introduced by Badnell et al. (2003) and presented in 12 subsequent papers, while the DR data for ions beyond Mg-like is from the tabulation of Mazzotta et al. (1998). The collisional ionization coefficients  $q^{CI}$ , which include both the direct ionization and excitation-autoionization processes, are from the Flexible Atomic Code (Gu 2002) calculations of Dere (2007).

While recombination and collisional ionization connect adjacent ionization states, inner-shell photoionization can lead to the ejection of multiple electrons through the Auger process, coupling several ionization states and accounting for the summation in the second term of Equation A.1. (In actuality, photoionization can be from several subshells for a given ion; this additional summation over subshells is suppressed in Equation A.1 for clarity.) The total photoionization cross-section  $\sigma^T$  from a given shell is taken from Verner & Yakovlev (1995), and the total ejected electrons are calculated from the probabilities of Kaastra & Mewe (1993), proportioned by their respective subshells' statistical weights.

Given the necessary tabulated atomic data, photoionizing mean intensity ( $J_\nu$ , calculated as below), electron temperature and density, the ionization state of a fluid element can be calculated in either the either the steady-state ( $df_i/dt = 0$ ) or time dependent cases. The rate equations form a set of stiff ODE's, so explicit dif-

ferentiation is not practical, and we employ the implicit backwards Euler method (Press et al. ) to evolve the time dependant equations. For a given timestep, the vector of updated ionization fractions ( $\bar{f}^{n+1}$ ) for each element is solved as

$$(\mathbf{I} + \delta t \mathbf{C}) \bar{f}^{n+1} = \bar{f}^n \quad (\text{A.2})$$

by LU decomposition.  $\mathbf{I}$  and  $\mathbf{C}$  are the identity and rate coefficient (from Eq A.1) matrices, respectively.

### A.3 Radiative Transfer

The photoionization rate is proportional to the mean intensity of the ionizing radiation field,  $J_\nu$ , which is itself dependent on the emissivity and spectrum of the emitting material, the opacity of the absorbing medium, and the overall geometry of the problem. For our case of a spherically symmetric supernova remnant, we choose the simplifying geometry of an emitting annulus of zero optical depth, with inner and outer radii at the reverse and forward shocks. The interior ejecta has no emissivity, so all absorbed radiation goes to photoionization and heat. The actual emission spectrum of Cas A's shocks is quite complex since it consists of the superposition of several fluids of variable composition, density, non-equilibrium ionization and non-azimuthally nor radially symmetric spatial distribution. In principle one could couple our 1D hydrodynamic and ionization calculations with a complex plasma emission model such as APEC (Smith et al. 2001) or the Raymond-Smith code (Raymond & Smith 1977), though given the magnitude of the asymmetric systematic effects listed above, we have enlisted an additional simplifying assumption, and set the emission spectrum to be the sum of two thermal bremsstrahlung spectra (Rybicki & Lightman 1979), one each for the reverse and forward shocks, with normalizations set to produce luminosities

of each component at  $t_{SNR} = 330 \text{ yr}$  to match the observed  $0.5 - 10 \text{ keV}$  brightness in the spatially summed *BeppoSAX* observations of Favata et al. (1997). The post-shock temperatures are calculated directly from the hydrodynamics, using emission measure-weighted averages of zones between the reverse shock and contact discontinuity for the shocked ejecta, and between the contact and blast wave for the circumstellar material. Assuming complete H and He ionization behind the blast wave and He-like metals in the ejecta, an ion to electron temperature of  $T_e/T_i = 0.08$  provides a reasonable match to the present day shock temperatures. Our choice of a pure bremsstrahlung spectrum decreases the sensitivity to the exact electron temperature of the X-ray/EUV emitting gas since  $T_e$  primarily sets the location of the exponential cut-off in flux, which stays considerably harder than the energies where most of the photoionizations occur (from 30 to a few hundred eV). We discretize the ionizing spectrum in logarithmic energy bins of  $\Delta \log_{10} E = 0.1$  from just below the softest ionization edge considered (Ca I at 6.1 eV) to 10 keV.

As demonstrated in Section 2, late in the supernova remnant evolution the mean density interior ejecta are optically thin to ionizing radiation from the shocks. However, at early times the densities are much higher and typical ions retain many more electrons, so the ejecta are quite optically thick. Calculation of the ionization and thermal states of the cold ejecta thus requires a method of radiative transfer. Hummer & Rybicki (1971) developed an elegant numerical algorithm (also described in detail by e.g. Mihalas & Weiber-Mihalas 1999 and Castor 2004), for transfer of radiation in spherically symmetric stellar atmospheres. We use their geometric construction, summarized here, to calculate  $J_\nu$ .

For set time intervals (typically every 100 hydrodynamic timesteps), we interpolate the ion density and ionization fractions for all hydrodynamic zones in-

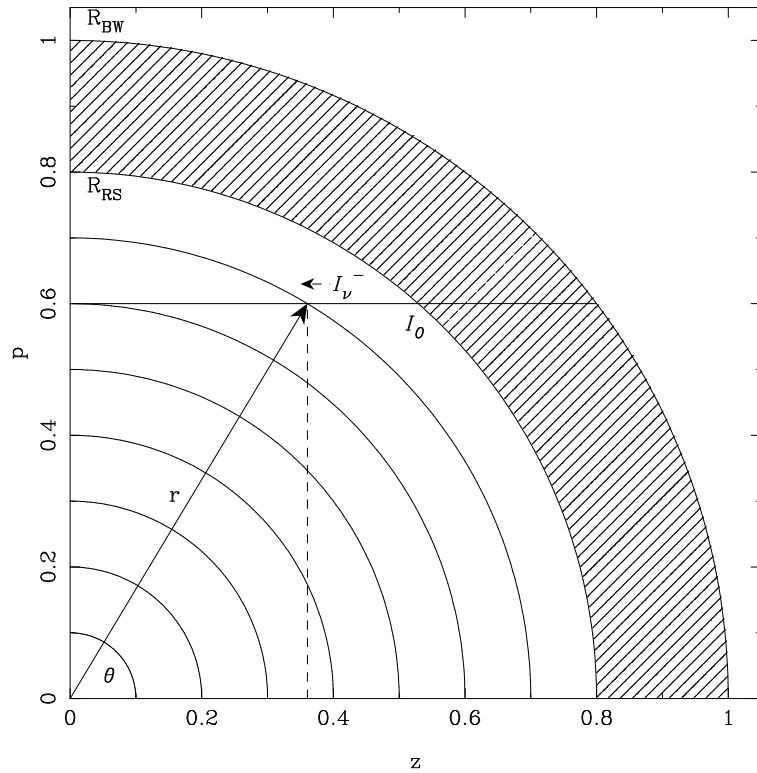


Figure A.1 Radiative transfer geometry. Rays emerge from the emitting region between the shocks with specific intensity  $I_0$  and run along constant impact parameter  $p$ . The radial zones are intersected by an increasing number of rays for higher radius, accounting for the greater anisotropy of the radiation field closer to the shocks.

terior to the reverse shock onto equally spaced radial shells, and impose a rectangular grid of impact parameter  $p$  and tangent distance  $z$  (Figure A.1). In this construction,

$$z = \sqrt{r^2 - p^2} = \mu r \quad (\text{A.3})$$

where  $\mu = \cos \theta$ , the angle cosine. We then solve the transfer equation for  $I_\nu$  along rays of constant impact parameter (i.e. tangent to the radial shells). Where these tangent rays intersect a radial coordinate, and making use of  $\mu = z/r$ ,

$$I_\nu(r, \mu) = I_0 \exp\left(-n_{ion} \Delta z \sum_j^{NZ} \sum_i^{Z(j)} \sum_k^{N\nu} X_j f_j \sigma_{ijk}\right) \quad (\text{A.4})$$

$$I_{\nu 0} = l \left( \epsilon^{BW} e^{-h\nu/kT_e^{BW}} + \epsilon^{RS} e^{-h\nu/kT_e^{RS}} \right) \quad (\text{A.5})$$

$$l = r_{BW} - \sqrt{r_{RS}^2 - p^2} \quad (\text{A.6})$$

where the sums in Equation A.4 are over the the fractional abundance of each element ( $X_j$ ), the ion fraction per element ( $f_i$ ), and radiation bins. Equations A.5 and A.6 account for limb brightening in the emitting annulus. The tangent rays intersect a greater number of radial shells with increasing impact parameter, allowing better sampling at higher radii, where the intensity is more anisotropic. From these  $I_\nu$  we obtain the mean intensity as a function of radius by numerical integration

$$J_\nu(r) = \int_0^1 I_\nu^+(r, \mu) + I_\nu^-(r, \mu) d\mu \quad (\text{A.7})$$

where  $I_\nu^-$  and  $I_\nu^+$  denote the inward and outward traveling rays, respectively. For our calculations, we used 200 radial shells. Fewer zones produce shallower absorption edges, while more zones show little difference in the calculated  $J_\nu$ .

#### A.4 Line Cooling, PI Heating, and Coulomb Equilibrium

The thermal evolution of the unshocked ejecta is determined by the interplay of adiabatic cooling (accounted for in the hydrodynamics), heating due to photoionization (calculated from the radiative transfer), and cooling due to collisionally excited line radiation, discussed here. Equation 3.1 showed the temperature dependence of an isolated transition, though the general problem involves the construction of a rate matrix for each ion describing the population of each level by collisional excitation, and de-excitation by another collision, or radiation of a photon. In practice, this is quite expensive for a simulation involving hundreds or thousands of computation zones and perhaps tens of thousands of time steps. Instead, we pre-tabulated a cooling curve for every ion considered with sufficient atomic data. For ions with forbidden lines significantly affected by collisional de-excitation, we generated curves for several electron densities, and obtained the cooling coefficient by 2D linear interpolation in  $(T_e, n_e)$  space. The cooling for all other ions was calculated by linear interpolation in electron temperature. The cooling rate due to lines is thus

$$Q^{line} = -n_e n_{ion} \sum_j^{N_Z} \sum_i^Z X_j f_i \Lambda_{ij}^{line}(T_e, n_e). \quad (\text{A.8})$$

In order to calculate the rate matrix, it is necessary to know the ion energy levels and statistical weights, and effective collision strengths for each collisionally excited transition, and the Einstein  $A_{if}$  transition probability for each radiative decay. Since we are concerned only with the cooling of the ejecta, we consider O, Ne, Mg, Si, S, Ar, Ca, and Fe. For most ions of most of these elements, the CHIANTI 5.2 database (Dere et al. 1997, Landi et al. 2006) provides sufficient atomic data. Where some or all data for a particular ion was missing, we supplemented the CHIANTI data with Iron Project (Hummer et al. 1993) calculations

from the TIPBASE database. The following ions required Einstein  $A_{ij}$  values and other data either missing from or incorrect in both CHIANTI and TIPBASE: O I (Bhatia & Kastner 1995, including level data and collision strengths, and Berrington 1988 for low temperature collision strengths), Ar II (taken from the XSTAR database, Bautista & Kallman 2001), Ca II (Meléndez et al. 2007, all data), Ca IV (XSTAR), Fe I (Fuhr & Wiese 2006), Fe II (the CHIANTI 5.2 Einstein  $A_{ij}$ 's are erroneous, Nussbaumer & Storey 1988, Quinet et al. 1996), Fe III (XSTAR), Fe IV (Nahar 2006), Fe V (Nahar et al. 2000). We were unable to locate sufficient data for all neutrals except those listed above (likely unimportant because of their vanishing  $\mathcal{Y}$  at low  $T_e$ ) Mg III and Ca III (closed shell, so unimportant), and Ca VI. For a number of ions, collision strengths are only available for the lowest terms, adequate for low temperature calculations like those described in Section 4 though not for a more general model. A more detailed listing of the atomic data used in our cooling curves will be given in a future work (Eriksen et al., in prep).

Line cooling is offset by heating due to photoionization. We make the approximation that 100% of the photon energy above the ionization potential is deposited as a photoelectron and instantaneously thermalized. The assumption of rapid thermalization is a particularly bad approximation for the cases of inner-shell photoionization, where Auger electrons of perhaps several hundreds to a few thousand eV are injected into gas with  $kT \sim 1\text{eV}$ . These highly suprathermal electrons may collisionally ionize nuclei or excite atomic levels well above  $kT$ , producing emission lines not typical of the thermal gas temperature. These photons themselves may be capable of ionization. Shull & van Steenburg (1985) used Monte Carlo simulations to explore this effect in cosmic abundance gas, and found that for gas with a 50% ionization fraction, 92% of the photoelectron's energy went to heat, increasing with higher degrees of ionization. However, their

results are presented as a function of hydrogen ionization fraction, which is obviously not applicable to the current problem. For the pure metal abundances in Cas A's ejecta, this effect is a considerably larger problem to model, requiring sampling of thousands of atomic levels and dozens of shells from which to ionize, and is clearly beyond the scope of the current work. Absent a practical prescription for handling these suprathermal electrons, the heating due to photoionizations is

$$Q^{PI} = \sum_j^{N_z} \sum_i^{Z(j)} \sum_k^{N_s} \left( \chi_{ijk} - n_{ion} X_j f_i \int_{\nu_0}^{\infty} 4\pi J_\nu \sigma_{ijk}(\nu) d\nu \right) \quad (\text{A.9})$$

where  $\chi_{ijk}$  is the ionization potential for a particular shell, and the sums are over element, ionization state, and shell. For low ionization gas with significant optical depth to inner-shell photoionization, the ionization state may be underestimated, and the temperature overestimated.

Recombination and collisional ionization also remove internal energy from the electron gas. The exact calculation for recombination requires a convolution of the electron velocity distribution with the energy-dependent recombination cross section, which can include complex resonance structure, particularly for DR. While reliable cross sections are now becoming available, cooling due to recombination is a subdominant effect in our calculations, and we use the approximation in Equation A.10, which is exactly correct for RR if  $\sigma \propto v^{-2}$ .

$$Q^{\alpha q} = - n_e n_{ion} \sum_j^{N_z} \sum_i^{Z(j)} X_j f_i \left( k_B T_e \alpha_{ij}^R(T_e) + \chi_{ij} q^{CI}(T_e) \right). \quad (\text{A.10})$$

For most conditions in our models, PI is the dominant ionization process, and the cooling due to CI is negligible.

The heating and cooling processes previously discussed only directly affect

the electron gas. However, the electrons and ions are coupled through the Coulomb interaction, which we model with the prescription from Spitzer (REF)

$$Q^{Coul} = \frac{3 n_{ion} n_e k_B (T_{ion} - T_e) \bar{Z}^2 \ln \Lambda}{503 \bar{A} T^{3/2}} \quad (\text{A.11})$$

where  $\ln \Lambda$  is the Coulomb integral and is approximately 11-21 for most conditions in our models.

### A.5 Initial Conditions

In the early evolution of a young supernova remnant, the cold, dense, and freely-expanding ejecta acts as a piston, driving a blast wave into a circumstellar environment shaped by the pre-supernova evolution of the progenitor star. Simulation of this physical configuration requires a specification of the initial ejecta and circumstellar density and velocity profiles. We use the parameterization Truelove & McKee (1999) employed for their similarity solutions in setting these initial conditions. For core-collapse supernovae, the ejecta density is typically modeled with two components: a power law envelope and a constant density core, with the transition occurring at velocity coordinate  $w_{core}$  (a free parameter). Together with a choice for the explosion energy, ejecta mass, and power law index this completely specifies the initial density and velocity.

Our goal was to produce a plausible time dependent hydrodynamic history of Cas A rather than an perform an exhaustive exploration of parameter space; we sought a single set of values for the ejecta index, ejecta mass, explosion energy, and  $w_{core}$  that sufficiently reproduced the current positions of the forward and reverse shocks in Cas A. The degree to which this can be accomplished is dependent on the validity of our assumptions of spherical symmetry and non-radiative shocks. Indeed, Patnaude & Fesen (2009) find that efficient cosmic ray accelera-

tion in the blast wave (neglected in our code) is necessary in order to reproduce the positions of the shocks and the blast wave velocity implied by X-ray proper motions. In addition, the remnant itself shows obvious signs of inhomogeneity and asymmetry. With that those caveats in mind, we were able to find a set of parameters that describe Cas A sufficiently to move forward.

In comparing their self-similar hydrodynamic and one zone non-equilibrium ionization models with the *Chandra* data for Cas A, Laming & Hwang (2003) found power-law indices of  $7 < n < 9$  best reproduced the X-ray spectra. For our models, we set  $n = 9$  and  $w_{core} = 0.5$ , though we have found varying the ejecta power-law index within the range allowed by Laming & Hwang does not appreciably change the results for our unshocked ejecta. We used  $E_{51} = 3$  (i.e.  $3 \times 10^{51}$  erg) for the explosion energy, slightly higher than the  $E_{51} = 2$  preferred by Young et al. (2006), and set the ejecta mass to  $4M_{\odot}$ . For the circumstellar density, we assumed a  $\rho(r) \propto r^{-2}$  profile appropriate for a constant velocity stellar wind, normalized to sweep up  $8M_{\odot}$  of material at  $t_{SNR} = 330$  years, in order to match the *XMM-Newton* observations of Willingale et al. (2003). In calculating our models, we used 1000 equal mass radial zones, half in the ejecta and half in the circumstellar medium. Our choice of parameters gives  $r_{BW} = 8 \times 10^{18}$  cm and  $r_{RS} = 5.5 \times 10^{18}$  cm at  $t_{SNR} = 330$  years.

Since core-collapse supernovae produce the bulk of the  $\alpha$ -elements in the Universe, Cas A's summed metal abundance yield must not be too far from the solar ratios. While the pre-SN star likely had highly layered chemical stratification of various burning shells, the observed spectra of its optically emitting ejecta show a high degree of mixing, with individual knots exhibiting lines from oxygen through iron (Hurford & Fesen 1996). We include the elements O, Ne, Mg, Si, S, Ar, Ca, and Fe with number fractions listed in Table 3.1. Absent a physical model

for the degree of mixing in the supernova, we assign a uniform (i.e. fully-mixed) abundance pattern throughout the ejecta.

The hydrodynamic variables are initialized as described as above and in Truelove and McKee (1999), with the ejecta expanding freely into the circumstellar medium a few years after the supernova explosion. The code runs just the hydrodynamics module for 2000 timesteps ( $t_{SNR} \sim 15$  yr), during which time the simulation develops well formed forward and reverse shocks.

After this start-up, the codes initializes the hydro zones interior to the reverse shock (hereafter the “interior zones”) with starting guesses for the ionization fractions and temperature, and maps these cells onto the radiative transfer grid. The steady-state ionization fractions are calculated, and the temperature is adjusted so that the PI heating and cooling do to line emission and expansion balance. This process is iterated to convergence.

#### A.6 Subsequent Execution

Once the initial ionization fractions and temperatures are determined, the execution of the full calculation proceeds. The location of the reverse shock is defined to be five zones interior to the the local maximum of the artificial viscosity at the smallest radius, and the electron and ion internal energy densities are calculated for all interior zones. The timestep for each iteration is set by the CFL condition, which, throughout the simulation, is shortest in the zones close to the contact discontinuity (i.e. away from the interior ejecta). At each time step, the electron and

ion internal energy densities are updated as

$$\dot{u}_e = - Q^{line} - Q^{\alpha q} + Q^{PI} + Q^{Coul} \quad (\text{A.12})$$

$$\dot{u}_{ion} = - Q^{Coul} \quad (\text{A.13})$$

$$u_e^{n+1} = u_e^n + \dot{u}_e^n \Delta t \quad (\text{A.14})$$

$$u_{ion}^{n+1} = u_{ion}^n + \dot{u}_{ion}^n \Delta t \quad (\text{A.15})$$

and the electron and ion temperatures are recalculated. The superscripts  $n$  and  $n + 1$  denote time evolution and  $\Delta t$  is usually the CFL timestep. However, if the full timestep will cause a greater than 10% change in either internal energy density, the timestep for that zone is reduced to  $0.1 \Delta t_{CFL}$ , and 10 subcycles are taken, recalculating  $T_e$ ,  $T_{ion}$ ,  $Q^{line}$ , and  $Q^{Coul}$  at each substep.

Every 10 hydro timesteps, the non-equilibrium ionization is advanced for all interior zones using the current densities, electron temperatures, a mean intensities. Every 100 timesteps, the reverse shock is relocalized, and the ionization fractions and densities for all interior zones are interpolated unto the radiative transfer grid.  $J_\nu$  and the photoionizations rates are recalculated, and mapped back onto the hydrodynamic zones.

## REFERENCES

- Alerstam, E., Svensson, T., & Andersson-Engels, S. 2008, *J. Biomedical Optics*, 13, 6
- Allen, G. E., et al. 1997, *ApJL*, 487, L97
- Alpher, R. A., Bethe, H., & Gamow, G. 1948, *Phys. Rev.*, 73, 7, 803
- Altun, Z., Yumak, A., Badnell, N. R., Colgan, J., & Pindzola, M. S. 2004, *A&A*, 420, 775
- Altun, Z., Yumak, A., Badnell, N. R., Loch, S. D., & Pindzola, M. S. 2006, *A&A*, 447, 1165
- Altun, Z., Yumak, A., Yavuz, I., Badnell, N. R., Loch, S. D., & Pindzola, M. S. 2007, *A&A*, 474, 1051
- Anders, E., & Grevesse, N. 1989, *Geochim. Cosmochim. Acta*, 53, 197
- Arnett, W. D. 1975, *ApJ*, 195, 727
- Arnett, D. 1996, *Supernovae and Nucleosynthesis*, (Princeton, NJ: Princeton University Press)
- Ashworth, W. B., Jr. 1980, *J. Hist. of Astron.*, 11, 1
- Baade, W., & Minkowski, R. 1954, *ApJ*, 119, 206
- Baade, W., & Zwicky, F. 1934, *Phys. Rev.* 45 , 138
- Badnell, N. R., et al. 2003, *A&A*, 406, 1151
- Badnell, N. R. 2006, *ApJS*, 167, 334

- Badnell, N. R. 2006, *A&A*, 447, 389
- Bautista, M. A., & Badnell, N. R. 2007, *A&A*, 466, 755
- Bautista, M. A., & Kallman, T. R. 2001, *ApJS*, 134, 139
- Bethe, H. A. 1939, *Phys. Rev.*, 55, 434
- Berrington, K. A. 1988, *J. Phys. B*, 21, 1083
- Bhatia, A. K., & Kastner, S. O. 1995, *ApJS*, 96, 325
- Bionta, R. M., Blewitt, G., Bratton, C. B., Caspere, D., & Ciocio, A. 1987, *Physical Review Letters*, 58, 1494
- Blair, W. P., et al. 2000, *ApJ*, 537, 667
- Bohlin, R. C. 2007, in *ASP Conf. Ser. 364, The Future of Photometric, Spectrophotometric, and Polarimetric Standardization*, ed. C. Sterken (San Francisco, CA: ASP), 315
- Bowers, R. L. & Wilson, J. R. 1991, *Numerical Modeling in Applied Physics and Astrophysics*, (Boston, MA: Jones and Bartlett)
- Cameron, A. G. W. 1955, *ApJ*, 121, 144
- Cardelli, J. A., Clayton, G. C., & Mathis, J. S. 1989, *ApJ*, 345, 245
- Chandra, R., Dagum, L., Kohr, D., Maydan, D., McDonald, J. & Menon, R. 2001, *Parallel Programming in OpenMP*, (San Francisco: Academic Press)
- Chevalier, R. A., & Oishi, J. 2003, *ApJL*, 593, L23
- Clayton, D. D. 1983, *Principles of Stellar Evolution and Nucleosynthesis*, (Chicago: The University of Chicago Press)

- Colgan, J., Pindzola, M. S., Whiteford, A. D., & Badnell, N. R. 2003, *A&A*, 412, 597
- Colgan, J., Pindzola, M. S., & Badnell, N. R. 2004, *A&A*, 417, 1183
- Colella, P., & Woodward, P. R. 1984, *J. Comput. Phys.*, 54, 174
- Cox, D. P. 1972, *ApJ*, 178, 143
- Cox, D. P., & Raymond, J. C. 1985, *ApJ*, 298, 651
- Cutri, R. M., et al. 2006, Explanatory Supplement to the 2MASS All Sky Data Release and Extended Mission Products, <http://www.ipac.caltech.edu/2mass/releases/allsky/doc/explsup.html>
- de Vaucouleurs, G., & Corwin, H. G., Jr. 1985, *ApJ*, 295, 287
- Dere, K. P., Landi, E., Mason, H. E., Monsignori Fossi, B. C., & Young, P. R. 1997, *A&AS*, 125, 149
- Dere, K. P. 2007, *A&A*, 466, 771
- Eichler, D. 1984, *ApJ*, 277, 429
- Ennis, J. A., Rudnick, L., Reach, W. T., Smith, J. D., Rho, J., DeLaney, T., Gomez, H., & Kozasa, T. 2006, *ApJ*, 652, 376
- Favata, F., et al. 1997, *A&A*, 324, L49
- Ferland, G. J. 2003, *ARA&A*, 41, 517
- Fesen, R. A., Pavlov, G. G., & Sanwal, D. 2006, *ApJ*, 636, 848
- Fryer, C. L., Rockefeller, G., & Warren, M. S. 2006, *ApJ*, 643, 292

- Fryxell, B., et al. 2000, *ApJS*, 131, 273
- Fuhr, J. R., Wiese, W. L. 2006 *J. Phys. Chem. Ref. Data* 35, 1669
- Fynbo, J. P. U., et al. 2006, *Nature*, 444, 1047
- Fryer, C. L., Hungerford, A. L., & Young, P. A. 2007, *ApJL*, 662, L55
- Gaetz, T. J., Edgar, R. J., & Chevalier, R. A. 1988, *ApJ*, 329, 927
- Galavis, M. E., Mendoza, C., & Zeippen, C. J. 1995, *A&AS*, 111, 347
- Gerardy, C. L., & Fesen, R. A. 2001, *AJ*, 121, 2781
- Ghavamian, P., Laming, J. M., & Rakowski, C. E. 2007, *ApJL*, 654, L69
- Godunov, S. K. 1959, *Mat. Sb.* 47, 271
- Gotthelf, E. V., Koralesky, B., Rudnick, L., Jones, T. W., Hwang, U., & Petre, R. 2001, *ApJL*, 552, L39
- Gray, R. O., & Corbally, C. J. 1994, *AJ*, 107, 742
- Gredel, R., & Reipurth, B. 1993, *ApJL*, 407, L29
- Gu, M. F. 2002, *ApJL*, 579, L103
- Hammell, M. C., & Fesen, R. A. 2008, *ApJS*, 179, 195
- Hartigan, P., Raymond, J., & Hartmann, L. 1987, *ApJ*, 316, 323
- Hartigan, P., Raymond, J., & Pierson, R. 2004, *ApJL*, 614, L69
- Hirata, K., Kajita, T., Koshiya, M., Nakahata, M., & Oyama, Y. 1987, *Physical Review Letters*, 58, 1490

- Huang K. N., 1985, ADNDT 32, 503
- Hughes, J. P., & Helfand, D. J. 1985, ApJ, 291, 544
- Hughes, J. P., Rakowski, C. E., Burrows, D. N., & Slane, P. O. 2000, ApJL, 528, L109
- Hummer, D. G., & Rybicki, G. B. 1971, MNRAS, 152, 1
- Hummer, D. G., Berrington, K. A., Eissner, W., Pradhan, A. K., Saraph, H. E., & Tully, J. A. 1993, A&A, 279, 298
- Hurford, A. P., & Fesen, R. A. 1996, ApJ, 469, 246
- Hoyle, F. 1946, MNRAS, 106, 343
- Innes, D. E., Giddings, J. R., & Falle, S. A. E. G. 1987, MNRAS, 224, 179
- Itoh, H. 1981, PASJ, 33, 1
- Iyudin, A. F., et al. 1994, A&A, 284, L1
- Jones, T. J., Rudnick, L., DeLaney, T., & Bowden, J. 2003, ApJ, 587, 227
- Kaastra, J. S., & Mewe, R. 1993, A&AS, 97, 443
- Kallman, T. R., & McCray, R. 1982, ApJS, 50, 263
- Kamper, K. W. 1980, Observatory, 100, 3
- Keenan, F. P., Aller, L. H., Bell, K. L., Hyung, S., McKenna, F. C., & Ramsbottom, C. A. 1996, MNRAS, 281, 1073
- Keenan, F. P., Hibbert, A., Ojha, P. C., Conlon, E. S. 1993, Phys. Scr, 48, 129
- Keohane, J. W., Rudnick, L., & Anderson, M. C. 1996, ApJ, 466, 309

- Kirshner, R. P., & Chevalier, R. A. 1977, *ApJ*, 218, 142
- Glazebrook, K., & Economou, F. 1997, *Dr. Dobb's Journal*, 9719, 45
- Krause, O., Birkmann, S. M., Usuda, T., Hattori, T., Goto, M., Rieke, G. H., & Misselt, K. A. 2008, *Science*, 320, 1195
- Lamers, H. J. G. L. M., de Groot, M., & Cassatella, A. 1983, *A&A*, 128, 299
- Laming, J. M. 2001, *ApJ*, 546, 1149
- Laming, J. M., & Hwang, U. 2003, *ApJ*, 597, 347
- Landi, E., Del Zanna, G., Young, P. R., Dere, K. P., Mason, H. E., & Landini, M. 2006, *ApJS*, 162, 261
- Levermore, C. D., & Pomraning, G. C. 1981, *ApJ*, 248, 321
- Li, H., McCray, R., & Sunyaev, R. A. 1993, *ApJ*, 419, 824
- Liska, R. & Wendroff, B. 2003, *SIAM J. Sci. Comp.*, 25, 3, 995
- Mazzotta, P., Mazzitelli, G., Colafrancesco, S., & Vittorio, N. 1998, *A&AS*, 133, 403
- McCarthy, D. W., Jr., Ge, J., Hinz, J. L., Finn, R. A., & de Jong, R. S. 2001, *PASP*, 113, 353
- Meléndez, M., Bautista, M. A., & Badnell, N. R. 2007, *A&A*, 469, 1203
- Mendoza, C., & Zeippen, C. J. 1982, *MNRAS*, 199, 1025
- Merrill, S. P. W. 1952, *ApJ*, 116, 21
- Mitnik, D. M., & Badnell, N. R. 2004, *A&A*, 425, 1153
- Morgan, J. A. 2008, *The Observatory*, 128, 80

- Morse, J. A., Fesen, R. A., Chevalier, R. A., Borkowski, K. J., Gerardy, C. L., Lawrence, S. S., & van den Bergh, S. 2004, *ApJ*, 614, 727
- Nagataki, S., Hashimoto, M.-A., Sato, K., Yamada, S., & Mochizuki, Y. S. 1998, *ApJL*, 492, L45
- Nahar S. N., Delahaye F., Pradhan A. K., C.J. Zeippen C. J. 2000, *A&AS*, 144, 141
- Nahar, S. N. 2006, *A&A*, 448, 779
- Nisini, B., Bacciotti, F., Giannini, T., Massi, F., Eisloffel, J., Podio, L., & Ray, T. P. 2005, *A&A*, 441, 159
- Nussbaumer, H., & Storey, P. J. 1988, *A&A*, 193, 327
- Nagataki, S., Hashimoto, M.-A., Sato, K., Yamada, S., & Mochizuki, Y. S. 1998, *ApJL*, 492, L45
- Osterbrock, D. E. 2001, *Bulletin of the American Astronomical Society*, 33, 1330
- Pastorello, A., et al. 2008, *MNRAS*, 389, 955
- Patnaude, D. J., & Fesen, R. A. 2005, *ApJ*, 633, 240
- Patnaude, D. J., & Fesen, R. A. 2008, arXiv:0808.0692
- Payne, C. H. 1925, *Stellar atmospheres; a contribution to the observational study of high temperature in the reversing layers of stars*, (Cambridge, MA: The Observatory)
- W. H. Press, S. A. Teukolsky, W. T. Vetterling, B. P. Flannery 1992, *Numerical Recipes in C: The Art of Scientific Computing*, Second Edition, (New York: Cambridge University Press)

- Qiu, Y., Li, W., Qiao, Q., & Hu, J. 1999, *AJ*, 117, 736
- Quinet, P., Le Dourneuf, M., & Zeippen, C. J. 1996, *A&AS*, 120, 361
- Raymond, J. C. 1979, *ApJS*, 39, 1
- Raymond, J. C., Hester, J. J., Cox, D., Blair, W. P., Fesen, R. A., & Gull, T. R. 1988, *ApJ*, 324, 869
- Raymond, J. C., & Smith, B. W. 1977, *ApJS*, 35, 419
- Reed, J. E., Hester, J. J., Fabian, A. C., & Winkler, P. F. 1995, *ApJ*, 440, 706
- Reynolds, S. P. 1998, *ApJ*, 493, 375
- Reynoso, E. M., & Goss, W. M. 2002, *ApJ*, 575, 871
- Rho, J., Reynolds, S. P., Reach, W. T., Jarrett, T. H., Allen, G. E., & Wilson, J. C. 2003, *ApJ*, 592, 299
- Richmond, M. W., Treffers, R. R., Filippenko, A. V., Paik, Y., Leibundgut, B., Schulman, E., & Cox, C. V. 1994, *AJ*, 107, 1022
- Richtmyer, R. D., Morton, K. W. 1967, *Difference Methods for Initial-Value Problems*, Krieger: Malabar
- Rousselot, P., Lidman, C., Cuby, J.-G., Moreels, G., & Monnet, G. 2000, *A&A*, 354, 1134
- Rybicki, G. B., Lightman, A. P. 1979, *Radiative Processes in Astrophysics*, John Wiley and Sons: New York
- Rybicki, G. B., & Hummer, D. G. 1991, *A&A*, 245, 171
- Searle, L. 1971, *ApJ*, 168, 41

- Seaton, M. J., 1987, *J. Phys. B* 20, 6363
- Shull, J. M., & van Steenberg, M. 1982, *ApJS*, 48, 95
- Shull, J. M., & van Steenberg, M. E. 1985, *ApJ*, 298, 268
- Sigut, T. A. A., & Pradhan, A. K. 2003, *ApJS*, 145, 15
- Skrutskie, M. F., et al. 2006, *AJ*, 131, 1163
- Smith, R. K., Brickhouse, N. S., Liedahl, D. A., & Raymond, J. C. 2001, *ApJL*, 556, L91
- Smith, N., & Hartigan, P. 2006, *ApJ*, 638, 1045
- Smith, J. D. T., Rudnick, L., Delaney, T., Rho, J., Gomez, H., Kozasa, T., Reach, W., & Isensee, K. (S09) 2009, *ApJ*, 693, 713
- Spitzer, L. 1978, *Physical Processes in the Interstellar Medium* (New York: John Wiley & Sons)
- Stevens, W. R. & Rago, S. A. 2005, *Advanced Programming in the Unix Environment, Second Edition*, (Upper Saddle River, NJ: Addison-Wesley)
- Stone, J. M., & Norman, M. L. 1992, *ApJL*, 390, L17 (1992a)
- Stone, J. M., & Norman, M. L. 1992, *ApJS*, 80, 753 (1992b, SN92)
- Tananbaum, H. 1999, *IAU Circ.*, 7246, 1
- Tayal, S. S., & Gupta, G. P. 1999, *ApJ*, 526, 544
- Thorstensen, J. R., Fesen, R. A., & van den Bergh, S. 2001, *AJ*, 122, 297

- Timmes, F. X., Woosley, S. E., Hartmann, D. H., & Hoffman, R. D. 1996, *ApJ*, 464, 332
- Troland, T. H., Crutcher, R. M., & Heiles, C. 1985, *ApJ*, 298, 808
- Truelove, J. K., & McKee, C. F. 1999, *ApJS*, 120, 299
- Vancura, O., Blair, W. P., Long, K. S., & Raymond, J. C. 1992, *ApJ*, 394, 158
- van den Bergh, S. 1971, *ApJ*, 165, 259
- van Leer, B. 1977, *J. Comp. Phys.*, 23, 276
- Vink, J., Laming, J. M., Kaastra, J. S., Bleeker, J. A. M., Bloemen, H., & Oberlack, U. 2001, *ApJL*, 560, L79
- von Neumann, J. & Richtmyer, R. D. 1950 *J. Appl. Physics* 21, 232
- Willingale, R., Bleeker, J. A. M., van der Heyden, K. J., & Kaastra, J. S. 2003, *A&A*, 398, 1021
- Wright, M., Dickel, J., Koralesky, B., & Rudnick, L. 1999, *ApJ*, 518, 284
- Young, P. A., et al. 2006, *ApJ*, 640, 891
- Zatsarinny, O., Gorczyca, T. W., Korista, K. T., Badnell, N. R., & Savin, D. W. 2003, *A&A*, 412, 587
- Zatsarinny, O., Gorczyca, T. W., Korista, K. T., Badnell, N. R., & Savin, D. W. 2004, *A&A*, 417, 1173
- Zatsarinny, O., Gorczyca, T. W., Korista, K., Badnell, N. R., & Savin, D. W. 2004, *A&A*, 426, 699

Zatsarinny, O., Gorczyca, T. W., Fu, J., Korista, K. T., Badnell, N. R., & Savin, D. W.  
2006, *A&A*, 447, 379